EXTERNAL COUPLING IN ORGANIC LIGHT-EMITTING DEVICES

Min-Hao Michael Lu

A DISSERTATION

PRESENTED TO THE FACULTY

OF PRINCETON UNIVERSITY

IN CANDIDACY FOR THE DEGREE

OF DOCTOR OF PHILOSOPHY

RECOMMENDED FOR ACCEPTANCE

BY THE DEPARTMENT OF

ELECTRICAL ENGINEERING

January 2002

Abstract

This work revolves around organic light-emitting devices (OLEDs) and its application in information displays. The bulk of the work is devoted to the investigation of light emission and external coupling in OLEDs after the appropriate excitons have been formed. The internally-emitted light can be classified into three modes: externally-emitted, substrate-waveguided, and ITO/organic-waveguided. A combined classical and quantum mechanical microcavity (CCQMM) model was used to calculate the lifetime of the excitons and the distribution of light emission into various modes as a function of the OLED architecture. Bilayer OLEDs with varying emitting layer thicknesse, indium-tin-oxide anode thickness, and index of refraction of the substrate were fabricated on both planar and shaped substrates. Shaped substrates were found to increase the external coupling efficiency by converting some substrate-waveguided modes into external modes. The largest increase were in OLEDs on shaped hight index-of-refraction substrates where an increase by a factor of 2.3 in the integrated external emission was measured. The CCQMM model accurately predicts the far-field intensity profile, the edge emission and the increase in external emission due to shaped substrates. Device optimization based on these results is discussed.

The second part of this thesis presents the work on an amorphous silicon thin film transistor (TFT) based active-matrix OLED display pixel. The two-TFT pixels were operated at VGA video rates and pixel luminance adjustment by the

data voltage was demonstrated.

The work on patterning OLEDs by lithographically patterning and dry etching the cathodes is present in the last part of this thesis. OLEDs with aluminum cathodes were shown to be compatible with the lithographic process. OLED degradation due to exposure to chlorine or oxygen plasma was quantified by measuring the growth of edge dark rings.

Acknowledgement

The production of a thesis is an emotionally charged affair. Not only is one full of hope and energy facing the myriad new possibilities in life, but also one cannot help but being sentimental about leaving a place accustomed to for over five years — the frequency and acridity of past statements to the contrary notwithstanding. It is my prerogative to take this moment to reflect upon a few things.

First and foremost, I dedicate this thesis to my parents: to my father, who was the first to show me the joy of research, and to my mother, whose boundless love is like no other that I know. Without them, this work would not have been possible.

Next, I would like to thank my advisor, Prof. Jim Sturm, who through the years has always believed in and respected me, who has shown, by example, the meaning of "hard work". I will always remember his scientific insight and carry with me his contagious enthusiasm.

Last but not least, there are a number of people who I own a debt of gratitude to. More than any one thing or event, they define my Princeton experience. They are, Chung-Chih Wu, Steve Theiss, Eugene Ma, Mike Valenti, Joe Palmer, Duane Marcy, Helena Gleskova, Florian Pschenitzka, Tom Hebner, Conor Madigan, Ke Long, Kiran Pangal, Malcolm Carroll, Eric Stewart, Iris Hsu, Richard Huang, Haizhou Yin, Xiangzhen Bo, John Thomson, Tom Dong, Pambos Anastasiou, Rob Runser, Manuel Sales, Bing Wang, Christine Coldwell, Gautam

Parthasarathy, Bob Min, Lori Stirling, Amlan Majumdar, Ravi Pillarisetty, Rabin Bhattacharya, and Paru Deshpande. Through times good and bad, they have stood by me (often because they are the very instigators of the said good or bad times). I will forever cherish the memories that these names invoke.

Min-Hao Michael Lu

Princeton, NJ, September 2001

Contents

List of Figures

List of Tables

Chapter 1

Introduction

1.1 Motivation

We are living in an information age. As they say, "a picture is worth a thousand words" — the most efficient way for human beings to receive information is through the visual means. The holy grail of the display industry is a full-color, high information-content, and low-cost display that is bright, high-contrast, lightweight, and unbreakable. A new technology based on organic light-emitting devices (OLEDs) seems the most promising for meeting these requirements.

The current wave of intense research interest in OLEDs started with the work of Tang et al. at Kodak on small molecule OLEDs, and that of Borroughes et al. on polymer OLEDs [1, 2]. A simple schematic representation of a typical OLED is shown in Figure 1.1. It is a two-terminal device that emits light under an applied voltage. The anode is usually made of indium-tin-oxide (ITO), a metal

oxide that has high transparency ($\sim 90\%$ for a 100 nm film), low resistivity ($\rho \simeq 5 \times 10^{-4}$ Ω-cm) and high work function ($\phi \simeq 4.8$ eV). The cathode is usually made of a low work function metal, such as a magnesium/silver (Mg:Ag) alloy. The organic material sandwiched in between can be comprised of one or several layers of small-molecule compounds or polymers. The total thickness of the device (anode/organic material/cathode) is around 300-400 nm, and it can be deposited on most substrates, including flexible plastic or stainless steel substrates [3, 4], making it an attractive technology for flat panel displays.

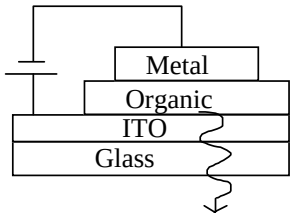

Figure 1.1: Schematic representation of a typical OLED with an ITO anode and a metal cathode. The organic region is comprised of one or several layers of small-molecule compounds or polymers. Light is emitted from the bottom under an applied voltage.

Today, the color gamut of OLEDs rivals that of CRT's; power efficiencies up to 18 lm/W and half life of 7,500 h at an initial luminance of 1462 cd/m^2 have been reported [5]-[8]. With rapidly improving device performance and decreasing cost, new applications, such as general lighting, are being explored. Current products that feature OLED displays include a car audio system from Pioneer and the Timeport^{TM} P8767 cellular phones from Motorola. They are both passive-matrix, multi-color displays (different regions of the display have different colors

by large-feature shadow-masked deposition; no color sub-pixels). Many technological problems, in particular, device life time, patterning, and active-matrix pixel design, have to be solved before a reliable full-color, large area, and high-resolution OLED display can be brought to market.

This work addresses several OLED-display-related issues. The majority of the thesis is devoted to the investigation of the external coupling of light from the OLED through both theoretical modeling and experiments. One of the key figures of merit of OLEDs is its external quantum efficiency (photons out/electrons in); however, in a typical device, a large amount of the internally generated light is trapped due to refractive index mismatching and never escapes to the viewer. A rigorous combined classical and quantum mechanical microcavity (CCQMM) model is used to compute the exact amount of light that escapes to the viewer and that trapped inside. An experimental approach utilizing back-side substrate patterning harvests light trapped in the substrate and converts it into useful, externally-emitted light. The enhancement in the external coupling efficiency is calculated by the model and correlated with empirical data for various device architectures. An increase by a factor of 2.3 in the total integrated external emission was observed in an OLED on shaped high-index-of-refraction substrates.

A secondary portion of this thesis deals with the design and fabrication of an amorphous silicon (α-Si) thin film transistor (TFT) based active-matrix OLED (AMOLED) display pixel. A two-transistor pixel driving a single-layer polymer

OLED capable of video brightness was fabricated and driven with a typical video rate signal for a VGA (480 rows) display. Lastly, the work on patterning OLED cathodes with conventional photolithography and dry etching is presented.

1.2 Thesis Outline

This thesis is organized as follows: after an introduction in Chapter 1, and a brief overview of the physics and chemistry of OLEDs in Chapter 2, the development of bilayer OLEDs, lithium fluoride/aluminum (LiF/Al) cathodes, and rf magnetron sputtered ITO is presented in Chapter 3. In Chapter 4, the CCQMM model is derived in detail. In addition, some preliminary numerical results are presented. Chapter 5 contains the data and discussion on the external and edge emission of devices on both planar and shaped substrates. Based on the modeling and experimental results, device optimization schemes are discussed. The work on the α-Si TFT based AMOLED pixel is discussed in Chapter 6. Chapter 7 deals with lithographically patterned cathodes for OLEDs and their process tolerances. The conclusions and suggestions for future work are located in Chapter 8. Sample Mathematica code of the CCQMM model is in the Appendix.

References

[1] C. W. Tang and S. A. VanSlyke, *Appl. Phys. Lett.* **51**, 913 (1987).

[2] J. H. Burroughes, D. D. C. Bradley, A. R. Brown, R. N. Marks, K, Mackay, R. H. Friend, P. L. Burns, and A. B. Holmes, *Nature* **347**, 539 (1990).

[3] P. E. Burrows, G. Gu, V. Bulović, Z. Shen, S. R. Forrest, and M. E. Thompson, *IEEE Trans. Elec. Dev.* **44**, 1188 (1997).

[4] C. C. Wu, S. D. Theiss, G. Gu, M. H. Lu, J. C. Sturm, S. Wagner and S. R. Forest, *IEEE Elec. Dev. Lett.* **18**, 609 (1997).

[5] K. Heeks, C. Towns, J. Burroughes, S. Cina, and A. Gunner, *IEDM Tech. Dig.*, 615 (2000).

[6] M. T. Bernius, M. Inbasekaran, J. O'Brien, and W. Wu, *Adv. Matt.* **12**, 1737 (2000).

[7] V.-E. Choong, S. Shi, J. Curless, C.-L. Shieh, H.-C. Lee, F. So, J. Shen, and J. Yang, *Appl. Phys. Lett.* **75**, 172 (1999).

[8] J. Shi and C. W. Tang, *Appl. Phys. Lett.* **70**, 1665 (1997).

Chapter 2

The Physics and Chemistry of Organic Light-Emitting Devices

2.1 Introduction

Organic light-emitting devices (OLEDs) are based on the electroluminescence (EL) of organic materials. EL refers to the emission of light from a material under an electric bias. A closely related phenomenon is photoluminescence (PL) where the light emission is from photo-excited materials. EL and PL of organic materials originate from the radiative decay of excited molecules, also called excitons. This chapter provides a brief review of the formation and decay of excitons in organic compounds.

2.2 Electronic structure of organic compounds

In organic solids, the intermolecular bonds are due to the weak van der Waals forces, so the overlap of molecular orbitals is small — the molecular energy levels are less perturbed than in inorganic solids and many features of single molecules are preserved in solids. Most organic compounds relevant to OLEDs contain many conjugated hydrocarbon structures where there is a regular alternation of single and double chemical bonds [1]. A classic example is the benzene molecule where alternating single and double bonds connect six carbon atoms in a cyclical fashion (Figure 2.1a). The bonding is in sp^2 hybridization where each carbon forms localized σ bonds with two neighboring carbon atoms and one hydrogen atom. These σ bonds have 120° bond angles and lie in the molecular plane. The overlap of the perpendicular, lone $2p_z$ orbital give rise to the extended π electron orbitals above and below the molecular plane [2] (Figure 2.1b). The delocalization of the π electrons also serve to stabilize the benzene molecule. In general, the atomic interactions in organic molecules result in bonding (π) and anti-bonding (π^*) electronic orbitals. Among these molecular orbitals, two are the most significant: the highest occupied molecular orbital (HOMO) which is similar to the valence band of the inorganic semiconductor, and the lowest unoccupied molecular orbital (LUMO) which is similar to the conduction band. The difference between the HOMO and the LUMO is the energy bandgap, E_g.

In principle, all the macroscopic properties of a system can be deduced if

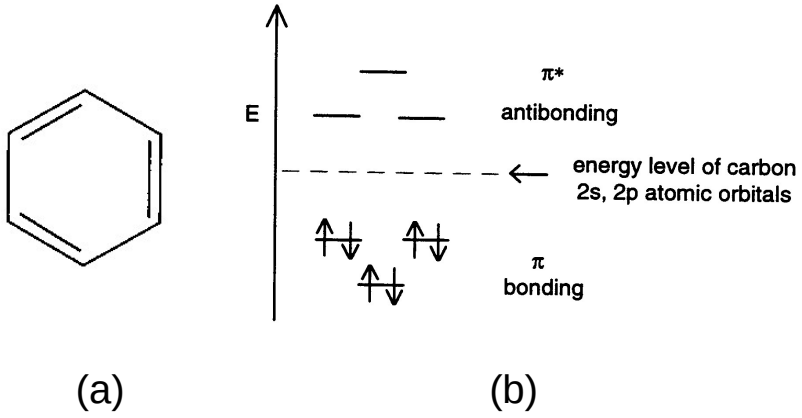

Figure 2.1: (a) The benzene molecule, (b) the bonding (π) and anti-bonding ($\pi*$) orbitals of benzene.

the wave function Ψ of the system is known. The wave function can be obtained by solving the Schrödinger equation,

$$H\Psi = E\Psi \tag{2.1}$$

where H denotes the Hamiltonian operator which consists of not only the electronic energy operator, but also the operators that represent the nuclear kinetic and nuclear-electronic interaction energies. Most formulations of molecular electronic states deal with vibrational and electronic (vibronic) motion. Due to the disparity between the nuclear and electronic masses, the electrons can be considered to react instantaneously to changes in nuclear configuration. In fact, electronic transitions take place in only $\leq 10^{-15}$ s, as compared with about 10^{-13} s for nuclear motions [2]. This is the basis for the Born-Oppenheimer approximation where the electronic wave functions are calculated from the instantaneous nuclear positions. Each electronic state is associated with a nuclear potential energy surface and form

a vibronic manifold as shown in Figure 2.2. Electronic transitions are completed before the nuclei can alter their spatial relationship. Such a transition is called a vertical, or Franck-Condon, transition (Figure 2.2).

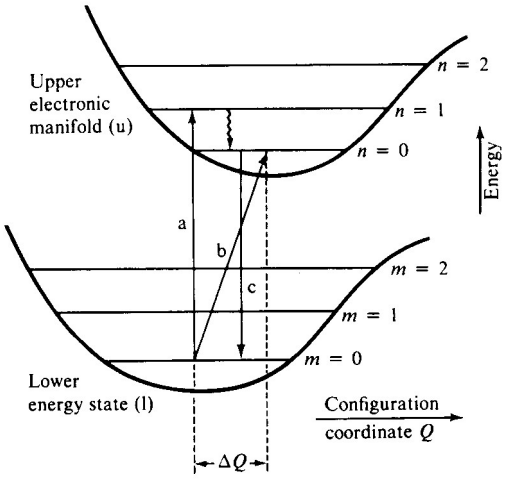

Figure 2.2: Two electronic states, u = upper state, l = lower state, and a few of their associated vibrational states. Transition a denotes a vertical Franck-Condon transition, whereas transition b represents a zero-phonon transition. The transition denoted by the wavy line is a radiationless transition between vibrational states of the upper electronic state. The letter c labels the emission or fluorescence transition and ΔQ represents the configurational coordinate displacement of the upper state relative to the ground electronic state. (From Ref. [2])

2.3 Spectral properties

In the molecular ground state, the HOMO is entirely filled and the LUMO is entirely empty. In molecules with a single excited electron, the excited states can be categorized into singlet states where the excited electron and the hole have antiparallel spin, or triplet states where their spins are parallel. The singlet states

excited states are labelled S^1, S^2, etc., and the triplet excited states T^1, T^2, etc. The ground state is singlet and usually labelled S^0. In general, the triplet states have lower energies than the corresponding singlet states. Dipole selection rules allow the transition $S^n \rightarrow S^0 + h\nu$ (fluorescence) whose characteristic lifetime is on the order of 10^{-9} s. On the other hand, the transition $T^n \rightarrow S^0 + h\nu$ (phosphorescence) is forbidden. In many organic compounds, phosphorescence is usually an extremely slow process: phosphorescence lifetime can be on the order of milliseconds, the exception being those compounds incorporating atoms such as platinum (Pt) or iridium (Ir), where the strong spin interaction of the "heavy atom" mixes the singlet and triplet states, thus allowing fast phosphorescence responses [3]. Phosphorescent dye dopants incorporating Pt or Ir have been used to fabricate extremely efficient OLEDs [5]-[11].

Since the nuclear motion happen on the order of 10^{-13} s, much faster than the fluorescence and phosphorescence lifetimes, excited molecules have sufficient time to decay to the lowest state in the vibronic manifold before radiative recombination. As a result, there is a well-known shift between the absorption and emission spectra which is named after Frank and Condon (Franck-Condon shift) (Figure 2.3).

There are other transition pathways in competition with fluorescence and

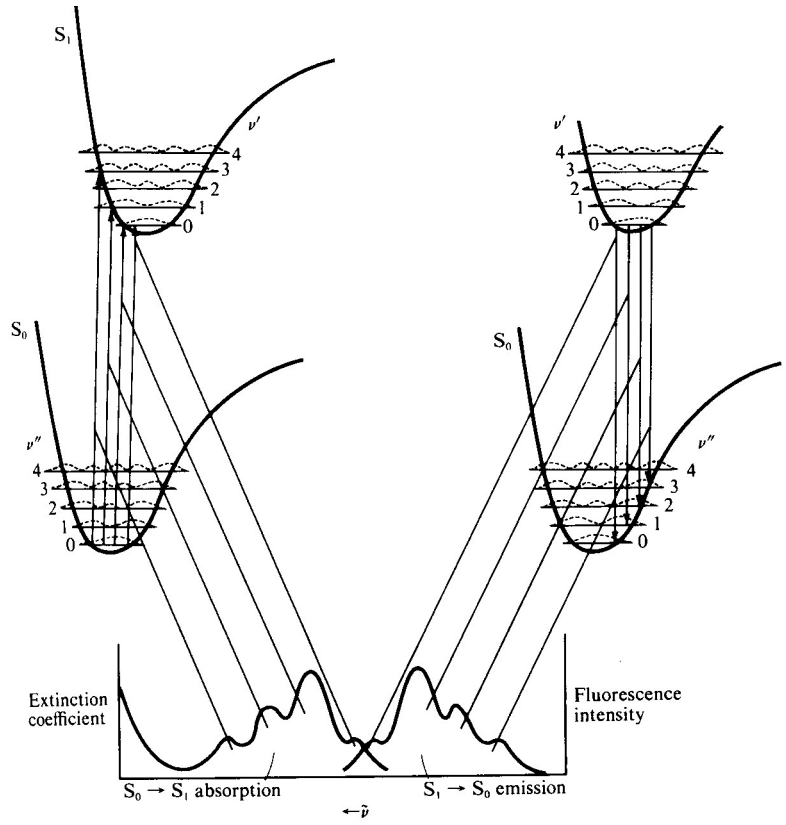

Figure 2.3: Simplified potential energy curves with vibrational probability functions showing how a mirror-image relations can arise between the electronic absorption and emission bands. (From Ref. [13, p. 108])

phosphorescence (Figure 2.4), namely,

$$\begin{aligned} S_1 &\rightarrow S_0 + \text{heat} \quad \text{Internal Conversion} \\ S_1 &\rightarrow T_1 + \text{heat} \quad \text{Intersystem Crossing} \\ T_1 &\rightarrow S_0 + \text{heat} \quad \text{Intersystem Crossing} \end{aligned} \tag{2.2}$$

where "heat" refers to the excitation of the phonon modes. In general, internal conversion is a non-radiative transition between two states of like spin multiplicity; intersystem crossing describes the non-radiative transition involving states of

different spin multiplicity [12].

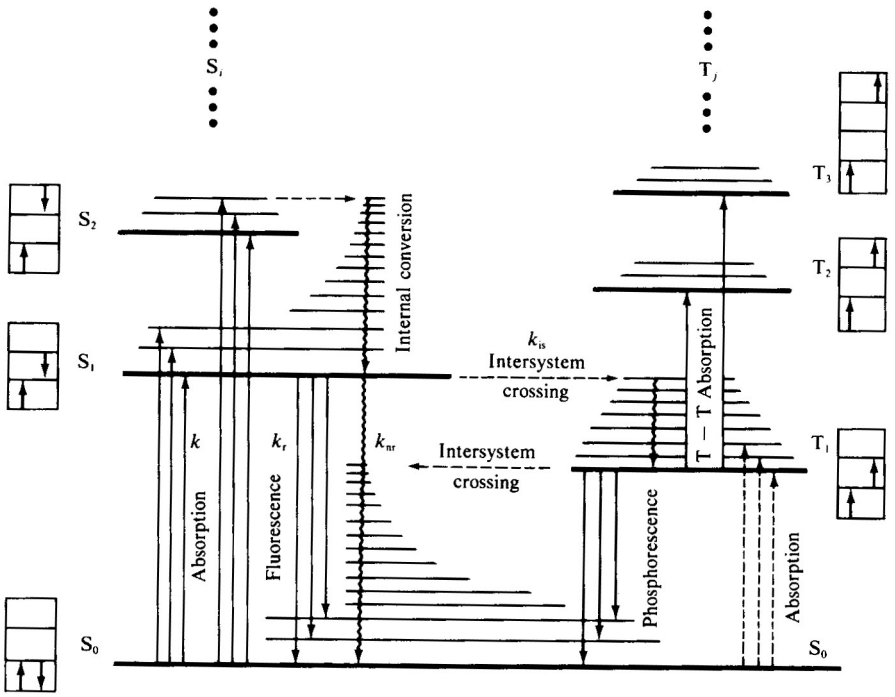

Figure 2.4: Radiative and non-radiative decay processes in a typical polyatomic molecule that obeys Kasha's rule: the radiative transition in a given spin manifold always occurs from the lowest excited state. Not all molecules obey Kasha's rule. The dispositions of the electron spins are shown in the boxes alongside the singlet (S) and triplet (T) state designations. The variables $k_{nr}, k_r,$ and k_{is} are, respectively, the nonradiateve decay rate to the ground state, the radiative decay rate to the ground state, and the intersystem crossing rate to the triplet manifold. (From Ref. [14, p. 2])

2.4 Small-molecule bilayer OLEDs

By far the most studied small molecule OLED system is based on the electron transport layer (ETL)/hole transport layer (HTL) heterostructure (Figure 2.5). Tris(8-hydroxyquinoline) aluminum (Alq_3) is the most common ETL, which often

serves as the emitting layer (EML) as well [15, 16]. ITO and Mg:Ag (10:1) are commonly used as the anode and cathode, respectively. Electrons and holes are injected from the respective electrode and a portion of them recombine to form excitons. At high injection levels, carrier transport is dominated by trapped-charge-limited current [17].

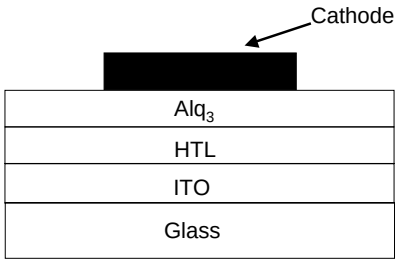

Figure 2.5: Schematic diagram of a small molecule bilayer OLED based on Alq_3 and an HTL.

The optical properties of low-mobility organic solids are dominated by small-radius Frenkel excitons, which are essentially excited single molecules as discussed in the previous section [18]. Figure 2.6 shows schematically the emission mechanism in bilayer OLEDs based on tris(8-hydroxyquinoline) aluminum (Alq_3)/N,N'-diphenyl-N,N'-(3-methylphenyl)-1,1'-biphenyl-4,4'diamine (TPD). Electrons trapped in Alq_3 near the Alq_3/TPD interface combine with a minority hole to form Frenkel excitons through Coulombic relaxation in the Alq_3 band gap, which subsequently recombine to generate electroluminescence [17].

The spins of the electron and the hole are uncorrelated, which, according to simple spin statistics, implies that of the excitons formed, 25% are singlets and 75% are triplets. In photoluminescence, however, the excited states are all

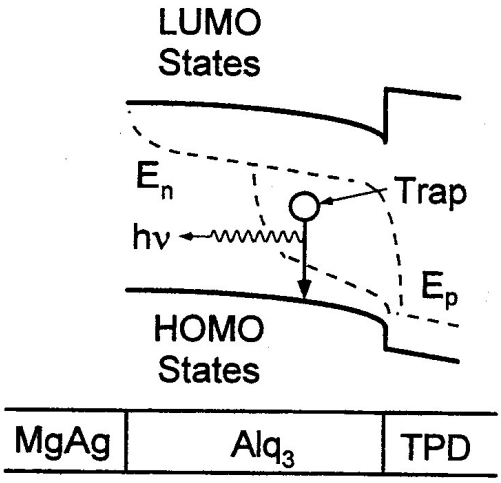

Figure 2.6: Schematic diagram showing the relaxation for trapped (polaronic self-trapping) electrons in Alq_3 with a minority hole, to form a distribution of Frenkel excitons in the Alq_3 band gap, which subsequently recombine to generate electroluminescence. (From Ref. [17])

singlets, viz. $S^0 + h\nu \rightarrow S^n$. Thus it is believed that the upper limit of the EL quantum efficiency (photo emitted/electron) is 25% that of the PL quantum efficiency (photon emitted/photon absorbed) [19]. The fraction of singlet excitons in an Alq_3-based OLED has been experimentally measured to be $22 \pm 2\%$ [8].

On the other hand, in polymer OLEDs based on derivatives of poly(phenylene vinylene) (PPV), it has been suggested recently that the triplet/singlet ratio is less than 3:1 — singlets are created preferentially despite having higher energy. One theoretical justification is that the polar nature of the singlet wavefunction more closely resembles the wavefunction of the unbound electron and hole, thus the singlet formation cross-section is greater than that of the triplet [20]-[22]. This intriguing and fundamental question remains an area of ongoing investigation.

2.4.1 Color tuning and energy transfer mechanisms

In conjugated-polymer-based OLEDs, changing the emission color is accomplished through structural modification of the polymer [23, 24], but in small molecule OLEDs, it is achieved through an entirely different mechanism. Tang and coworkers demonstrated color tuning in OLEDs by using a dye-sensitized host material as the EML [16]. The excitons created on the host molecule are transferred to the dye guest, where they recombine and emit light. The color of the emission is determined by the energy levels of the dye molecule rather than those of the host. Two of the most important energy transfer mechanisms are Förster transfer and Dexter transfer. An independent process of carrier trapping will be reviewed in the next section.

Förster energy transfer involves a dipole-dipole coupling of the transition dipole moments of the excited donor (host exciton) and the dye (acceptor) in its ground state (Figure 2.7). The advantage of this sort of energy transfer process is that the dipole-dipole interaction can be quite strong over large distances, allowing efficient energy transfer over distances of up to 10 nm in very favorable cases. An analytical expression of the rate of Förster energy transfer, $K_{ET}^{Föster}$, is given by [25]

$$K_{ET}^{Föster} = 0.382 \times 10^{-20} \frac{9k^2}{128\pi^5 n^4 r^6 \tau_D} \int_0^\infty F_D(\tilde{\nu}) \epsilon_A(\tilde{\nu}) \frac{d\tilde{\nu}}{\tilde{\nu}^4} \tag{2.3}$$

$$R_0^6 = 0.382 \times 10^{-20} \frac{9k^2}{128\pi^5 n^4} \int_0^\infty F_D(\tilde{\nu}) \epsilon_A(\tilde{\nu}) \frac{d\tilde{\nu}}{\tilde{\nu}^4} \tag{2.4}$$

$$\Phi_{PL} = \int_0^\infty F_D(\tilde{\nu}) d\tilde{\nu} \tag{2.5}$$

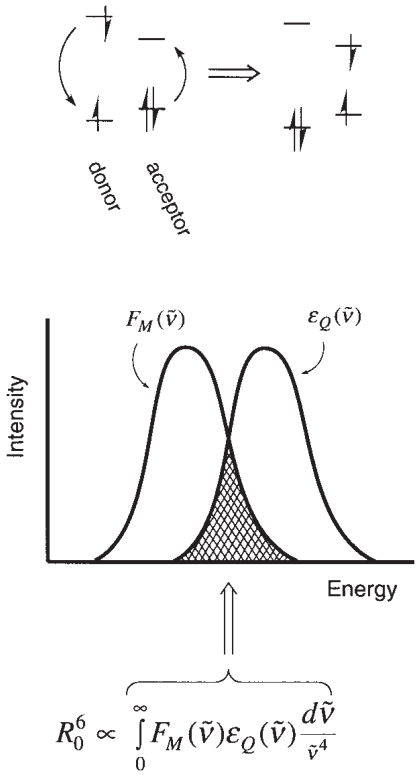

Figure 2.7: Schematic representation of Förster energy transfer and overlap integral from eq. 2.4 shown as the shaded region of the curves. (From Ref. [26])

where $0.382 \times 10^{-20} = 1000/N_A \ln 10$ is the conversion factor between the molar extinction coefficient [liter mol/cm] and the absorption cross-section [cm^2]; N_A is the Avagardro's number. k^2 is an orientation factor, which has a value of 2/3 for random donor-acceptor orientations as found in doped OLEDs. n is the refractive index of the medium. r is the donor-acceptor separation, and τ_D is the fluorescence lifetime of the donor. $F_D(\tilde{\nu})$ is the fluorescent spectrum of the donor, defined as in eq. 2.5, where Φ_{PL} is the fluorescence quantum yield; $\epsilon_A(\tilde{\nu})$ is the molar extinction coefficient spectrum of the acceptor; and $\tilde{\nu}$ is the energy in wave numbers ($E = hc\tilde{\nu}, \tilde{\nu} = 1/\lambda$). A high rate of energy transfer from the host to the dye molecule relative to the radiative relaxation rate of the host will lead to emission predominantly from the dye dopant. A more common approach to evaluating Förster energy transfer is to calculate the Förster radius R_0 given in eq. 2.5. The Förster radius is defined as the distance between the donor and acceptor at which the probability of intermolecular energy transfer equals that of relaxation of the donor by fluorescence or unimolecular processes. A large Förster radius is indicative of a very efficient energy transfer process, which will compete with unimolecular relaxation very effectively at distances shorter than R_0. Assuming the dyes are uniformly dispersed in the host, e.g. in Alq_3, a dye doping level of 1% would correspond to a sphere of 100 Alq_3 surrounding each dye molecule, with a radius of roughly 3 Alq_3 molecules ($4\pi r^3 = 100$). The diameter of Alq_3 is roughly 0.9 nm, leading to an estimate of 2.7 nm for the maximum distance that an Alq_3

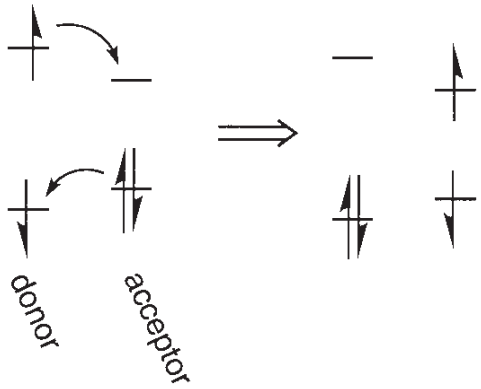

Figure 2.8: Dexter electron-exchange energy transfer process. (From Ref. [26])

exciton can be from a dopant molecule. As a comparison, the Förster radius for DCM in Alq_3 has been calculated to be 3.3 nm, implying efficient Förster energy transfer in this system [2, 26, 27].

An alternative process for energy transfer may also be active in dye-doped materials, which achieves energy transfer via an electron exchange mechanism. This process is often referred to as Dexter energy transfer and is shown schematically in Figure 2.8 [28].

Either simultaneous or consecutive electron transfers lead to the donor in its ground state and the acceptor in its electronic excited state. This transfer mechanism can be visualized as occurring by formation of a transient exciplex (a complex formed by an excited molecule and a ground-state molecule of different species [26, 27]), which relaxes to a ground state on the donor and an excited state on the acceptor. The rate of the Dexter energy transfer (K_{ET}^{Dexter}) is proportional to the degree of overlap between the donor emission spectrum (E_D) and the acceptor

absorption spectrum (A_A) (eq. 2.6). Contrary to the case found in Förster energy transfer, however, the emission and absorption spectra are normalized (such that the area under each spectra is 1), removing any dependence of the rate on the absolute magnitude of the donor PL efficiency or the acceptor extinction coefficient. The integral of eq. 2.6 is normalized such that complete overlap of the emission and absorption spectra corresponds to a value of 1. The parameter Z cannot be obtained directly from optical experiments, but is related to the electronic matrix element for electron-exchange energy transfer. The magnitude of Z is dependent on the the donor-acceptor distance, as shown in eq. 2.6, where r is the donor-acceptor distance and L is the sum of the van der Waals radii of the donor and acceptor molecules [2, 26, 28].

$$K_{ET}^{Dexter} = \frac{2\pi}{\hbar} Z^2 \int_0^\infty E_D(\tilde{\nu}) A_A(\tilde{\nu}) d(\tilde{\nu}), \quad Z^2 \propto e^{-2r/L} \tag{2.6}$$

Dexter energy transfer is fastest for very short donor-acceptor separations and decreases rapidly as the separation increases. The rate of energy transfer by a Dexter type mechanisms is expected to drop to negligible levels beyond a 1.5–2.0 nm donor-acceptor distance in Alq_3. Förster energy transfer requires that both the donor and the acceptor states to have the same spin multiplicity. Dexter energy transfer, however, does not have such a requirement, and transfer from donor singlet states to acceptor triplets states are possible, as demonstrated in OLEDs based on Alq_3:PtOEP. Because of the short donor-acceptor distance requirement,

high doping levels (5–10%) are used in these systems [5, 6].

2.5 Single-layer doped-polymer OLEDs

Efficient dye-doped single-layer polymer OLEDs based on (poly(N-vinylcarbazole) (PVK) and 2-(4-biphenyl)-5-(4-tert-butylphenyl)-1,3,4-oxadiazole (PBD)/Coumarin 6 (C6) have been demonstrated (Figure 2.9) [4], [29]-[31]. The hole transport

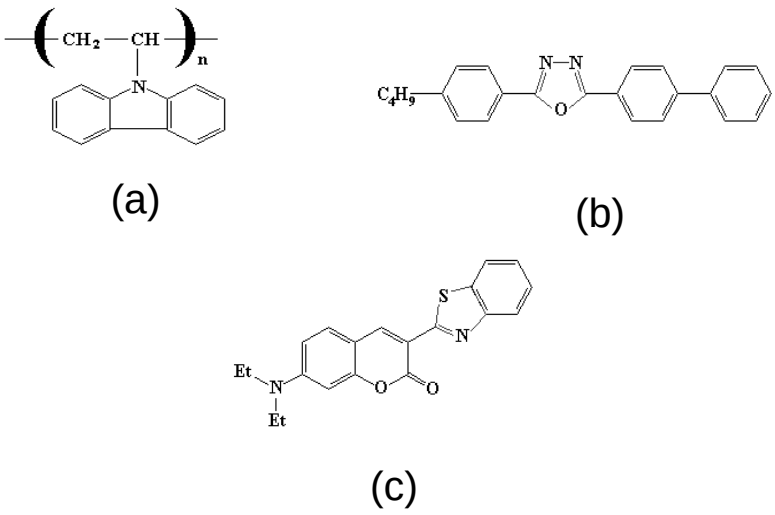

Figure 2.9: Chemical structures of (a) PVK, (b) PBD, and (c) C6.

function is provided by PVK, a non-conjugated polymer whose carbazole groups are electrically active [32]. It has been studied extensively as a photoconductor since the 1950's [2, 32]. The electron transport function is provided by the small molecule PBD. The emission color is tuned by choice of the dye dopant, in this case, C6. All three components are dissolved in the same solution and cast as a single film (Figure 2.10). The band diagram of the single layer PVK/PBD/C6

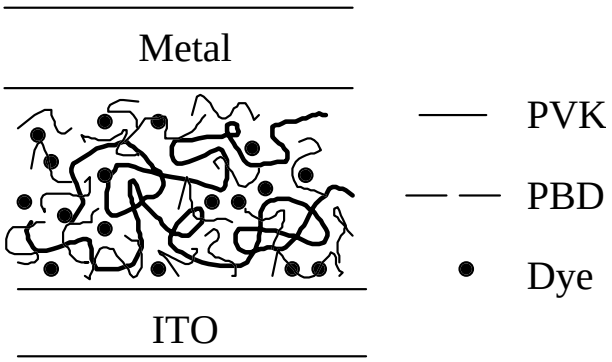

Figure 2.10: Schematic diagram of a mixed single layer polymer OLED that contains PVK, PBD and dye dopants. (From Ref. [4])

OLED is shown in Figure 2.11. The electrons and holes are injected from the Mg:Ag cathode and the ITO anode, respectively. They move across the device via hopping motion under the applied electric field [20].

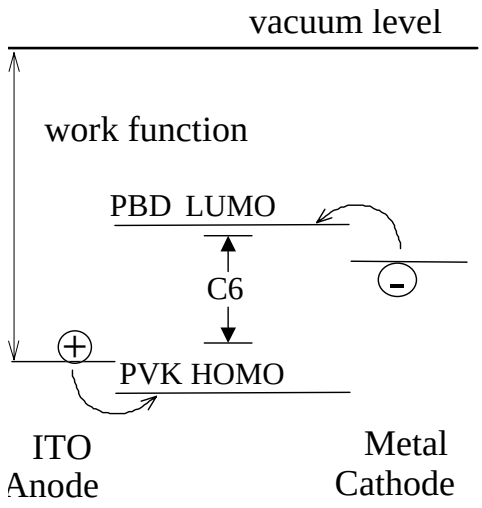

Figure 2.11: Energy level diagram of the single layer PVK/PBD/C6 device. (From Ref. [4])

The PBD content is optimized through the I–V characteristics of the OLED

(Figure 2.12), while the dye concentration is optimized through the EL efficiency of the OLED (Figure 2.13). The optimal concentration was found to be PVK:PBD:C6 = 100:40:0.3 by weight, from which OLEDs of external quantum efficiency in excess of 1% have been fabricated [4, 29].

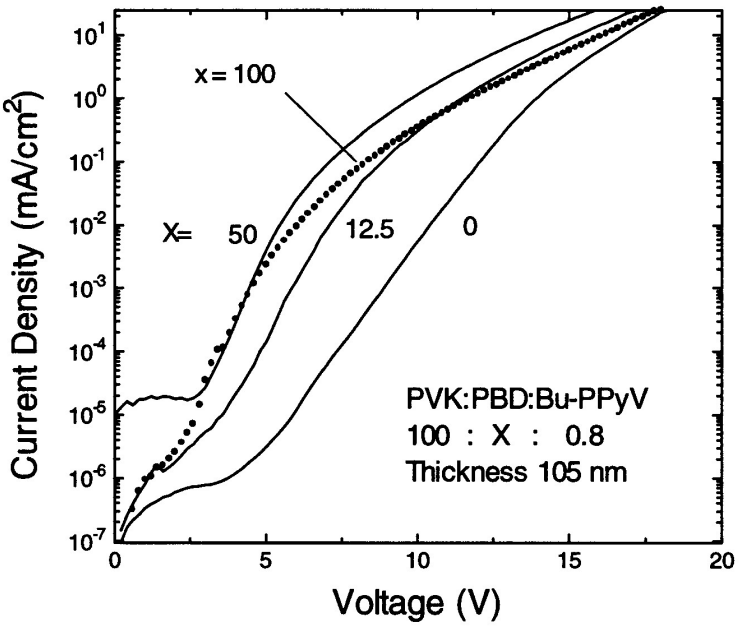

Figure 2.12: Forward I–V characteristics of ITO/PVK:PBD:Bu-PPyV (105 nm)/Mg:Ag (120 nm)/Ag (80 nm) devices of different PBD contents, where the weight ratio of PVK:PBD:Bu-PPyV is 100:X:0.8. (From Ref. [4])

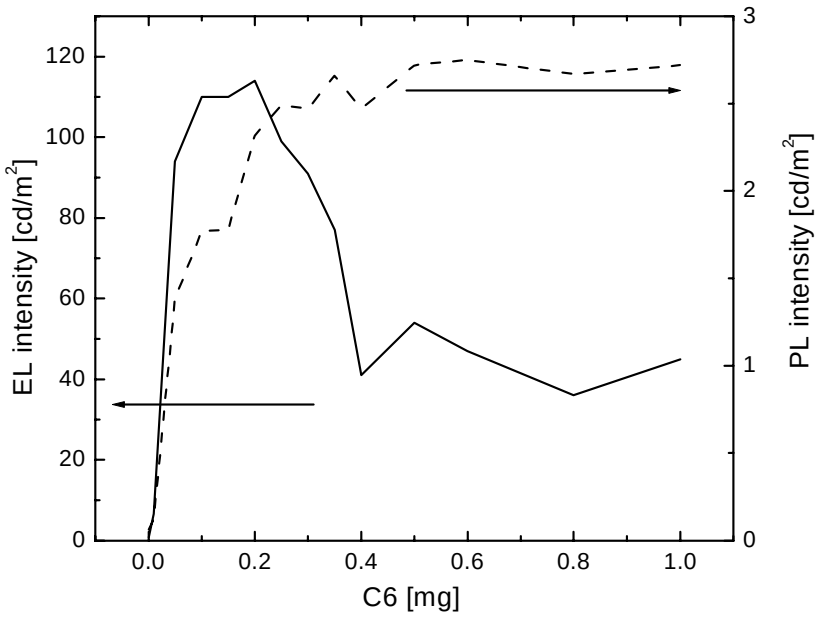

Figure 2.13: EL and PL intensity of PVK/C6 as a function of C6 content, measured in milligrams of C6 per 100 mg of PVK. Solid line: EL, dashed line: PL. (From F. Pschenitzka)

The discrepancy in dye concentration dependency in EL and PL (Figure 2.13) intensities suggests that the dye exciton creation and/or energy transfer mechanisms are different in the two instances. In PL, the excitons on C6 are most likely created by Förster energy from PVK. However, in EL, the proposed exciton creation mechanism is by carrier trapping on the dye dopant [4, 29]. In carrier trapping, the dye acts as a trap for either holes or electrons. When a current is passing through the device, one of the carriers is trapped at the dye and eventually recombines with the opposite carrier, forming an exciton on the dye molecule. This carrier trapping process can occur in parallel with energy transfer in a given device. The only requirement for efficient carrier trapping is that the dye dopant must have a HOMO energy higher than that of the host material or a LUMO energy lower than that of the host material [26].

Recently, O'Brien et al. observed a similar discrepancy in dye concentration dependence in EL and PL from PtOEP in polyfluorene based OLEDs. They arrived at the same conclusion that the Förster type of energy transfer mechanism is mainly responsible for the PL, whereas a carrier trapping mechanism is mainly responsible for the EL [33]

References

[1] M. Jones, Jr., *Organic Chemistry*, (W. W. Norton, New York, 1997).

[2] M. Pope and C. E. Swenberg, *Electronic Processes in Organic Crystals and Polymers*, (Oxford University Press, New York, 1999).

[3] P. W. Atkins, *Molecular Quantum Mechanics*, 3rd ed., (Oxford, New York, 1997).

[4] C.-C. Wu, *Light-Emitting Devices Based on Doped Polymer Thin Films* Ph.D Thesis, Elec. Eng., Princeton Univ., 1997).

[5] D. F. O'Brien and M. A. Baldo, *Appl. Phys. Lett.* **74**, 442 (1999).

[6] M. A. Baldo, D. F. O'Brien, Y. You, A. Shoustikov, S. Sibley, M. E. Thompson, and S. R. Forrest, *Nature* **395**, 151 (1998).

[7] M. A. Baldo, S. Lamansky, P. E. Burrows, M. E. Thompson, and S. R. Forrest, *Appl. Phys. Lett.* **75**, 4 (1999).

[8] M. A. Baldo, D. F. O'Brien, M. E. Thompson, and S. R. Forrest, *Phys. Rev. B* **60**, 14422 (1999).

[9] M. A. Baldo, M. E. Thompson, and S. R. Forrest, *Nature* **403**, 750 (2000).

[10] M. A. Baldo and S. R. Forrest, *Phys. Rev. B* **62**, 10958 (2000).

[11] M. A. Baldo, C. Adachi, and S. R. Forrest, *Phys. Rev. B* **62**, 10967 (2000).

[12] K. C. Kao and W. Hwang, *Electrical Transport in Solids* (Pergamon Press, Oxford, 1981).

[13] A. Kearwell and F. Wilkinson, *Transfer and Storate of Energies by Molecules*, (Pergamon Press, Oxford, 1981).

[14] S. P. McGlynn, T. Azumi, and M. Kinoshita, *Molecular Spectroscopy of the Triplet State*, (Prentice Hall, Englewood Cliffs, NJ, 1969).

[15] C. W. Tang and S. A. VanSlyke, *Appl. Phys. Lett.* **51**, 913 (1987).

[16] C. W. Tang, S. A. VanSlyke, and C. H. Chen, *J. Appl. Phys.* **65**, 3610 (1989).

[17] P. E. Burrows, Z. Shen, V. Bulovic, D. M. McCarty, S. R. Forrest, J. A. Cronin, and M. E. Thompson, *J. Appl. Phys.* **79**, 7991 (1996).

[18] E. A. Silinsh, *Organic Molecular Crystals*, (Springer, Berlin, 1980).

[19] L. J. Rothberg and A. J. Lovinger, *J. Mater. Res.* **11**, 3174 (1996).

[20] Y. Cao, I. D. Parker, G. Yu, c. Zhang, and A. J. Heeger, *Nature* **397**, 414 (1999).

[21] Z. Shuai, D. Beljonne, R. J. silbey, and J. L. Brédas, *Phys. Rev. Lett.* **84**, 131 (2000).

[22] M. Wohlgenannt, K. Tandon, S. Mazumdar, S. Ramasesha, and Z. V. Vardeny, *Nature* **409**, 494 (2001).

[23] J. H. Burroughes, D. D. C. Bradley, A. R. Brown, R. N. Marks, K, Mackay, R. H. Friend, P. L. Burns, and A. B. Holmes, *Nature* **347**, 539 (1990).

[24] P. L. Burn, A. B. Holmes, A. Kraft, D. D. C. Bradley, A. R. Brown, R. H. Friend, and R. W. Gymer, *Nature* **356**, 47 (1992).

[25] T. Förster, *Discussions Faraday Soc.* **27**, 7 (1959).

[26] A. A. Shoustikov, Y. You, and M. E. Thompson, *IEEE J. Sel. Quan. Elec* **4**, 3 (1998).

[27] M. Klessinger and J. Michel, *Excited States and Photochemistry of Organic Molecules* (VCH Publishers, New York, 1995).

[28] D. L. Dexter, *J. Chem. Phys.* **21**, 836 (1953).

[29] C. C. Wu, J. C. Sturm, R. A Register, J. Tian, E. P. Dana, and M. E. Thompson, *IEEE Trans. Elec. Dev.* **44**, 1269 (1997).

[30] J. Kido, M. Kohda, K. Okuyama, and K. Nagai, *Appl. Phys. Lett.* **61**, 761 (1992).

[31] J. Kido, H. Shionoyama, and K. Nagai, *Appl. Phys. Lett.* **67**, 2281 (1995).

[32] J. M. Pearson and M. Stolka, *Poly(N-vinyl-carbazole)* (Gordona and Breach Science Publishers, New York, 1981).

[33] D. F. O'Brien, C. Giebler, R. B. Fletcher, A. J. Cadby, L. C. Palilis, D. G. Lidzey, P. A. Lane, D. D. C. Bradley, and W. Blau, *Syn. Met.* **116**, 379 (2001).

[34] V. D. Lakhno, Ed. *Excited Polaron States in Condensed Media* (Manchester University Press, Manchester, 1991).

[35] E. I. Rashba and M. D. Sturge, *Excitons* (North-Holland Publishing, Amsterdam, 1982).

Chapter 3

OLED Technology Development

3.1 Introduction

The majority of the device development work described in this chapter is motivated both by the need to verify the results of the combined classical and quantum mechanical microcavity (CCQMM) model (see Chapter 4), and by the need in our research group for an efficient device for display technology demonstrations. In the CCQMM model, the exact location of the emitting center is crucial; therefore, a bilayer device was developed where the exciton profile is controlled by the location of the hole transport layer/electron transport layer (HTL/ETL) interface. Secondly, lithium fluoride/aluminum (LiF/Al) cathodes were developed for their superior electron injection abilities [21]. Lastly, since the index of refraction of the substrate is an important parameter in the model, a room-temperature ITO deposition process was developed so that OLEDs can be fabricated on plastic or

specialty glass substrates that are not pre-coated with ITO.

This chapter is organized as follows: after a discussion of the fabrication equipment and measurement apparatus in Sec. 3.2, the fabrication of the bilayer OLEDs based on PVK and Alq_3 will be discussed in detail in Sec. 3.3. Also included in Sec. 3.3 is the development of LiF/Al cathodes. Finally, the room-temperature ITO deposition process, the characteristics of the resulting films and the OLEDs fabricated on them are discussed in Sec. 3.4.

3.2 Fabrication equipment and measurement apparatus

Most of the device fabrication centers on two pieces of equipment: a dry nitrogen-filled glovebox (Terra Universal) and a four-source evaporator. The glove box consists of two sides connected by a load lock (Figure 3.1).

One side of the glove box houses a spinner, where spin-casting of polymer layers take place. The other side houses a probe station where the OLEDs can be characterized in a dry nitrogen atmosphere. The water vapor content in the glovebox is approximately 30 ppm as estimated from dew point measurements (Terra Universal). OLED luminous output is detected by a large-area, broad-band, Si photodiode (UDT PIN10-DP). The luminance–current density–voltage (L–J–V) curves are measured and recorded by an HP 4145B semiconductor parameter

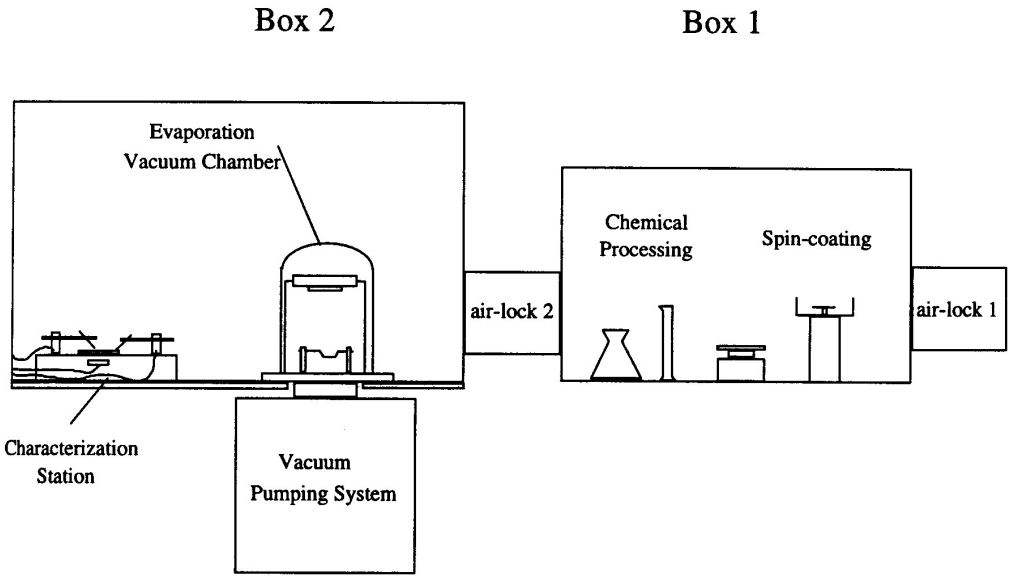

Figure 3.1: Schematic diagram of the nitrogen-filled glovebox.

analyzer.

Both small molecule organic materials and metals (Alq_3, LiF, Mg, Ag, and Al) are evaporated in a 4-source evaporator manufactured by Angstrom Engineering (Cambridge, ON, Canada). Each source consists of a resistively-heated boat (tungsten or tantalum, R. D. Mathis Corp.) and its own power supply. The rotatable sample stage, which holds substrates facing down, is situated at the top of the chamber. The sample-source distance is approximately 30 cm. Each of the 4 sources and the sample stage has its own shutter and quartz crystal thickness monitor. The evaporator is equipped with a cryogenic pump and base pressures better than 10^{-7} Torr are routinely achieved. The system is controlled by a personal computer which is capable of running both pre-programmed and manual

evaporation sequences.

PL and EL spectra are measured by a Photoresearch PR650 colorimeter. The optics of the colorimeter allows it to measure the luminance of a spot that subtends a 1.5° field of view. This translates to a spot size of <1 mm at a focal length around 6 cm.

3.3 Hybrid bilayer OLEDs based on PVK/Alq_3

The early focus in our group has been single layer, doped polymer (PVK/PBD/C6) OLEDs [1, 2]. Their chemical structures or PVK, PBD and C6 are shown in Figure 2.9. Reasonable external efficiencies in excess of 1%, and color tuning by appropriate choice of dye dopants such as nile red and C47 have been demonstrated [1, 2]. On the other hand, OLEDs with HTL/ETL heterojunctions allow independent tuning of the injection and transport of both electrons and holes, which generally results in higher external quantum efficiencies. Another important advantage of these bilayer devices is that the location of the emission zone is precisely controlled by the heterojunction, whereas in single layer devices the emission zone is sensitively dependent upon the balance of injection and transport of both carriers [3]. It will be shown in Chapters 4 and 5 that the location of the emission zone is crucial to the external coupling of light emission in the OLED.

The seminal work on small molecule OLEDs by Tang et al. was based on a bilayer heterojunction where an aromatic diamine served as the HTL and Alq_3

either alone or doped with a fluorescent dye served as the ETL and the emitting layer (EML) (Figure 3.2) [4, 5].

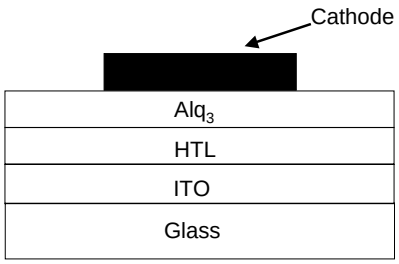

Figure 3.2: Schematic diagram of a mall molecule bilayer OLED based on Alq_3 and an HTL.

Alq_3 is by far the most widely studied small molecule electro-fluorescent material for use in OLEDs (Figure 3.3). A number of other HTL/Alq_3

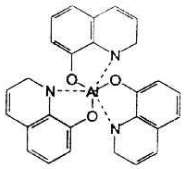

Figure 3.3: Chemical structures of Alq_3.

combinations have been investigated extensively, of which N,N'-diphenyl-N,N'-(3-methylphenyl)-1,1'-biphenyl-4,4'diamine (TPD) and 4,4'=bis[N-(1-naphyl)-N-phenyl-amino]biphenyl (α-NPD) are two of the most popular small molecule HTLs [6, 7]. Polymer HTLs, such as and poly-(phenylene vinylene) (PPV) [8]-[13], have also been used in conjunction with Alq_3 to make what is called "hybrid" OLEDs — in the sense that these systems employ both small molecule and polymer materials.

Bilayer OLEDs based on PVK/Alq_3 were a natural choice due to our exist-

ing knowledge base in processing PVK, and the oxygen plasma treatment of ITO surfaces for optimal hole injection into PVK [10]. It is not a common material system: there is one report by Liu et al. who used PVK/Alq_3 OLEDs to study device aging and cathode forming processes [14]. Their devices had poor performance due to the use of untreated ITO and pure aluminum cathodes.

3.3.1 Substrates and cleaning procedures

The standard glass substrates used for OLED fabrication are purchased from Applied Films Corp. (Boulder, CO). They are made of soda lime glass and come in two thicknesses, 0.7 mm and 1.1 mm. The ITO layer thicknesses range from 120 nm to 180 nm and the nominal sheet resistances range from 15 to 30 Ω/sqare. Cleaning the substrates involves a number of steps. After a vigorous scrubbing with Tergitol (J. T. Baker) and a cotton swab, the substrate is sent through sonication in trichloroethylene, acetone and isopropanol for 10 min each at slightly elevated temperatures (40 - 50°C). The substrate is blown dry with dry nitrogen in between these steps. Finally, the substrate is placed in a Plasma Technology reactive ion etcher with 10 in anodized Al electrodes for an oxygen plasma treatment. The standard plasma parameters are: oxygen flow rate = 25 sccm, pressure = 150 mTorr, rf power = 25 W, and time = 4 min [1, 10].

In some experiments, OLEDs need to be fabricated on unconventional substrates, such as 175 μm polycarbonate (PC) films purchased from Goodfellows

Corp. (PA) and Schott SFL57 glass substrates purchased from Sydor Optics. ITO films are deposited onto these substrates before OLED fabrication (see Section 3.4). Before ITO deposition, PC films are scrubbed with Tergitol and rinsed in DI water, but not exposed to any of the solvents, for even the slightest reaction may alter the surface morphology. The bare glass slides are cleaned by scrubbing with Tergitol and solvent rinse/sonication. After ITO deposition, the substrates are treated with the oxygen plasma before OLED fabrication.

3.3.2 Spin-coating PVK

PVK layers are spun-cast on oxygen plasma treated ITO-coated glass substrates. The PVK is purchased from Aldrich (Mw = 69,000, secondary standard). Chlorobenzene (CB) is used as the solvent. Previously, chloroform was used as the solvent in single layer PVK/PBD/C6 devices [1, 2]. There are a number of factors that precipitated this change. First, it has been reported that spin-casting of poly(phenylene vinylene) (MEH-PPV) from a chloroform solution led to aggregate formation in the resultant film and red-shifted EL spectra. It was theorized and shown through numerical simulation that due to the non-aromatic nature of chloroform, aromatic polymers such as MEH-PPV bundles up in the solution which led to aggregate formation. Conversely, MEH-PPV in an aromatic solvent such as dicholorobenzene (DCB) was shown to have an extended structure which was preserved in the spun-cast films [15, 16]. Due to the aromatic nature of the carbazole group

in PVK, it was expected that an aromatic solvent such as CB will also suppress aggregate formation in the spun-cast PVK films. Chloroform is acidic, and is know to react with PVK over a period of time [17]. Anecdotal observation indicates that PVK/chloroform solution starts turning slightly yellow from totally clear after approximately one week, after which OLEDs made from the said solution have markedly lower external efficiencies. On the other hand, devices made from PVK/CB solutions that were up to one month old have the same characteristics as those made from fresh PVK/CB solutions. Additionally, CB is less volatile than chloroform and generally the films spun-cast from CB are more uniform as indicated by visual inspection.

The thicknesses of various spun-cast PVK films were measured by a Sloan Dektak III stylus profilometer and plotted against spin rate and solution concentration in Figure 3.4. The PVK layer in most of the bilayer OLEDs in this thesis were spun-cast from a 7.5 mg/ml solution at 2000 RPM, which gives a film approximately 40–45 nm thick.

3.3.3 Alq_3 evaporation

Alq_3 from two vendors was used: Aldrich (99.995% pure) and TCI America. It is used as received. The Alq_3 from TCI America has higher purity and made more efficient OLEDs. Unless otherwise stated, the Alq_3 used is from this vendor. Another high-quality vendor, H. W. Sands, has also been identified. Alq_3 is evap-

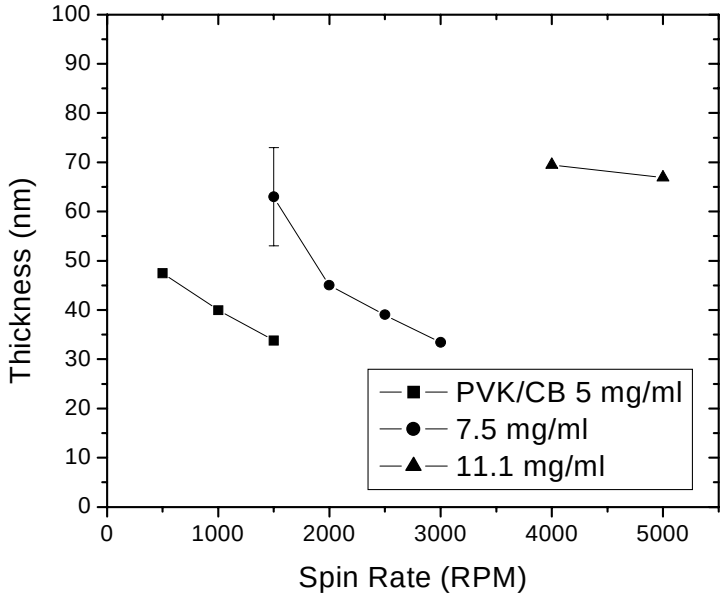

Figure 3.4: Thickness of the PVK film *vs.* spin rate and solution concentration. The solvent is chlorobenzene.

orated (sublimed) at a base pressure better than 10^{-6} Torr, at a rate of 0.1 - 0.3 nm/s. Faster deposition rates, such as 1 nm/s, leads to less efficient devices. The structural defects created by rapid deposition are thought to increase non-radiative recombination of excitons.

The electroluminescence (EL) spectrum of these bilayer OLEDs and the photoluminescence spectrum of a single layer of Alq_3 evaporated onto a Si wafer are compared in Figure 3.5. They coincide very well, which indicates that the EL comes exclusively from the Alq_3.

The external quantum efficiency of OLEDs, η_{EL}^{ext}, can be calculated from the measured photocurrent [1]. The external quantum efficiency is plotted along with the J–L–V of OLEDs with Alq_3 layer thickness ranging from 20 to 80 nm (Figure

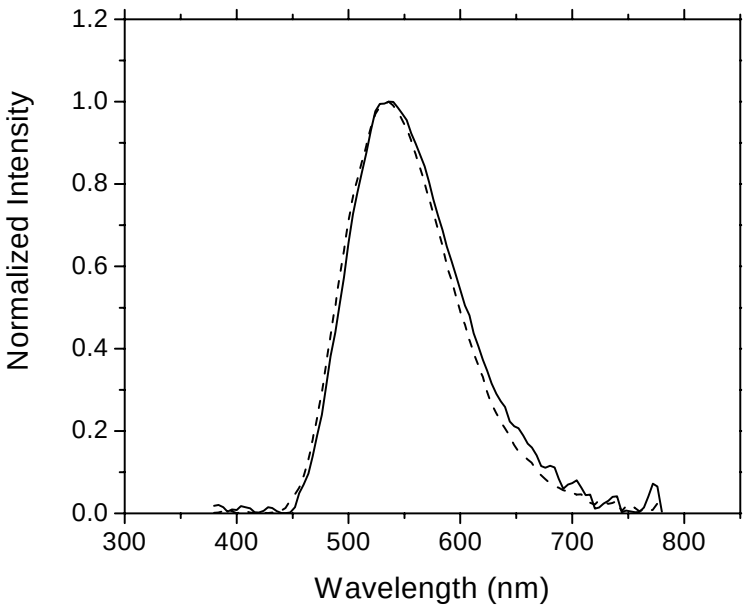

Figure 3.5: Normalized PL (solid line) and EL spectra (dashed line) from pure Alq_3 and PVK/Alq_3 bilayer devices. From the excellent match of the two spectra it can be concluded that the EL is exclusively from Alq_3.

3.6). η_{EL}^{ext} increases monotonically with Alq_3 thickness. At $J = 100$ mA/cm^2, η_{ext} ranges from 0.22% for a device with a 20 nm layer Alq_3 to 0.9% for a device with an 80 nm layer Alq_3. The theoretical explanation for this dependence will be discussed in detail in Chapters 4 and 5. At the same time, the drive voltage at the same current density increases from 8.8 V to 14.4 V. This increase is due to the extra voltage drop across the thicker Alq_3 layer. The highest power efficiency is generally obtained at an Alq_3 thickness around 50 nm [18].

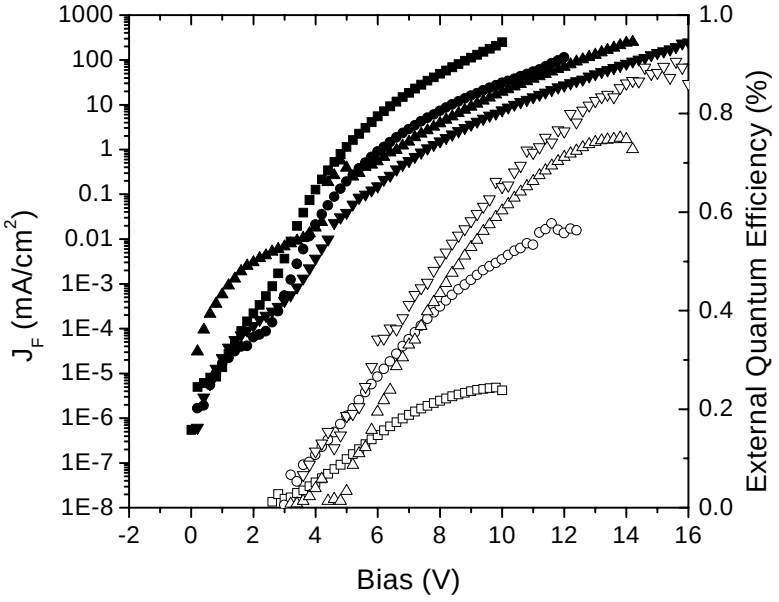

Figure 3.6: J–V (solid symbols) and external quantum efficiency (open symbols) of bilayer devices of the structure: soda lime glass/180 nm ITO/40 nm PVK/Alq_3 (Aldrich)/Mg:Ag/Ag as a function of Alq_3 thickness. Squares: 20-nm-thick-Alq_3, circles: 40 nm, up triangles: 60 nm, and down triangles: 80 nm.

3.3.4 Lithium fluoride/aluminum cathodes

Electron injection layers (EIL) are thin layers of material inserted between the cathode and the ETL to improve the injection of electrons. Inorganic insulators like Al_2O_3, SiO_2, and Li_2O, as well as polymers, have been used as EILs [19, 20]. One of the most effective EILs is a layer of thin LiF inserted between an aluminum cathode and Alq_3 [21]. Other alkali metal halide compounds have been tried as EILs, or co-evaporated with aluminum to form composite cathodes [22]-[24]. Pure lithium and lithium-doped Alq_3 have also been tried with good results; however, the difficulty in handling lithium limits the practical use of these systems [25]-[27]. Recently, good results with LiF/Al cathodes have also been obtained in polyfluorine-based polymer OLEDs [28]. One proposed mechanism is that the evaporated Al reacts with LiF to form AlF_3 and releases Li, which then react with Alq_3 to form Alq_3 anions which facilitate electron injection [29]. To that extent, even an Al layer as thin as 0.1 nm has been show to activate LiF [30]. However, this still remains an area of active investigation [31].

Powder form LiF is purchased from Alfa Aesar and stored in a dry ambient (load-lock of the nitrogen glove box), since it readily absorbs water. LiF can be thermally evaporated easily from a tungsten boat. OLEDs with LiF/Al cathodes are fabricated as follows: after spin-coating 40 nm PVK onto cleaned ITO substrates and a blanket evaporation of 50 nm Alq_3, the vacuum is broken and a shadow mask with 2x2 mm^2 holes is loaded on top of the samples. Then LiF

is evaporated at a rate of 0.05 nm/s for a total of 0.5-1.5 nm while the substrate stage is rotating. Finally, 100 nm of Al is evaporated. The L–J–V curves of these OLEDs are shown in Figure 3.7. It is clear from comparing the symbols and

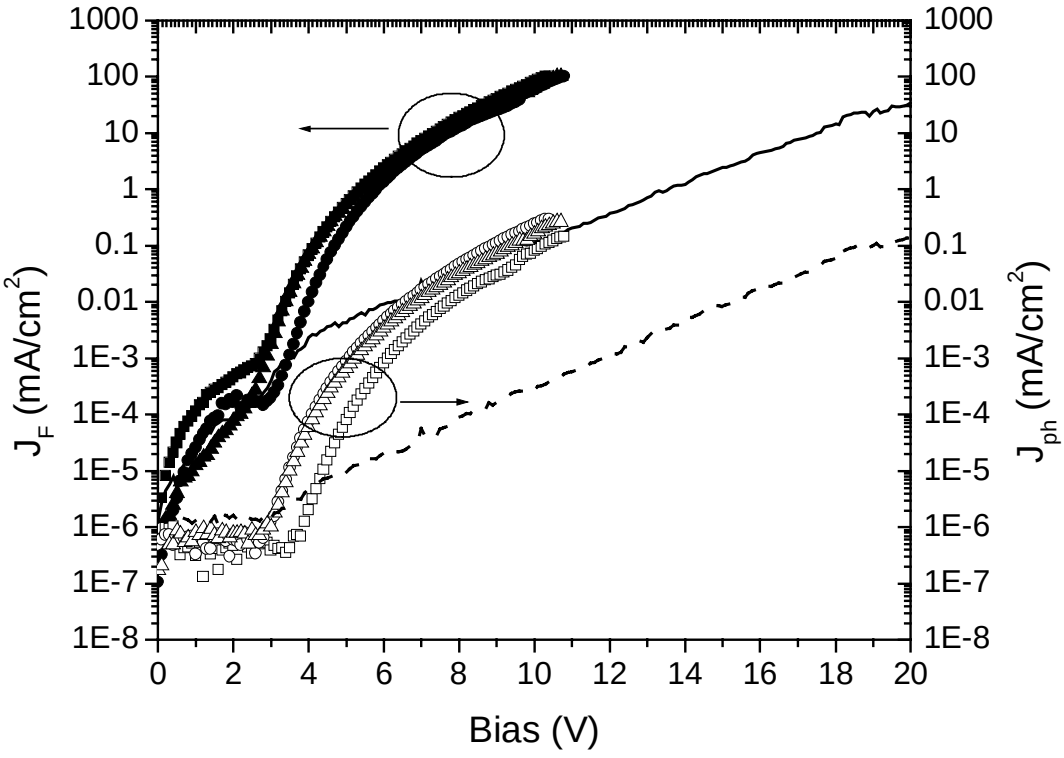

Figure 3.7: L–J–V curves of bilayer devices of the structure: soda lime glass/160 nm ITO/40 nm PVK/50 nm Alq_3 (Aldrich) /LiF/Al for several LiF thicknesses. The forward current is represented by solid symbols, and the photo current by the open symbols. Squares: 0.5-nm-thick-LiF, circles: 1.0 nm, and up triangles: 1.5 nm. The forward and photo current of the control device (pure Al cathode) are represented by the solid and dashed lines, respectively.

lines in Figure 3.7 that the addition of even 0.5 nm of LiF between the Al cathode and Alq_3 brings about a tremendous increase in both the forward current and luminous output of the device. Similar to that observed by Hung et al. [21], the

devices with a 1.0 nm LiF layer have the highest forward current and luminous efficiency, although the difference between the devices with 1.0 or 1.5 nm LiF is small. In the device with 1.0 nm LiF, the turn-on voltage, defined as the onset of measurable photocurrent, is 2.3 V, and the voltage at $J = 10$ mA/cm^2 is 7.3 V, at which point the luminance is 150 cd/m^2, corresponding to an external efficiency of 0.5%.

3.3.5 Comparison with single layer devices

Using a purer supply of Alq_3 (from TCI America) and minimizing the delay between spin-casting the PVK film and loading the samples into the evaporator, device performance can be drastically improved. The evaporation rates for Alq_3, LiF and Al are 0.1 nm - 0.3 nm/s, 0.05 nm/s and 0.5 nm/s, respectively. No other special handling is required. Figure 3.8 compares the L–J–V curves of bilayer devices with either Mg:Ag or LiF/Al cathodes with single layer PVK/PBD/C6 devices. Both bilayer devices have turn-on voltages around 2.3 V, compared with 4.8 V for the single-layer device. The current density $J = 10$ mA/cm^2 is reached at 4.9 V, 5.4 V and 13.7 V for the bilayer device with LiF/Al cathodes, Mg:Ag cathodes, and the single layer device, respectively. The luminance values at this current density are, 300 cd/m^2, 220 cd/m^2 and 160 cd/m^2, corresponding to external quantum efficiencies of 1.0%, 0.7% and 0.5% (note the efficiency of the single layer OLED is lower than the results obtained by C.-C. Wu whose best

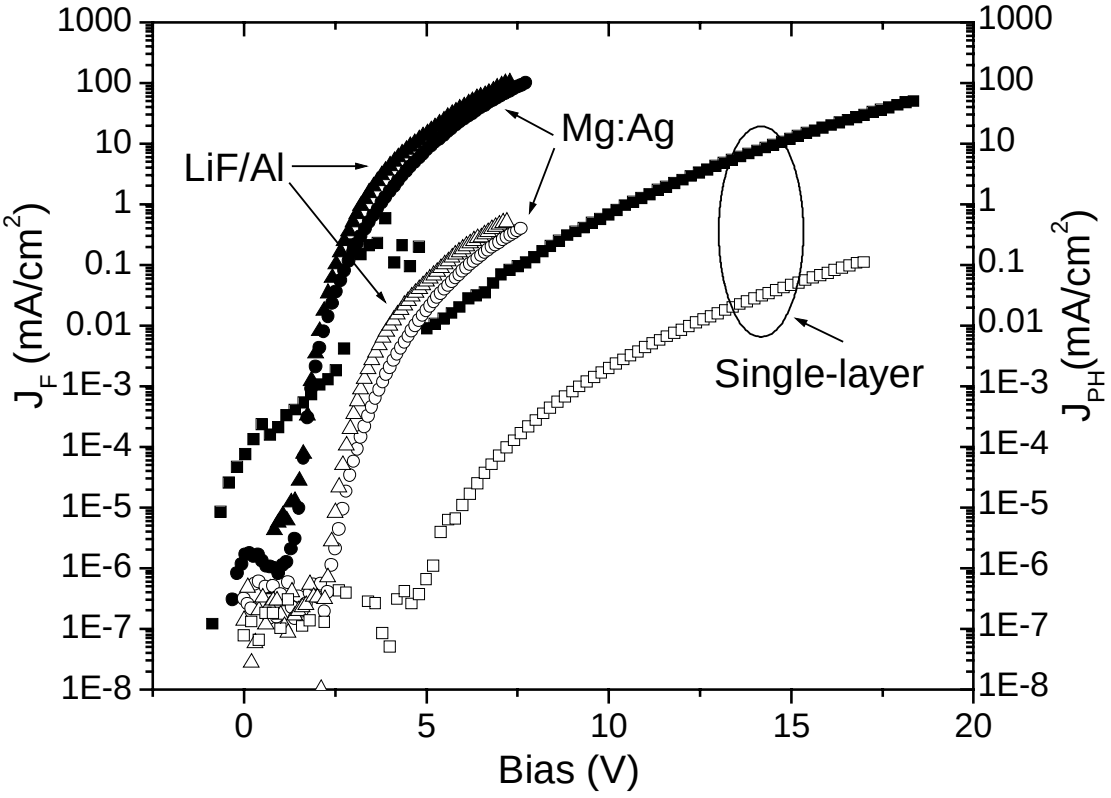

Figure 3.8: L–J–V of a single layer device (squares: soda lime glass/120 nm ITO/100 nm PVK/PBD/C6/Mg:Ag/Ag) compared with two bilayer devices (circles: soda lime glass/120 nm ITO/40 nm PVK/50 nm Alq_3/Mg:Ag/Ag, and triangles: soda lime glass/120 nm ITO/40 nm PVK/50 nm Alq_3/1 nm LiF/Al). The forward current is represented by solid symbols, and the photocurrent divided by the OLED area by the open symbols.

single layer devices are up to 1% in external efficiency [1, 2]), respectively. The results from these hybrid bilayer OLEDs are comparable with the bilayer OLEDs based on Alq_3/NPD [32].

The external efficiencies of the three devices examined above is plotted against the forward current density in Figure 3.9. C.-C. Wu found that the luminance of single layer OLEDs is linear with current for several orders of magnitude

[1]. A flat region in the efficiency *vs.* current density curve for the single layer device is also observed here. However, for both bilayer devices the efficiency increases linearly with drive current. The currents in these PVK/Alq_3 devices are most likely hole-dominated just as in other HTL/Alq_3 devices [33], and higher drive levels tend to balance the hole and electron currents, resulting in a more efficient device.

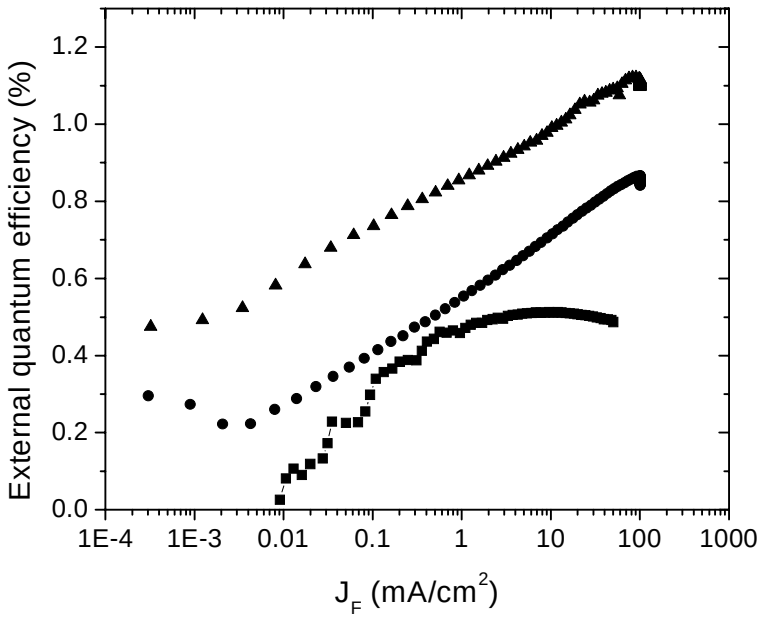

Figure 3.9: External quantum efficiency as a function of current density (squares: soda lime glass/120 nm ITO/100 nm PVK/PBD/C6/Mg:Ag/Ag, circles: soda lime glass/120 nm ITO/40 nm PVK/50 nm Alq_3/Mg:Ag/Ag, and up triangles: soda lime glass/120 nm ITO/40 nm PVK/50 nm Alq_3/1 nm LiF/Al).

3.4 ITO deposition

3.4.1 ITO deposition methods

ITO can be deposited by a number of techniques including ion beam sputtering, pulsed laser ablation, and DC magnetron sputtering [34]-[38]. In a research lab setting, the most commonly used deposition method is rf magnetron sputtering. The dependence of film quality on deposition parameters such as gas composition, gas pressure, rf power, target-sample distance, and post annealing has been studied in detail [39]-[52]. Under optimized conditions, which typically involve using a gas mixture of argon with a small amount ($\leq$ 1%) of oxygen, a 150-nm film of ITO has a transparency of >90% in the visible, and a resistivity of 6.8×10^{-5} Ω cm, corresponding to a sheet resistance of 4.5 Ω/sq [40]. Substrate heating during deposition (250°C) or post annealing (400°C, 1 hr) were required to achieve these results [40, 43]. ITO films sputtered in pure Ar plasma have a typical resistivity of 2×10^{-3} Ω cm [39, 48]. Nanto et al. obtained excellent room-temperature results by using an external DC magnetic field coupled to the rf magnetron. They reported films with resistivities of 2×10^{-4} Ω cm and transparency of >85% when the ITO films were sputtered from a 95% In_2O_3-5% SnO target in a 3.4 mTorr, 0.8% O_2-Ar plasma at 50 W rf power and an external DC magnetic field of 150 gauss [43].

The purpose of developing our own ITO deposition capabilities was to demonstrate the dependence of the distribution of light emission into various modes

(Chapter 4) on the index of refraction of the substrate. To that end, it was only necessary to obtain an ITO film of sufficient transparency and conductivity so that OLEDs fabricated on them have measurable and stable luminous output. The deposition procedure, the characteristics of the films, and the OLEDs fabricated on them is discussed in the following section.

3.4.2 ITO films by room temperature rf magnetron sputtering

An Edwards 306A deposition chamber equipped with an rf magnetron cathode assembly was used for ITO deposition. ITO was sputtered from a 3-inch 90% In_2O_3-10% SnO target (Target Materials America). A pure Ar plasma at 2 mTorr was used for all depositions. The base pressure was better than 10^{-6} Torr, and the target was pre-sputtered for 20 min before actual deposition to remove any impurities on its surface. The substrate was soda lime glass. The deposition was carried out without intentional heating or cooling. Some of the ITO coated substrates were post-annealed in a vacuum chamber at 400°C for 1 hour.

The recipes for ITO deposition are outlined in Table 3.1. The parameter with the most impact on film quality and uniformity is the sample-target distance. As the ITO atoms are knocked off the target by argon ion bombardment, they are thermalized, i.e., their kinetic energy is lost through collision with Ar atoms or ions in the plasma until reaching an equilibrium. When the sample-target distance is

less than the thermalization distance, the ITO atoms arrive at the substrate with considerable kinetic energy, which translates into surface mobility and enhanced crystallinity of the resultant film [44]. The thermalization distance is a function of both pressure and rf power. At a pressure of 2 mTorr and rf power of 150 W the thermalization distance is in excess of 10 cm [44], but a strong dependence of the kinetic energy of ITO atoms impinging on the substrate on the sample-target distance is still to be expected. Too much kinetic energy carried by the ITO atoms can knock off oxygen in the film and produce "darkened" films [48]. This is just one example of the inter-dependence of the transparency and conductivity of the ITO films.

Table 3.1: Recipes for depositing ITO films.

Recipe	Pressure (mTorr)	rf power (W)	Sample-target distance (cm)	Time (min)
1	2	150	5	2
2	2	125	5	2
3	2	175	5	2
4	2	150	3.5	2
5	2	150	6.5	2
6	2	150	5	3

The electrical characteristics of these ITO films are summarized in Table 3.2. The sheet resistance of the ITO films were measured by the 4-point probe method, and their Hall mobility by the van der Pauw method [53, 54]. The increase in the carrier density and decrease in carrier mobility due to annealing was also observed elsewhere [43]. More systematic studies are required to correlate film characteristics with deposition parameters.

Table 3.2: Characteristics of the ITO films deposited.

Recipe	Thickness (nm)	Resistivity (10^{-3} ohm-cm)		Mobility (cm^2/Vs)		n (10^{20} cm^{-3})	
		Before anneal	After anneal	Before anneal	After anneal	Before anneal	After anneal
1	110	1.4	1.1	210	1	0.22	54
2	100	5.7	0.57	18	1.8	0.7	61
3	150	21	0.58	16	2.3	0.19	48
4	145	4.2	0.48	22	2.3	0.67	58
5	90	1.7	0.98	33	0.24	1.1	260
6	250	6.4	0.79	20	1.8	0.49	72

The transmission of the films 1 and 5 along with a substrate purchased from Applied Films Corp. was measured with a Hitachi spectrophotometer and is shown in Figure 3.10. The transmissivity is that of the ITO-coated soda lime glass substrates normalized to that of air. The Applied Films substrate is fairly transparent, averaging 85-90% in the visible. Recipe 1 yielded films only 70-75% transparent, while recipe 5 yielded films that are $\sim$80% transparent. The difference in the peaks of transmission are from microcavity effects. The Applied Films ITO has an index of refraction of 1.8 and a thickness of 180 nm. Both recipes 1 and 5 yielded ITO with an index of refraction of 2.0 as measured from ITO films deposited on a Si wafer by ellipsometry.

The L–J–V curves of OLEDs (ITO/40 nm PVK/50 nm Alq_3/LiF/Al) fabricated on unannealed ITO films from recipes 3 to 6 are plotted in Figure 3.11. The voltage required to reach $J = 10$ mA/cm^2 ranges from 9.6 V in recipe 4 to 12.1 V in recipe 5, compared with 7.3 V for identical OLEDs deposited on ITO films purchased from Applied Films Corp. The external quantum efficiencies are similar, all at around 0.5%.

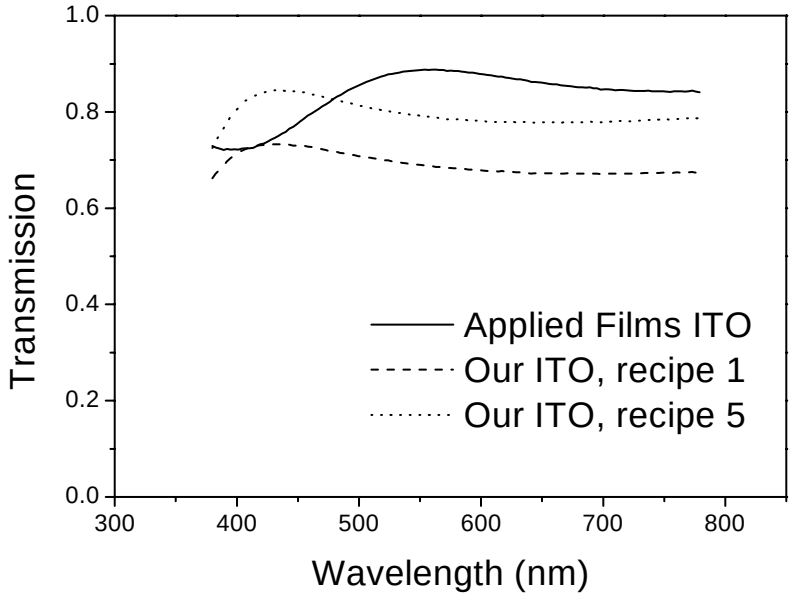

Figure 3.10: Transmission in the visible of 3 ITO-coated glass substrates: Applied Films substrate (t_{ITO} = 180 nm) and those from recipies 1 and 5. The substrate is 1.1 mm soda lime glass, and the reference (100%) is the transmissivity of air.

Recipe 5 has the highest as-deposited conductivity, it also has good transparency and uniformity. So it was chosen for all experiments involving ITO deposition despite having the highest driving voltage among the OLEDs shown in Figure 3.11.

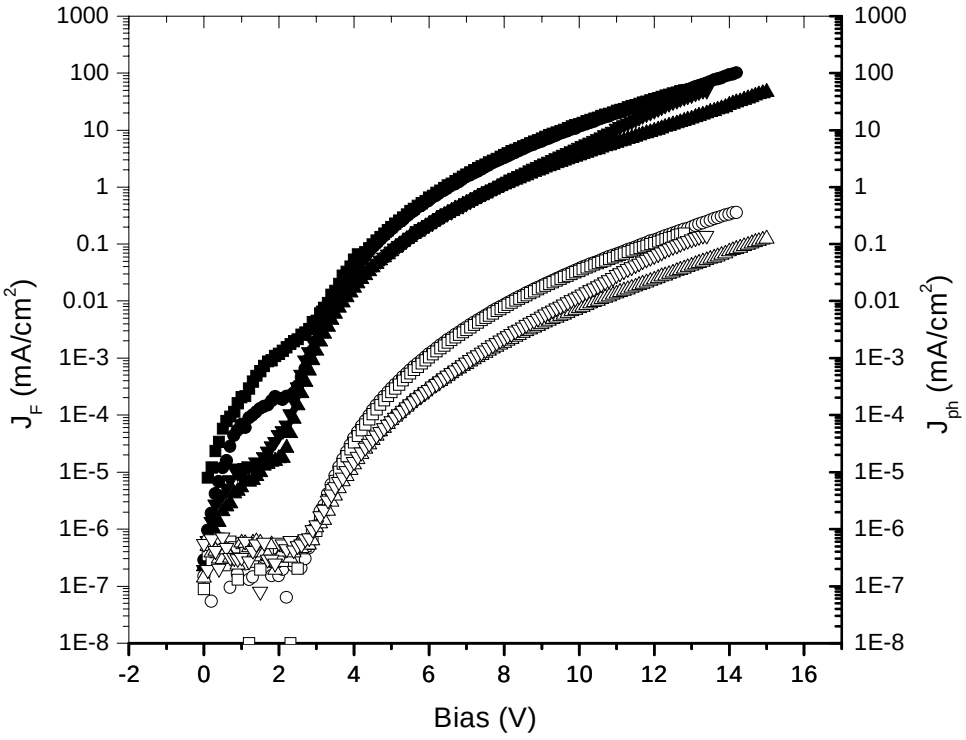

Figure 3.11: L–J–V curves from OLEDs fabricated on room temperature sputtered ITO films: squares: recipe 3, circles: recipe 4, up triangles: recipe 5, down triangles: recipe 6. OLED structure: ITO/40 nm PVK/50 nm Aldrich Alq_3 Mg:Ag.

References

[1] C.-C. Wu, *Light-Emitting Devices Based on Doped Polymer Thin Films*, (Ph.D Thesis, Elec. Eng., Princeton Univ., 1997).

[2] C. C. Wu, J. C. Sturm, R. A Register, J. Tian, E. P. Dana, and M. E. Thompson, *IEEE Trans. Elec. Dev.* **44**, 1269 (1997).

[3] G. G. Malliaras and J. C. Scott, *J. Appl. Phys.* **83**, 5399 (1998).

[4] C. W. Tang and S. A. VanSlyke, *Appl. Phys. Lett.* **51**, 913 (1987).

[5] C. W. Tang, S. A. VanSlyke, and C. H. Chen, *J. Appl. Phys.* **65**, 3610 (1989).

[6] J. Kido and Y. Iizumi, *Appl. Phys. Lett.* **73**, 2721 (1998).

[7] V. Bulović, R. Deshpande, M. E. Thompson, and S. R. Forrest, *Chem. Phys. Lett.* **308**, 317 (1999).

[8] S. E. Shaheen, G. E. Jabbour, B. Kippelen, N. Peyghambarian, J. D. Anderson, S. R. Marder, N. R. Armstron, E. Bellmann, and R. H. Grubbs, *Appl. Phys. Lett.* **74**, 3212 (1999).

[9] G. E. Jabbour, S. E. Shaheen, M. M. Morrell, J. D. Anderson, P. Lee, S. Thayumanavan, S. Barlow, E. Bellmann, R. H. Grubbs, B. Kippelen, S. Marder, N. R. Armstron, and N. Peyghambarian, *IEEE J. Quan. Elec.* **36**, 1 (2000).

[10] C. C. Wu, C. I. Wu, J. C. Sturm and A. Kahn, *Appl. Phys. Lett.* **70** 1348 (1997).

[11] C. C. Wu, J. K. M. Chun, P. E. Burrows, J. C. Sturmk M. E. Thompson, S. R. Forrest, and R. A. Register, *Appl. Phys. Lett.* **66**, 653 (1995).

[12] X. Jiang, Y. Liu, X. Song, and D. Zhu, *Solid State Comm.* **99**, 183 (1996).

[13] T. Zyung, S.-D. Jung, and D.-H. Hwang, *Synth. Met.* **117**, 223 (2001).

[14] X. Liu, W. Li, J. Yu, J. Peng, Y. Zhao, g. Sun, x. Zhao, Y. Yu, and G. Zhong, *Jpn. J. Appl. Phys. pt. 1* **37**, 6633 (1998).

[15] Y. Shi, J. Liu, and Y. Yang, *J. Appl. Phys.* **87**, 4254 (2000).

[16] J. Liu, Y. Shi, L. Ma, and Y. Yang, *J. Appl. Phys.* **88**, 605 (2000).

[17] R. Kwong, private communication.

[18] V. Bulović, V. B. Khalfin, G. Gu, P. E. Burrows, D. Z. Garbuzov, and S. R. Forrest, *Phys. Rev. B* **58**, 3730 (1998).

[19] Y.-E. Kim, H. Park, and J.-J. Kim, *Appl. Phys. Lett.* **69**, 599 (1996).

[20] F. Li, H. Tang, J. Anderegg, and J. Shinar, *Appl. Phys. Lett.* **70**, 1233 (1997).

[21] L. S. Hung, C. W. Tang, and M. G. Mason, *Appl. Phys. Lett.* **70**, 152 (1997).

[22] T. Wakimoto, Y. Fukuda, K. Nagayama, A. Yokoi, H. Nakada, and M. Tsuchida, *IEEE Trans. Elec. Dev.* **44**, 1245 (1997).

[23] G. E. Jabbour, Y. Kawabe, S. E. Shaheen, J. f. Wang, M. M. Mrrell, B. Kippelen, and N. Peyghambarian, *Appl. Phys. Lett.* **71**, 1762 (1997).

[24] G. E. Jabbour, B. Kippelen, N. R. Armstrong, and N. Peyghambarian, *Appl. Phys. Lett.* **73**, 1185 (1998).

[25] F. G. Celii and S. J. Jacobs, *Soc. Info. Disp. Symp. Dig.*, 314 (1997).

[26] P. F. Seidler, E. I. Haskal, A. Curioni, and W. Andreoni, *Soc. Info. Disp. Symp. Dig.*, F-5 (1997).

[27] J. Kido and T. Matsumoto, *Appl. Phys. Lett.* **73**, 2866 (1998).

[28] T. M. Brown, R. Friend, I. S. Millard, D. J. Lacey, J. H. Burroughes, and F. Cacialli, *Appl. Phys. Lett.* **77**, 3096 (2000).

[29] M. G. Mason, C. W. Tang, L.-S. Hung, P. Raychaudhuri, J. Madathil, D. J. Giesen, L. Yang, Q. T. Lee, Y. Gao, S.-T. Lee, L. S. Liao, L. F. Cheng, W. R. Salaneck, D. A. dos Santos, and J. L. Brédas, *J. Appl. Phys.* **89**, 2756 (2001).

[30] L. S. Hung, C. W. Tang, M. G. Mason, P. Raychaudhuri, and J. Madathil, *Appl. Phys. Lett.* **78**, 544 (2001).

[31] G. Parthasarathy, C. Shen, A. Kahn, ans S. R. Forrest, *J. Appl. Phys.*, (2001).

[32] J. Shi and C. W. Tang, *Appl. Phys. Lett.* **70**, 1665 (1997).

[33] S. A. Van Slyke, C. H. Chen, and C. W. Tang, *Appl. Phys. Lett.* **69**, 2160 (1996).

[34] M. Higuchi, S. Uekusa, R. Nakano, and K. Yokogawa, *J. Appl. Phys.* **74**, 6710 (1993).

[35] M. Rottmann and K. Heckner, *J. Phys. D: Appl. Phys.* **28**, 1448 (1995).

[36] S. Uthanna, P. S. Reddy, B. S. naidu, and P. J. Reddy, *Vacuum* **4**, 91 (1996).

[37] J. Bregman and Y. Shapira, *J. Appl. Phys.* **67**, 3750 (1990).

[38] Y. Wu, C. H. M. Marèe, R. F. Haglund, Jr., J. D. Hamilton, M. A. Morales Paliza, M. b. Huang, L. C. Feldman, and R. A. Weller, *J. Appl. Phys.* **86**, 991 (1999).

[39] M. Buchanan, J. B. Webb, and D. F. Williams, *Appl. Phys. Lett.* **37**, 213 (1980).

[40] S. Ray, R. Bajerjee, N. Basu, A.K. Batabyal, and A. K. Barua, *J. Appl. Phys.* **54**, 3497 (1983).

[41] M. Clement, J. Santamaria, E. Iborra, and G. González-Diaz, *Vacuum* **37**, 447 (1987).

[42] M. Libra and L. Bárdoš, *Vacuum* **38**, 455 (1988).

[43] H. Nanto, T. Minami, S. Orito, and S. Takata, *J. Appl. Phys.* **63**, 2711 (1988).

[44] C. V. R. Vasant Kumar and A. Mansingh, *J. Appl. Phys.* **65**, 1270 (1989).

[45] H.-W. Zhang and W.-Y. Xu, *Vacuum* **43**, 835 (1992).

[46] H.-W. Zhang, Y.-G. Zhang, ans W.-Y. Xu, *Vacuum* **45**, 145 (1994).

[47] L.-J. Meng, A. Maçarico, and R. Martins, *Vacuum* **46**, 673 (1995).

[48] W.-F. Wu, B.-S. Chiou, ans S.-T. Hsieh, *Semicond. Sci. Technol.* **9**, 1242 (1994).

[49] W.-F. Wu and B.-S. Chiou, *Semicond. Sci. Technol.* **11**, 196 (1996).

[50] T. Gervin and M. Grätzel, *J. Appl. Phys.* **79**, 1722 (1996).

[51] R. B. H. Tahar, T. Ban, Y. Ohya, and Y. Takahashi, *J. Appl. Phys.* **83**, 2631 (1998).

[52] K. Zhang, F. Zhu, C. H. A. Huan and A. T. S. Wee, *J. Appl. Phys.* **86**, 974 (1999).

[53] S. M. Sze *Physics of Semiconductor Devices* (Wiley Interscience, New York, 1981).

[54] L. J. van der Pauw, *Philips Research Reports* **13**, 1 (1958).

Chapter 4

External Coupling of Light in OLEDs: Model Development

4.1 Introduction

The enormous research interest in OLEDs is due primarily to their application in flat panel displays. Hence, one critical figure of merit for OLEDs is the electroluminescence external efficiency, η_{EL}^{ext} (externally emitted photon/injected electron). A number of models for current–voltage behavior in OLEDs have been developed, all of which start from analyzing charge injection, then carrier transport, and finally the creation of excitons [1]-[3]. The present work starts from the point where the appropriate excitons have already been created, and attempt to answer the questions, "How do these excitons decay?" and "How much light is emitted externally from each exciton?" Our specific advances over previous work are: a) a combined classical and quantum mechanical microcavity (CCQMM) model [4]

is used to calculate the distribution of light emission into the external, substrate and ITO/organic waveguided modes as a function of the OLED structure; b) the energy transfer to the cathode is investigated with a classical Green's function formalism for several different cathode materials; and c) the model is applied to OLEDs on shaped, high-index-of-refraction substrates where the light in substrate waveguided modes are converted to external modes (experimental data in Chapter 5).

After a brief description of the light-trapping problem, the CCQMM model of OLEDs is derived in Sec. 4.2. While the CCQMM model was first developed by Bulović et al. [4], the analytical treatment of the external modes employed here is slightly different. Although many works have been published on the classical or the quantum mechanical treatment of radiating molecules in cavities, the combined theory has never been published before in this detail. The level of analytical rigor, relative to classical ray optics, is needed since the layers within a typical OLED is thinner than the wavelength of the light the OLED emits. The model is used to explore the dependency of the coupling efficiency on various aspects of device architecture, such as the distance between the emission zone to the cathode, the index of refraction of the substrate, and the thickness of the ITO layer. The expected increase in external emission due to shaped substrates is also calculated. Selected numerical results are presented in Sec. 4.3, while the experimental data and application of the model are left for the next chapter.

4.1.1 The light trapping problem – ray optics theory

A critical figure of merit for OLEDs is the external coupling efficiency, η_{cp}^{ext}, which links the external electroluminescence (EL) quantum efficiency (photon/electron), η_{EL}^{ext}, to the internal quantum efficiency (internally emitted photon/electron), η_{EL}^{int}, by the relation

$$\eta_{EL}^{ext} = \eta_{cp}^{ext} \eta_{EL}^{int}. \tag{4.1}$$

The typical OLED consists of a multi-layer sandwich of a planar glass substrate, a layer of ITO, one or more organic layers, and a reflective cathode. The emitted light suffers from total internal reflection (TIR) at the ITO/glass and glass/air interfaces. Thus it can be classified into three types of modes: the external modes where the light escapes the substrate, the substrate-waveguided modes, and the ITO/organic-waveguided modes (Figure 4.1) [5, 6].

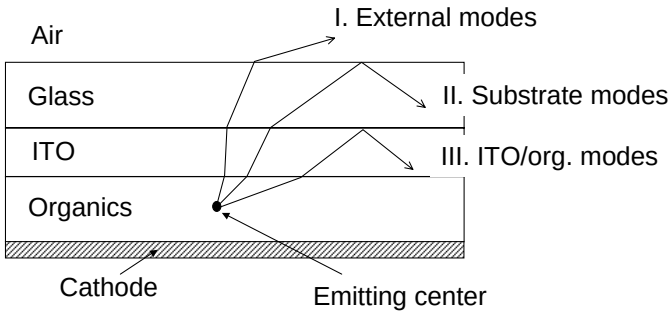

Figure 4.1: Three types of radiative modes in OLEDs: I. External modes, II. Substrate modes, and III. ITO/organic modes.

In ray optics, the emitting exciton is regarded as an isotropic source, and the

flux into each of the modes is obtained simply by integrating over the appropriate solid angles:

$$\eta_{cp}^{ext} = \int_0^{\theta_{c1}} \sin\theta_o d\theta_o = 1 - \cos\theta_{c1} \approx \frac{1}{2n_o^2} \tag{4.2}$$

$$\eta_{cp}^{sub} = \cos\theta_{c1} - \cos\theta_{c2} \tag{4.3}$$

$$\eta_{cp}^{IO} = \cos\theta_{c2} \tag{4.4}$$

where θ_o is the angle from normal in the emitting layer; $\theta_{c1} = \sin^{-1} n_a/n_o$ is the cut-off angle for external modes; $\theta_{c2} = \sin^{-1} n_g/n_o$ is the cut-off angle for substrate modes; $n_a, n_g,$ and n_o are the index of refraction of air, glass and the emitting layer, respectively. At $n_a = 1, n_g = 1.51,$ and $n_o = 1.71$, the coupling efficiencies of the external, substrate and ITO/organic modes are 18.9%, 34.2%, and 46.9%, respectively [5, 6]. This model neglects roughness in the layers which would scatter some modes into others. The RMS roughness of the ITO-coated glass substrates were measured by atomic force microscope (AFM) to be on the order of 2 nm, which is much less than the wavelength being considered here; however, features of 10's of nm in height are frequently encountered. Other scattering may be caused by uneven interdiffusion of materials during thermal evaporation which results in less well-defined layers.

Furthermore, the external luminous intensity distribution $I(\theta_{ff})$, where θ_{ff} is the viewing angle in the far-field in air, under the same assumptions, is given by [7],

$$I(\theta_{ff}) = I(\theta_o)\frac{n_a^2 \cos\theta_{ff}}{n_o^2 \cos\theta_o} \tag{4.5}$$

which approximately resembles the cosine intensity profile of a Lambertian emitter. θ_o and θ_{ff} are related through Snell's law, $n_o \sin\theta_o = n_a \sin\theta_{ff}$. $I(\theta_o)$ is the intensity distribution in the emitting layer denoted by the subscript "o", and is assumed to be isotropic in ray optics. In eq. 4.5, it is assumed that all light incident an interface at angles less than the critical angle are completely transmitted. One can also calculate the intensity profile using the Fresnel transmission coefficients for each angle, but the difference between the two is small [6]. Eq. 4.5 is generally applicable for finding the intensity distribution in the destination medium (in this case, air) from a known intensity distribution in the incident medium (in this case, the emitting organic material). There can exist any number of intervening layers as long as none of their refractive indices is not less than that of the destination medium.

4.1.2 Inadequacies of the ray optics model

Ray optics provides a qualitative understanding in the out coupling efficiency of various modes, but remains inadequate in view of the fact that the layer thicknesses in a typical OLED are shorter than the wavelength of the light it emits. According to spin statistics, the singlet:triplet ratio for excitons is 1:3, which has been verified in Alq_3 [9], so the upper limit of the internal EL efficiency, η_{int}^{EL} is 25%. By eqs. (4.1) and (4.4), the maximum external EL efficiency, η_{int}^{EL}, is around 5% [10]. However, Kido et al. fabricated highly efficient small molecule fluorescent OLEDs with an

external quantum efficiency in excess of 7% [11], casting doubt on the validity of the coupling efficiency as calculated by ray optics. In addition, several groups have reported dependence of the far-field emission pattern on the thickness of the organic layer, which is not explained by the ray optics theory [12, 13].

In the following section, the CCQMM theory for OLEDs is used to more precisely calculate the distribution of emission into the external, substrate and ITO/organic modes as well as to predict the amount of increase in the external efficiency due to shaped substrates.

4.2 The CCQMM model

4.2.1 Overview

The schematic diagram of the OLED structure used in both modeling and experiments is shown in Figure 4.2. The microcavity is confined on one side by the cathode and on the other, the leaky ITO/glass interface.

The behavior of radiating molecules in an optical microcavity is a general problem that can be approached in two ways: one based on classical electrodynamics and one based on quantum mechanics. Using a classical approach, many groups have examined the far-field emission characteristics as a function of the OLED layer structure using wave optics and a transfer matrix formalism [14]-[19]. Most recently, the electroluminescence pattern of polymer LEDs were found to

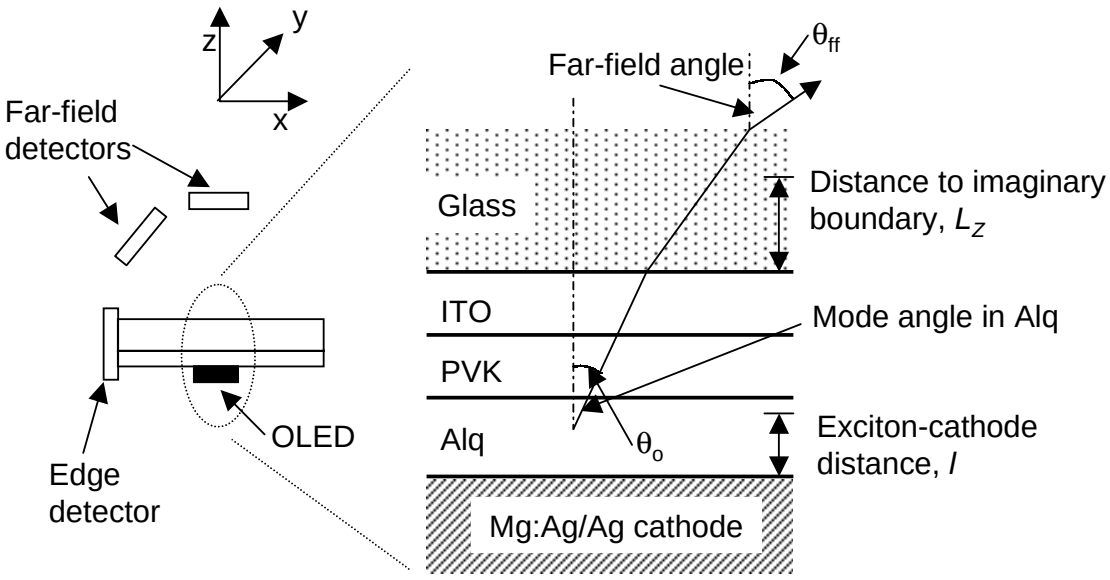

Figure 4.2: Schematic diagram of the OLED structure used in both modeling and experiments.

be accurately described by a half-space dipole model that accounts for optical interference effects due to the metal cathode [20]. The most complete classical treatment of the general problem is that presented by Chance, Prock, and Sibley [21], where the radiating molecule is modeled as a classical oscillating dipole and the radiation fields in the layered media is described by a dyadic Green's function. Some of their earlier work was based on a Hertzian vector approach that has recently been applied to OLEDs [22]-[24]. They have shown that the Green's function method is completely equivalent to the Hertzian vector approach and more easily applied to general stratified media [21]. A simpler version of this theory has been used to explain photoluminescence data from an Alq_3-Al system [25]. From a quantum mechanical point of view, Ujihara presented field quantization of a one-

dimensional optical cavity with output coupling in an early paper [26]. Similar quantum mechanical treatments were used to describe the change in rate, spectrum and directionality of emission from radiative dipoles in III-V semiconductor microcavities [27]-[29].

The CCQMM model was developed by Bulović et al. [4]. In the QM treatment, the electromagnetic field in the layered microcavity is represented by the sum of eigenmodes of the cavity; the radiating molecule is modeled as a dipole; and the transition probability into each mode is given by Fermi's golden rule. The QM approach has the advantage that the transition rates into the external, substrate and ITO/organic modes are computed separately. The shortcoming of the QM approach is that it does not account for the energy transfer from the dipole to the metal electrodes. However, it was shown by Chance et al. that this energy transfer arises exclusively from the near field of the dipole [21], so it does not affect the shape of the normalized far-field intensity pattern. In the model developed by Bulović et al., the QM microcavity treatment is augmented by the Green's function analysis, which is more convenient in computing the total rate of energy loss and hence the dipole lifetime in layered media [4]. In that work, the model was used to calculate the far-field emission spectrum as a function of the far-field angle, as well as the emission into the substrate-waveguided modes.

In this work, the CCQMM model is used to calculate the distribution of light emission into all three (external, substrate and ITO/organic) modes; thus the

entire decay mechanism of excitons can be calculated. The model is used to examine the dependence of this distribution on the thickness and material constants of the constituent layers. Numerical results are compared with measured intensity profiles and edge emission data. Furthermore, it has been shown that patterning on the backside of the OLED substrate can convert substrate-waveguided light into externally emitted light [6, 8, 30]. This model is applied to OLEDs on shaped substrates to calculate the amount of enhancement in external emission as a function of the index of the substrate. Finally, based on these calculations as well as the experimental data, general principles in device optimization are discussed.

4.2.2 Exciton recombination process

Both electroluminescence and photoluminescence (PL) are due to the radiative recombination of Frenkel excitons within the organic layers [31]. Since the quantum mechanical approach is based on the dipole approximation, and the classical analysis models the recombining excitons as oscillating dipoles, the terms "exciton" and "dipole" will be used interchangeably. A schematic diagram of the emission process is shown in Figure 4.3. Our discussion is based on the emitter/electron transport material, Alq_3, but can be easily extended to doped or electrophosphorescent devices. For example, the path occurring under "singlets" in Figure 4.3 could easily be applied to "triplets" as well.

For each electron injected into the device, a fraction of $\gamma\, r_{st}$ results in singlet

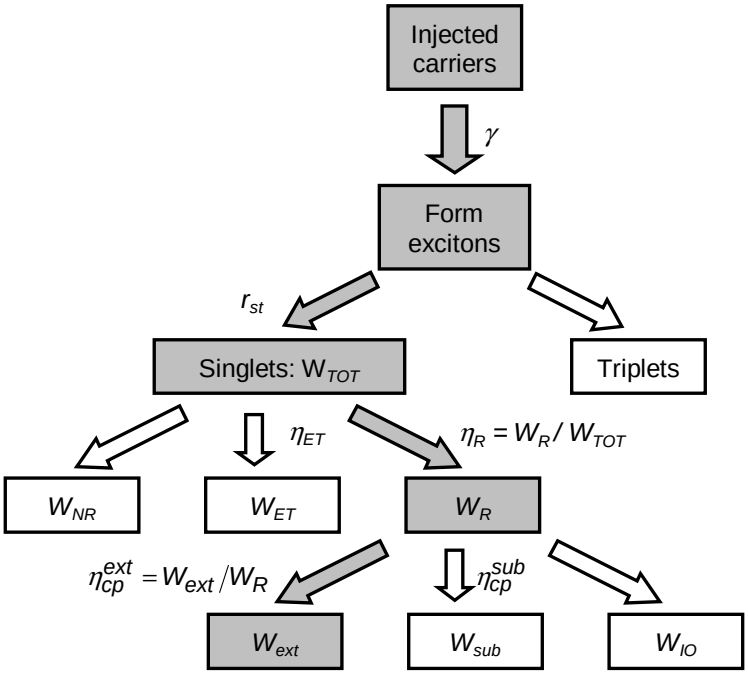

Figure 4.3: A schematic diagram of electrofluorescence in OLEDs: the gray path indicates the mechanism by which useful EL is emitted.

excitons, where γ is the number of exciton forming events per electron flowing through the OLED, and r_{st} is the fraction of singlet excitons thereof. The decay of the singlet excitons is described by the following equation:

$$\begin{aligned} W_{TOT} &= W_R + W_{ET} + W_{NR} \\ W_R &= W_{ext} + W_{sub} + W_{IO} \end{aligned} \tag{4.6}$$

where the W's are defined as $h\nu f$, where f denotes the transition rate per Fermi's golden rule (eq. 4.13), and have units of Watts. W_{TOT} is the total rate of decay of the singlet excitons. The rate of radiative decay, W_R, is the sum of the decay rates of the external, substrate and ITO/organic radiative modes, W_{ext}, W_{sub}, and W_{IO}. W_{ET} denotes the rate of energy transfer to the metallic cathode via non-radiative

dipole-metal transfer and excitation of surface plasmons. W_{NR} denotes the rate of non-radiative decay of the exciton which is assumed to be unaffected by the placement in the microcavity. Thus $W_{NR} = W^0_{NR}$, where W^0_{NR} is the intrinsic rate of non-radiative decay due to internal conversion and intersystem crossing which can be calculated from the photoluminescence quantum efficiency, η_{PL}, of a thick film [4]:

$$\eta_{PL} = W_0/(W_0 + W^0_{NR}) \tag{4.7}$$

where W_0 is the intrinsic rate of radiative decay. η_{PL} of Alq_3 has been accurately measured to be $32 \pm 2\%$, or $W^0_{NR} = 2.125W_0$ [32]. The fraction of internally generated photons that are emitted externally is given by the external coupling efficiency:

$$\eta^{ext}_{cp} = W_{ext}/W_R \tag{4.8}$$

which is commonly held to be $\sim 20\%$ by ray optics — a figure that will be revisited later. Also of great interest is the number of photons emitted externally for every singlet exciton created, $\eta_{exciton}$,

$$\eta_{exciton} = W_{ext}/W_{TOT} \tag{4.9}$$

which takes the non-radiative decay into account; consequently, it is a better measure of the external emission from the exciton in the microcavity than η^{ext}_{cp}. This can be seen more clearly if we let τ denote the total lifetime of the exciton: the amount of radiation each exciton emits into the external modes is then given by

$W_{ext}\tau \propto W_{ext}/W_{TOT} \equiv \eta_{exciton}$. Various efficiency measures are related to each other as follows (Figure 4.3):

$$\begin{aligned} \eta_{EL}^{ext} &= \eta_{cp}^{ext}\,\eta_{EL}^{int} = \gamma\, r_{st}\,\eta_{exciton} \\ \eta_{EL}^{int} &= \gamma\, r_{st}\eta_R \\ \eta_{exciton} &= \eta_R\,\eta_{cp}^{ext} \end{aligned} \tag{4.10}$$

The fraction of singlet excitons, r_{st}, in OLEDs has been a topic of interest especially since several recent reports suggested that the fraction may approach 50% in certain polymer OLEDs [20, 33, 34], rather than the statistical 25% measured in small molecule OLEDs [9]. A precise knowledge of $\eta_{exciton}$ as a function of exciton location and the cavity structure is a must for the accurate determination of r_{st}.

Backside substrate patterning has been shown to increase the external emission by converting some of the substrate modes into external modes [6, 8, 30]. This conversion can be accounted for by replacing W_{ext} with $(W_{ext} + \beta W_{sub})$ in eqs. 4.8 and 4.9, where β is the conversion efficiency.

In a guest-host system such as Alq_3 doped with Coumarin 6 (C6), singlet excitons formed on Alq_3 are transferred onto the highly efficient ($W_{NR}^{C6} \sim 0$) C6 dopant via the Förster mechanism [35]. We then have

$$\begin{aligned} W_{TOT}^{Alq} &= W_F + W_R^{Alq} + W_{ET}^{Alq} + W_{NR}^{Alq} \\ W_{ext} &= W_F \frac{W_{ext}^{C6}}{W_R^{C6} + W_{ET}^{C6}} + W_{ext}^{Alq} \end{aligned} \tag{4.11}$$

where the subscripts have their usual meaning, and W_F is the rate of Förster transfer from Alq_3 to C6. The reverse transfer from C6 to Alq_3 along with the

non-radiative decay in C6 has been neglected. If the rate of Förster transfer is much greater than the rate of other decay paths of the Alq_3 singlet exciton, then the efficiency can be much higher than the undoped device, viz.

$$\eta_{exciton} = W_{ext}^{C6}/(W_R^{C6} + W_{ET}^{C6}) \tag{4.12}$$

4.2.3 QM calculation for the radiative modes

The recombining exciton is modeled as a two-level system whose transition rate, f, is given by Fermi's golden rule:

$$f = \frac{2\pi}{\hbar^2} \sum_m |\langle m|\mu \cdot \mathbf{E}(\mathbf{k}, z)|n\rangle|^2 \delta(E_n - E_M - h\nu) \tag{4.13}$$

where μ is the dipole moment and $\mathbf{E}(\mathbf{k}, z)$ is the electrical field for mode $\mathbf{k}$ at the location of the dipole; E_m and E_n are the energies of the initial and final exciton states; and $h\nu$ is the energy of the photon emitted. The total transition rate is obtained by summing over all $\mathbf{k}$ and ν. In Refs. [4] and [27], the external modes are treated as travelling waves which are not normalizable, although a ratio of the electric fields at far-field and within the OLED cavity can still be obtained. The current treatment follows Ujihara and Deppe et al. [26, 29], where an imaginary upper boundary is placed a distance L_Z away from the ITO/glass interface (Figure 4.2). Then all the modes are solved for, and L_Z is let to tend to infinity. Analytically, letting L_Z tend to infinity reduces the expression of the allowable $\mathbf{k}$ vectors to $k_z = n\pi/L_z$, n an integer. The advantage is that all modes

become normalizable. To evaluate the transition rate, f, it remains to calculated the electric fields at the dipole $\mathbf{E}(\mathbf{k}, z)$.

The expression for the external and substrate modes have the same form within the OLED microcavity. The only difference lies in the transmission or total internal refraction at the substrate/air interface which is calculated by classical ray optics (cf. eq. 4.5) [5, 6, 20]. The classical theory is applicable since the thickness of the substrate is much larger than the wavelength of the light emitted. The electrical fields are of the general form:

$$\begin{aligned} \mathbf{E}_{\mathbf{k}}^{TE} &= \mathbf{A}(\mathbf{k}) \sin^2(k_{oz} l)\hat{x} \\ \mathbf{E}_{\mathbf{k}}^{TM} &= \mathbf{B}(\mathbf{k}) \cos^2\theta_o \sin^2(k_{oz} l)\hat{y} + \mathbf{C}(\mathbf{k}) \sin^2\theta_o \cos^2(k_{oz} l)\hat{z} \end{aligned} \tag{4.14}$$

where $\mathbf{A}(\mathbf{k}), \mathbf{B}(\mathbf{k})$ and $\mathbf{C}(\mathbf{k})$ are functions of material constants and $\mathbf{k}$; k_{oz} is the z component of the wave vector in the emitting layer; l is the dipole-cathode distance; and θ_o is the angle of the mode in the emitting layer. Near an antinode in the electric field where the $\sin^2(k_{oz} l)$ terms are maximized, the TE and first half of the TM radiation, both of which arise from the in-plane component of the electric field, are maximized. Near a node in the electric field, the second half of the TM radiation, which arises from the normal component of the electric field, is maximized, leading to a large in-plane TM component. Hence, these two components in the TM radiation are called the antinodal and nodal contribution, respectively.

The following derivation is based on TE polarized waves — the derivation

for TM polarized waves presenting no extra difficulties. The cathode is assumed to be a perfect metal for simplicity. The electromagnetic wave of mode $\mathbf{k}$ polarized in the $\mathbf{x}$ direction is assumed to take the form

$$E^{TE}_{\mathbf{k}x} = \begin{cases} E^{TE}_{\mathbf{k}x} \sin k_{oz}(z + d_o + d_p + d_i)e^{ik_y y} & -(d_o + d_p + d_i) < z < -(d_p + d_i) \\ E^{TE}_{\mathbf{k}x}[A \sin k_{pz}(z + d_p + d_i) & \\ \quad + B \cos k_{pz}(z + d_p + d_i)]e^{ik_y y} & -(d_p + d_i) < z < -d_i \\ E^{TE}_{\mathbf{k}x}(C \sin k_{iz} z + D \cos k_{iz} z)e^{ik_y y} & -d_i < z < 0 \\ E^{TE}_{\mathbf{k}x} F \sin k_{gz}(z - L_z)e^{ik_y y} & 0 < z < L_z \end{cases} \tag{4.15}$$

where d_α, $\alpha = i, p, o$, are the thicknesses of the ITO, PVK and Alq_3, respectively. $k_{\beta z}$, $\beta = g, i, p, o$ are the z components of the $\mathbf{k}$ vector in glass, ITO, PVK and Alq_3, respectively. A – D and F, not to be confused with $\mathbf{A}(\mathbf{k}), \mathbf{B}(\mathbf{k})$ and $\mathbf{C}(\mathbf{k})$ of eq. 4.14, are coefficients to be determined. The magnetic field of the same plane wave can be found simply by

$$H^{TE}_{\mathbf{k}y} = -\frac{1}{\omega \mu_0} \partial_z E^{TE}_{\mathbf{k}x} \tag{4.16}$$

$$H^{TE}_{\mathbf{k}y} = \begin{cases} -\frac{1}{\omega\mu_0} E^{TE}_{\mathbf{k}x} \cos k_{oz}(z + d_o + d_p + d_i)e^{ik_y y} & -(d_o + d_p + d_i) < z < -(d_p + d_i) \\ -\frac{1}{\omega\mu_0} E^{TE}_{\mathbf{k}x}[A \cos k_{pz}(z + d_p + d_i) & \\ \quad - B \sin k_{pz}(z + d_p + d_i)]e^{ik_y y} & -(d_p + d_i) < z < -d_i \\ -\frac{1}{\omega\mu_0} E^{TE}_{\mathbf{k}x}(C \cos k_{iz} z - D \sin k_{iz} z)e^{ik_y y} & -d_i < z < 0 \\ -\frac{1}{\omega\mu_0} E^{TE}_{\mathbf{k}x} F \cos k_{gz}(z - L_z)e^{ik_y y} & 0 < z < L_z \end{cases} \tag{4.17}$$

where $\mu_0 = 1$ is the magnetic permeability. By the continuity of $E^{TE}_{\mathbf{k}x}$ and $H^{TE}_{\mathbf{k}y}$ at $z = -(d_p + d_i), -d_i$ and 0, the coefficients A – D and F can be determined. For spontaneous emission, which is relevant here, the magnitude of the mode is to be normalized by requiring the total energy in the mode to be equal to that of a photon. Due to the structure of the OLED microcavity, which ends in the glass substrate (Figure 4.2), the normalization condition amounts to

$$\hbar\omega = \oint_{\text{In glass}} \frac{1}{2}\epsilon_g |\mathbf{E}|^2 \, dv \tag{4.18}$$

$$E^{TE}_{\mathbf{k}x} = \frac{4\hbar\omega}{L_x L_y L_z \epsilon_g [(C\frac{k_{iz}}{k_{gz}})^2 + D^2]} \tag{4.19}$$

Here L_x and L_y represents the lateral dimension of the OLED, while L_Z is the distance between the ITO/glass interface and the imaginary boundary (Figure 4.2). Substituting eq. 4.19 into eq. 4.13, and replace the sum by an integral: $\sum_{\mathbf{k}} \Rightarrow \int (\text{mode volume in } \mathbf{k} \text{ space})^{-1} d^3\,\mathbf{k}$, the L's cancel themselves out and the decay rates into external and substrate TE modes are found to be:

$$W^{TE}_{ext}(\lambda) = W_{PL}(\lambda)\frac{\epsilon_o}{\epsilon_g}\int_0^{\theta_{c1}} [(C\frac{k_{iz}}{k_{gz}})^2 + D^2]^{-1} \sin^2 k_{oz} l \sin\theta \; d\theta \tag{4.20}$$

$$W^{TE}_{sub}(\lambda) = W_{PL}(\lambda)\frac{\epsilon_o}{\epsilon_g}\int_{\theta_{c1}}^{\theta_{c2}} [(C\frac{k_{iz}}{k_{gz}})^2 + D^2]^{-1} \sin^2 k_{oz} l \sin\theta \; d\theta \tag{4.21}$$

where $W_{PL}(\lambda)$ is the normalized PL power spectrum measured in a thick film ($\int W_{PL}(\lambda) d\lambda = 1$). It is often convenient to express various decay rates in relation

to the intrinsic rate, W_0:

$$\begin{aligned} f_0 &= \frac{2\pi}{c\hbar^2}\sum_{\mathbf{k}} |\mathbf{E}_{\mathbf{k}}\cdot\mu|^2\,\delta(\frac{\omega}{c}-k) \\ &= \frac{2\pi}{\hbar^2 c}\int k^2 d\,k E^2\mu^2\,\delta(\frac{\omega}{c}-k)\frac{L_xL_yL_z}{\pi^3}\,(2\pi\int_0^{\pi}\cos\theta\sin\theta d\,\theta) \\ &= \frac{64\mu^2\omega^3}{3\hbar c^3\epsilon_o} \\ W_o(\lambda) &= f_o\hbar\omega W_{PL}(\lambda) \end{aligned} \tag{4.22}$$

The intensity of radiation from an exciton at a single point in space and at a single wavelength within the Alq_3 layer, $I_{single}(\theta_o,\lambda,l)$, is given simply by

$$I_{single}(\theta_o,\lambda,l) = W_{PL}(\lambda)\frac{\epsilon_o}{\epsilon_g}[(C\frac{k_{iz}}{k_{gz}})^2+D^2]^{-1}\sin^2 k_{oz}l\sin\theta \tag{4.23}$$

The decay rates into the ITO/organic modes are substantially similar to the derivation above, the one difference being that the sum in $\mathbf{k}_z$ is now discrete due to the fact that the relevant layer thicknesses are on the order of the wavelength of visible light. The integral in $\mathbf{k}_x$ and $\mathbf{k}_y$ remains the same, viz. $\sum_{\mathbf{k}} \Rightarrow \sum_{k_z}\int(\text{mode area in } \mathbf{k}_{xy}\text{ plane})^{-1}dk_xdk_y\,\delta(\sqrt{(\frac{\omega_o}{cn_o})^2-k_z^2}-k)$. Again the derivation given below is for the TE modes. The z-component of the mode vector $\mathbf{k}$ satisfies the transcendental equation:

$$-\frac{\tan k_{iz}d_i}{k_{iz}} = \frac{\frac{k_{oz}}{k_{pz}}\cos k_{oz}d_a\sin k_{pz}d_p+\sin k_{oz}d_o\cos k_{pz}d_p}{k_{oz}\cos k_{oz}d_o\cos k_{pz}d_p-k_{pz}\sin k_{oz}d_o\sin k_{pz}d_p} \tag{4.24}$$

which is to be solved numerically. After some manipulations, the rate of decay into the TE ITO/organic modes is found to be:

$$W_{IO}^{TE}(\lambda) = W_{PL}(\lambda)\frac{\lambda}{2d_o}\frac{4\hbar\omega}{L_xL_y}\sum_{kz}|E_{\mathbf{k}x}^{TE}|^2\sin^2 k_{oz}l\sin\theta \tag{4.25}$$

where the electrical field in the cavity $E_{\mathbf{k}x}^{TE}$ is normalized in the same way as in eq. 4.19 over the ITO/organic layer,

$$\oint_{\text{In ITO/organic}} \frac{1}{2}\epsilon|\mathbf{E}|^2 \, dv = \hbar\omega \tag{4.26}$$

The excitons are assumed to be generated at the Alq_3/PVK interface and then diffuse into the Alq_3 layer. Tang and co-workers found the exciton diffusion length to be 20 nm, from examining the EL of an Alq_3 based device with varying dye-doped regions [37]. Throughout this work, the exciton recombination profile is assumed to be the same as the diffusion profile with the same characteristic decay length ($L_D = 20$ nm). To calculate the intensity as a function of the mode angle in Alq_3, $I(\theta_o)$, $I_{single}(\theta_o, \lambda, l)$ is weighted by the PL spectrum of Alq_3 and the exciton recombination profile:

$$I(\theta_o) = \frac{\int\int I_{single}(\theta_o, \lambda, l) W_{PL}(\lambda) e^{-(do-l)/L_D} d\lambda \, dl}{\int e^{-(do-l)/L_D} dl} \tag{4.27}$$

where $W_{PL}(\lambda)$ is the normalized Alq_3 PL spectrum, l is the dipole-cathode distance, and do is the thickness of the Alq_3 layer.

Finally, the normalized decay rates into the external, substrate and ITO/organic modes, weighted by the exciton profile and the emission spectrum, are

$$\begin{aligned}
\frac{W_{ext}}{W_0} &= \frac{\int\int (W_{ext}^{TE}(\lambda) + W_{ext}^{TM}(\lambda)) e^{-(do-l)/L_D} d\lambda \, dl}{\int e^{-(do-l)/L_D} dl} \\
\frac{W_{sub}}{W_0} &= \frac{\int\int (W_{sub}^{TE}(\lambda) + W_{sub}^{TM}(\lambda)) e^{-(do-l)/L_D} d\lambda \, dl}{\int e^{-(do-l)/L_D} dl} \\
\frac{W_{IO}}{W_0} &= \frac{\int\int (W_{IO}^{TE}(\lambda) + W_{IO}^{TM}(\lambda)) e^{-(do-l)/L_D} d\lambda \, dl}{\int e^{-(do-l)/L_D} dl}
\end{aligned} \tag{4.28}$$

4.2.4 Classical calculation for the dipole-cathode energy transfer

Introduction

The Fermi's golden rule used in the QM calculation of exciton recombination is based on the dipole approximation; therefore, its results are valid only for the far-field. In the absence of the microcavity, a dipole placed close to a metal surface undergoes an energy transfer to the metal in the form of $W_{ET} \propto l^{-3}$ in the limit of short dipole-cathode separation $l \ll \lambda$ [21]-[23]. Although the effect of the cathode is expected to remain preeminent for a dipole in the OLED weak microcavity, the other dielectric interfaces also affect the field distribution in the microcavity; therefore, a more complete analysis is required for an exact solution. The Green's function analysis is a powerful method for solving for the electromagnetic (EM) fields in layered media. It can be used to calculated the normalized decay rate due to the total EM fields of the dipole, $(W_R + W_{ET})/W_0$. Combined with the knowledge of the non-radiative decay learned from PL measurements (e.g., $W_{NR} \approx W_{NR}^0 = 2.125W_0$ in Alq_3 [32]), the normalized total rate of decay W_{TOT}/W_0 can be obtained.

This section contains derivations of the Green's function method and calculated $(W_R+W_{ET})/W_0$ for several different cathode materials, as well as normalized exciton lifetime as a function of the exciton location.

Decay rates calculated by the Green's function method

The derivations below is adapted to the actual OLEDs fabricated (Figure 4.2) but still follows closely that of Tai [38] and Chance et al. [21].

The Green's function for the OLED microcavity is constructed as follows:

$$\begin{aligned}\mathbf{G}_\alpha &= \frac{i}{4\pi}\int_0^\infty d\lambda \sum_{n=0,j=e,o}^{\infty} \frac{2-\delta_{no}}{\lambda h_o}\{[C_\alpha \mathbf{M}_{jn\lambda}(-h_\alpha) + C'_\alpha \mathbf{M}_{jn\lambda}(h_\alpha)]\mathbf{M}'_{jn\lambda} \\ &\quad +[F_\alpha \mathbf{N}_{jn\lambda}(-h_\alpha) + F'_\alpha \mathbf{N}_{jn\lambda}(h_\alpha)]\mathbf{N}'_{jn\lambda}(h_\alpha)\} + \delta_{\alpha o}\mathbf{G}^0_o \end{aligned} \tag{4.29}$$

where $h_\alpha = \sqrt{k_\alpha^2 - \lambda^2}$. The subscript, $\alpha = g, i, p,$ and o, denotes the glass, ITO, PVK, and Alq_3 layers respectively. The second term in the equation, $\mathbf{G}^0_o$, represents the source function in the organic layer:

$$\begin{aligned}\mathbf{G}^0_o &= \frac{i}{4\pi}\int_0^\infty d\lambda \sum_{n=0,\ j=e,o}^{\infty} \\ &\quad \frac{2-\delta_{no}}{\lambda h_o}\begin{bmatrix} \mathbf{M}_{jn\lambda}(h_o)\mathbf{M}_{jn\lambda}(-h_o)' + \mathbf{N}_{jn\lambda}(h_o)\mathbf{N}_{jn\lambda}(-h_o)' & z \geq z' \\ \mathbf{M}_{jn\lambda}(-h_o)\mathbf{M}_{jn\lambda}(h_o)' + \mathbf{N}_{jn\lambda}(-h_o)\mathbf{N}_{jn\lambda}(h_o)' & z \leq z' \end{bmatrix}\end{aligned} \tag{4.30}$$

The dipole is located at $z = z'$ in the Alq_3 layer. The functions $\mathbf{M}_{jn\lambda}$ and $\mathbf{N}_{jn\lambda}$ are the eigenfunctions in cylindrical coordinates [38]:

$$\begin{aligned}\mathbf{M}_{\substack{e\\o}n\lambda}(h) &= [\mp\frac{nJ_n(\lambda r)}{r}\begin{matrix}\sin\\\cos\end{matrix} n\phi\ \hat{r} - \frac{\partial J_n(\lambda r)}{\partial r}\begin{matrix}\cos\\\sin\end{matrix} n\phi\ \hat{\phi}]\, e^{ihz} \\ \mathbf{N}_{\substack{e\\o}n\lambda}(h) &= \frac{1}{k_\lambda}[ih\frac{\partial J_n(\lambda r)}{\partial r}\begin{matrix}\cos\\\sin\end{matrix} n\phi\ \hat{r} \\ &\quad \pm\frac{ihn}{r}J_n(\lambda r)\begin{matrix}\sin\\\cos\end{matrix} n\phi\ \hat{\phi} + \lambda^2 J_n(\lambda r)\begin{matrix}\cos\\\sin\end{matrix} n\phi\ \hat{z}]\, e^{ihz}\end{aligned} \tag{4.31}$$

Although the expressions seem daunting, they simplify nicely at the point of the dipole which we set to be the origin of the cylindrical coordinate system. The

usual boundary conditions of the electromagnetic fields are elegantly conveyed by the continuity of $\hat{z} \times \mathbf{G}$ and $\hat{z} \times \Delta \times \mathbf{G}$ at the interfaces. The system of linear equations arising from the boundary conditions can be solved for the coefficients, $C_\alpha, C'_\alpha, F_\alpha$ and F'_α in eq. 4.29, after which the normalized rate of decay can be found via

$$\hat{W}_\perp = 1 + \frac{3}{2} \operatorname{Re} \int_0^\infty \frac{\lambda^3 F'_o}{h_o k_o^3} e^{i2h_o l} \, d\lambda \tag{4.32}$$

$$\hat{W}_\parallel = 1 + \frac{3}{4} \operatorname{Re} \int_o^\infty (C'_o - \frac{h_o^2}{k_o^2} F'_o) \frac{\lambda}{h_o k_o} e^{i2h_o l} \, d\lambda \tag{4.33}$$

where $\hat{W}_\perp$ and $\hat{W}_\parallel$ are the normalized rates for dipoles perpendicular and parallel to the metal surface, respectively. l is the dipole-cathode distance. For a collection of dipoles having no preferred average orientation (isotropic dipole), the decay rate is given by

$$\frac{W_{ISO}}{W_0} = 1/3\hat{W}_\perp + 2/3\hat{W}_\parallel \tag{4.34}$$

Note that in evaporated Alq_3 films, the molecular orientation is random, thus the ensemble average is isotropic, i.e., $W_R + W_{ET} = W_{ISO}$. In polymer OLEDs, a preferred dipole orientation may exist due to spin-coating of the polymer layer [20, 41, 42].

Calculated energy transfer rates and exciton lifetimes

Figure 4.4 illustrates the calculated decay rate as a function of dipole-cathode distance for a monochromatic emitter at 524 nm, placed in a microcavity consisting of cathode/organic layer/ITO/glass, where the cathode material is Ag, Al or Mg.

At a short distance away, the interaction between the near-field of the dipole and the metal leads to a high W_{ET}, i.e. cathode quenching, resulting in a very short lifetime. The rate of energy transfer is twice as fast for a perpendicular dipole as for a parallel dipole, the physics of which is similar to the radiation of dipole antennas immediately above the earth's surface [39]. The same principle was used to determine the orientation of single molecules at an interface by their fluorescence lifetimes [40].

The energy transfer to the metal cathode can be thought of as damping of the electric field in the cathode. Therefore, aluminum, with the highest reflectivity among the three materials, gives rise to the least W_{ET}; conversely, magnesium gives rise to the largest (Figure 4.4). For all three cathodes, W_{ET} is drastically reduced for dipole-cathode distance above 60-80 nm. $(W_R + W_{ET})/W_0$ approaches 1.3 - 1.5 for a dipole-cathode distance of 80 - 140 nm. The dipole-cathode energy transfer is *not* negligible in this region since the dipole-cathode distance is still less than the wavelength, but it no longer dominates the total decay rate. The sum of W_R and W_{ET} and their relative contribution depend sensitively on the exact microcavity structure.

The normalized lifetime, $\tau/\tau_0 = W_0/W_{TOT}$, is plotted in Figure 4.5 as a function of the dipole-cathode distance and the dipole orientation for a typical Alq_3-based OLED fabricated in this work. $\tau_o \propto 1/(W_0 + W_{NR}^0)$ is the intrinsic Alq_3 lifetime in a thick film. This differs from the previous plot in that W_{NR} is also

taken into account (see Sec. 4.2.5). Here W_{ET} decreases rapidly with increasing dipole-cathode distance and the lifetime levels off to approximately 85% of the intrinsic lifetime at a dipole-cathode separation of 80 nm (cf. Ref. [4]).

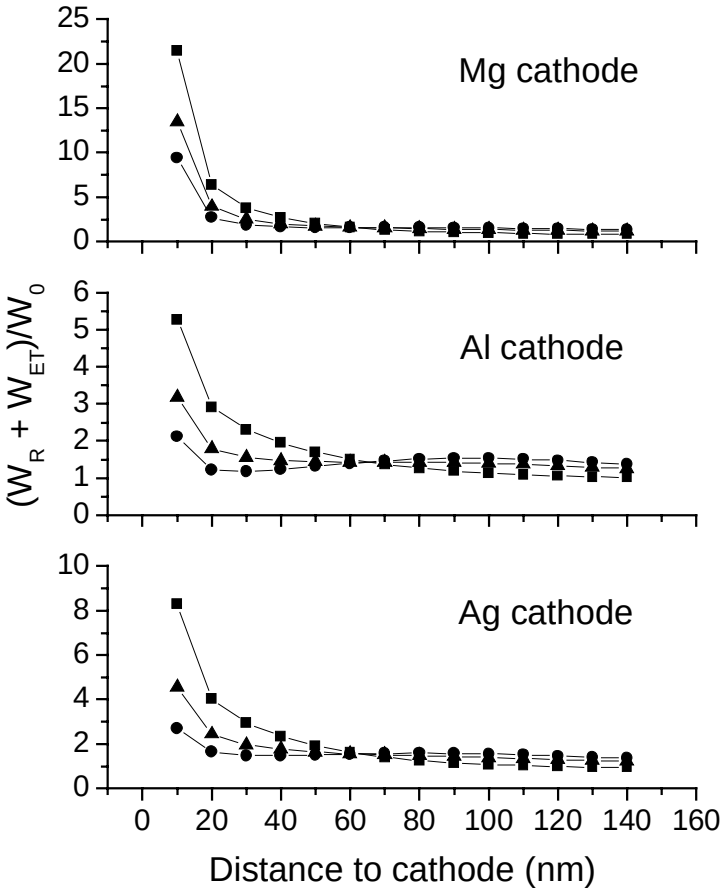

Figure 4.4: Normalized decay rate due to the total electromagnetic fields of the dipole $(W_R + W_{ET})/W_0$ as a function of the dipole-cathode distance for three different cathode materials. Squares: perpendicular dipole, circles: parallel dipole, triangle: isotropic dipole. The OLED cavity has the structure: cathode/organics (n = 1.7, t = 150 nm)/ITO (n = 1.8, t = 120 nm)/glass (n=1.51). Calculated for a monochromatic emitter at 524 nm.

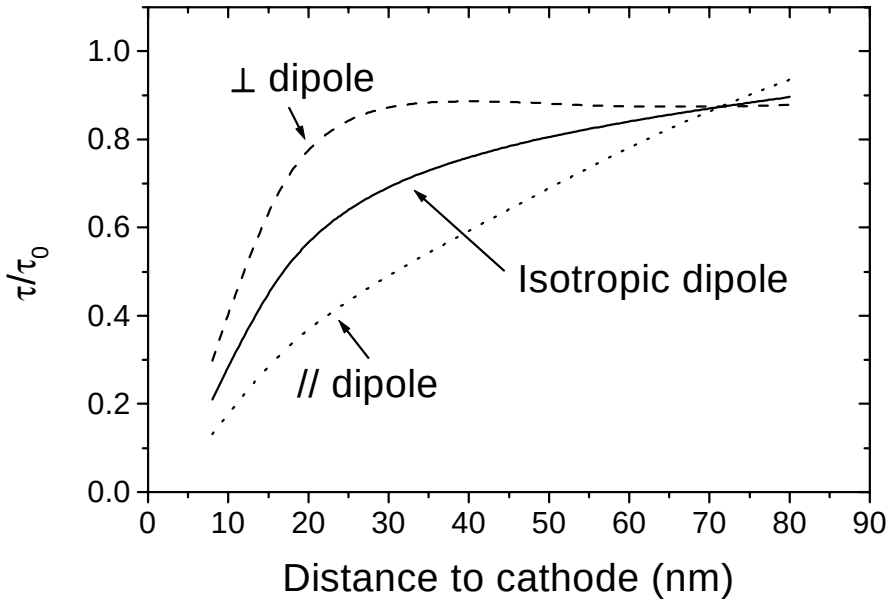

Figure 4.5: Normalized lifetime *vs.* exciton distance to cathode in the OLED (soda lime glass/100 nm ITO/40 nm PVK/80nm Alq_3/Ag).

4.2.5 Combining the quantum mechanical and classical results

To calculate the rate of singlet excitons that radiates into the various modes (external, substrate and ITO/organic), we need to know the rate of singlet excitons that are lost due to non-radiative decay (W_{NR}) and energy transfer to the cathode (W_{ET}). However, the rate of energy transfer to the cathode cannot be evaluated directly, but only through the sum $W_R + W_{ET}$. This problem is solved by combining the QM and classical results.

The calculated decay rates and intensities are all normalized to the intrinsic rate (eq. 4.22). Since $\tau \propto 1/W_{TOT}$, the amount of external emission of a singlet Alq_3 exciton is,

$$\frac{W_{ext}}{W_{TOT}} = \eta_{exciton} = \frac{W_{ext}}{W_0}\left(\frac{W_R + W_{ET}}{W_0} + \frac{W_{NR}}{W_0}\right)^{-1} \tag{4.35}$$

where W_{ext}/W_0 is calculated by quantum mechanics as shown in Sec. 4.2.3, $(W_R + W_{ET})/W_0$ by the Green's function method as shown in Sec. 4.2.4, and $W_{NR}/W_0 \simeq W^0_{NR}/W_0$ from the PL measurements.

4.3 Selected numerical results

4.3.1 Introduction

The intensity profile within the Alq_3 layer as calculated by classical ray optics theory, a half-space dipole model that was recently applied to polymer OLEDs [20], and the CCQMM model are plotted below to illustrate the difference between these models. Monochromatic emission at $\lambda = 524$ nm (peak wavelength of Alq_3 EL) from an emitter at the PVK/Alq_3 interface is considered. The mode intensity is plotted against the mode angle in Alq_3 in radial plots.

4.3.2 Classical ray optics

Figure 4.6 depicts classical ray optics picture where the radiation is isotropic. The cathode is assumed to be a perfect reflector so that radiation is into the forward direction. The wavelength is not a factor in this model. The TE and TM polarizations are identical, and the modes are delineated by the critical angles for TIR at the glass/air and ITO/glass interfaces. The total emitted flux is given by

$$F = 2\pi \int I(\theta_o) \sin\theta_o \, d\theta_o \tag{4.36}$$

for an angular intensity pattern, $I(\theta_o)$. The emission at large angles to normal is heavily weighted because of the large solid angles corresponding to large θ_o, so much so that 47% of the emitted light is in the ITO/organic mode according to the

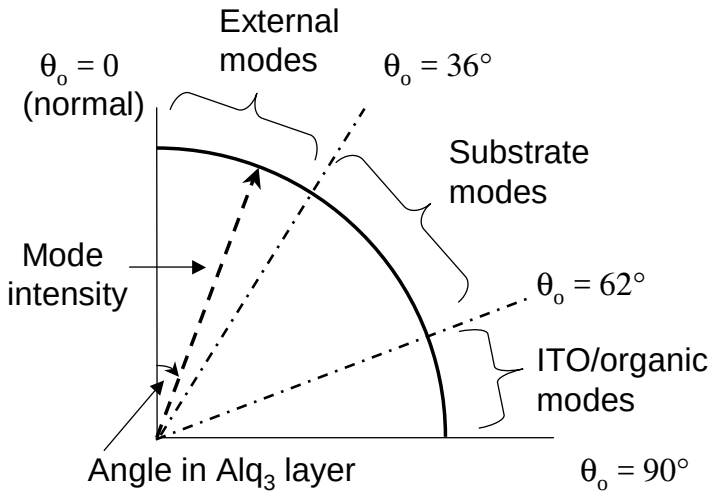

Figure 4.6: Radial plots of mode intensity *vs.* mode angle in Alq_3: classical ray optics.

ray optics theory. In reality, the cut-off wavelength of the thin ITO/organic waveguiding slab may fall within the visible region, and the strength of the ITO/organic modes are in general less than what the classical theory leads one to believe.

4.3.3 Half-space dipole model

A recent paper on modeling the light emission in polymer OLEDs utilized a half-space dipole model, where the exciton in the OLED is approximated by a dipole located in a semi-infinite region of organic material on top of a semi-infinite metal cathode [20]. The far-field intensity is calculated from the superposition of the direct radiation and the reflection from the metal surface. This model does not take energy transfer to the metal due to the near-field of the dipole into account.

The far-field intensity is given by

$$I(\theta_o) \propto |1 + r_s \exp(i2\delta \cos\theta_o)|^2 + |1 - r_p \exp(i2\delta \cos\theta_o)|^2 \qquad (4.37)$$

where $\delta = 2\pi n_{org} l/\lambda$ is the phase distance from the cathode; r_s and r_p are the Fresnel reflection coefficients for TE and TM waves, respectively. For simplicity, the metal is assumed to be a perfect reflector. The intensity in the normal direction, $I(\theta_o = 0)$, is proportional to the square of the magnitude of the electric field which has maxima at $\delta = (m + 1/2)\pi$ or $l = (m/2 + 1/4)\lambda/n_{org}$. m is an integer. Figure 4.7 shows the same radial plot as in Figure 4.6 calculated by the half-space-dipole model for dipole-cathode distance of 20 and 80 nm [20]. Given the peak Alq_3 EL at 524 nm, the first maximum of emission intensity is a dipole-cathode spacing of 77 nm (see Figure 4.8 and the next section for details). The perfect metallic cathode creates a node in the electric field, so that at a shorter dipole-cathode distance of 20 nm, the modal intensity is much reduced (Figure 4.7).

Comparing with the classical ray optics picture, the intensity of the large angle modes is suppressed by interference due to the metal cathode. Numerically, the half-space dipole model achieves the same effect as taking into account the cut-off due to the thin ITO/organic waveguide, but the simplicity of the model precludes many variations in the OLED structure being reflected in the calculated intensity profile.

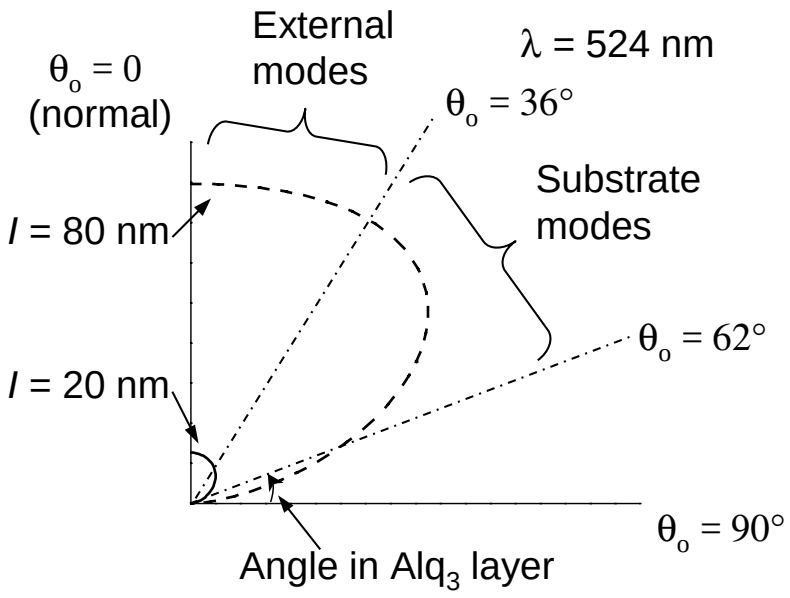

Figure 4.7: Radial plots of mode intensity *vs.* mode angle in Alq_3: half-space dipole model. Solid line: dipole-cathode distance = 20 nm, dashed line: dipole-cathode distance = 80 nm. The wavelength is 524 nm.

4.3.4 The CCQMM model

From eq. 4.13, the radiative decay rates, hence the intensity of each mode, is proportional to the square of the magnitude of the electric field, $\mathbf{E}(\mathbf{K})$, at the exciton. Here, $\mathbf{E}(\mathbf{k})$ is the electric field associated with the emitted light. $\mathbf{E}(\mathbf{k})$ has a strong dependence on the location of of the exciton within the OLED cavity. If the metal cathode is assumed to be a perfect metal for simplicity, the first antinode (maximum) of the electric field is located at $\lambda/4$ away from the cathode, i.e., $l \simeq 77$ nm for $\lambda = 524$ nm at the EL peak of Alq_3 (Figure 4.8). If the exciton is located near the antinode of the electric field, the total radiative emission is maximized; conversely, if the exciton is near the cathode where a node in the electric field

resides, the radiative emission is minimized. Note this decay in the light emission due to diminished **E** fields near the cathode is a separate effect from the increased dipole-cathode energy transfer which occurs in parallel for emitters located near the cathode. Indicated in the same figure, is the exciton recombination profile in a bilayer device with an 80-nm-thick Alq_3 layer, where the excitons are generated at the PVK/Alq_3 interface and diffuse into Alq_3.

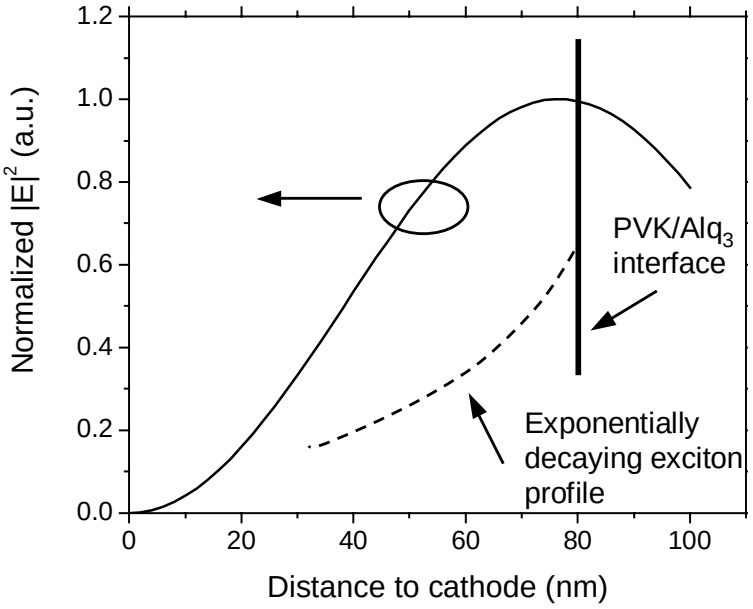

Figure 4.8: Normalized square of the magnitude of the electric field (proportional to the intensity of the mode) *vs.* distance to cathode in the organic layer. The wave vector is in the normal direction. Also indicated is the the approximate exciton profile in a bilayer device with an 80-nm-thick Alq_3 layer assuming a decay length of 20 nm. The OLED cavity has the structure: cathode (perfect metal)/organics (n = 1.7, t = 150 nm)/ITO (n = 1.8, t = 120 nm)/glass (n = 1.51). Calculated for a monochromatic emitter at 524 nm.

The CCQMM model is applied to two bilayer OLEDs with 20 or 80-nm-thick Alq_3 layers. The intensity profile in the organic layer from a single emitter at

the PVK/Alq_3 interface at the peak emission wavelength ($\lambda = 524$ nm) is plotted in Figure 4.9. In the device with an 80-nm-thick Alq_3 layer, the exciton is in close proximity to the antinode in the electric field at which point the TE and antinodal TM emissions are maximized (see eq. 4.14 and discussions thereafter). The radiation pattern retains much of the characteristics of that of an in-plane dipole again due to the fact that the electric field vector of both the TE and the antinodal TM waves are in the x-y plane. The external and substrate modes form a continuum, because mode density is inversely proportional to the thickness of the region of space where the modes occupy. In the device with a 20-nm-thick Alq_3 layer, the total radiation is much less, qualitatively similar to that calculated from a half-space dipole model (Figure 4.7). However, the TM radiation at large angles is enhanced as discussed. This is one clear distinction between the CCQMM model and the half-space dipole model. Measured far-field intensity patterns that supports the CCQMM model will be presented in the next chapter.

ITO/organic modes do not exist at 524 nm, which is above the cut-off wavelength of the ITO/organic waveguide. However, at shorter wavelengths, discrete modes do exist in the ITO/organic waveguide. A single TM mode in the ITO/organic waveguide exists in the device illustrated in Figure 4.10 at a wavelength of 380 nm. Rigorously, the mode should have been drawn as a δ-function in θ_o, the area under which corresponds to the energy in the mode. It is shown only as a single dot at the correct mode angle in the figure. Due to spatial confinement,

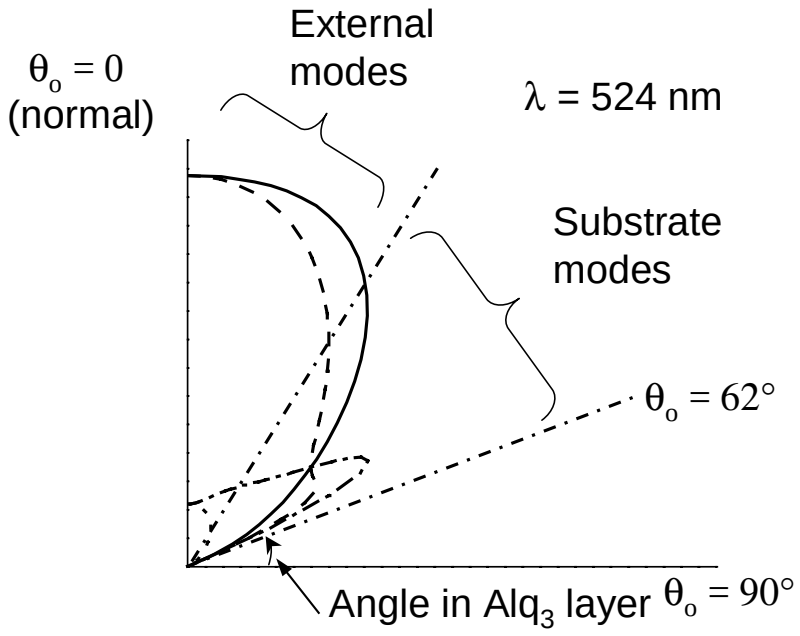

Figure 4.9: Radial plot of mode intensity *vs.* mode angle in Alq_3: CC-QMM model for two bilayer OLEDs with the structure: soda lime glass/100 nm ITO/40 nm PVK/Alq_3/cathode, solid line: 80 nm Alq_3, TE emission; dashed line: 80 nm Alq_3, TM; dotted line: 20 nm Alq_3, TE; dash-dotted line: 20 nm Alq_3, TE. The wavelength is 524 nm. The emitter is assumed to be at the Alq_3/PVK interface.

the energy in the discrete modes may still be significant.

4.3.5 Impact of high-index substrates

It will be shown in the next chapter that the use of shaped high-index substrates can recover almost all of the waveguided light for external emission. (The term "high-index" here refers specifically to indices higher than the that of the emitting layer ($n_{Alq} = 1.71$) . Some early work that led to this thesis involved polycarbonate substrates (n = 1.595) [6]. The increased in external coupling efficiency by using shaped substrates as a function of the refractive index of the substrate is

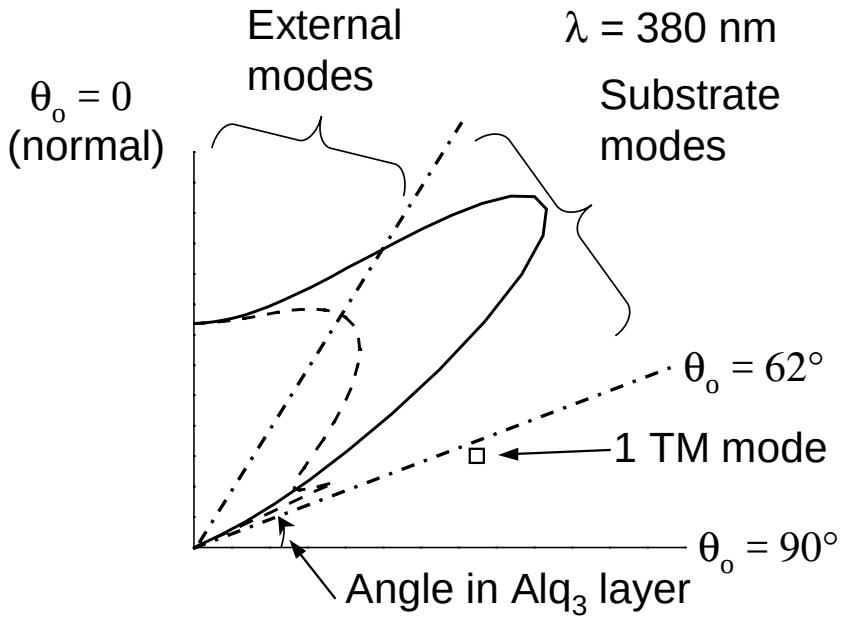

Figure 4.10: Radial plot of mode intensity *vs.* mode angle in Alq_3: CCQMM model for an OLED with the structure: soda lime glass/100 nm ITO/40 nm PVK/80 nm Alq_3/cathode, solid line: TE emission; dashed line: TM. The wavelength is 380 nm. The emitter is assumed to be at the Alq_3/PVK interface.

calculated by the CCQMM model in Chapter 5.) The radiation pattern of OLEDs on high-index substrates is examined here in keeping with the theme of this section. In an OLED on standard soda lime glass substrates, the ITO/organic modes are confined by TIR at the ITO/glass interface due to index mismatch between the substrate and the emitting layer ($n_{glass1} < n_{Alq}$). In OLEDs on high-index substrates ($n_{glass2} > n_{Alq}$), the ITO/organic modes are converted into substrate-waveguided modes which exist predominantly in the substrate. Figure 4.11 shows the radial plot of intensity *vs.* mode angle in the device as in Figure 4.9 except on a high-index substrate. The ITO/organic modes are no longer present, and all modes

form a continuum. The radiation pattern resembles that of an in-plane dipole up to large angles from the normal, where interference effects from the ITO/organic layer on the TM radiation are observed.

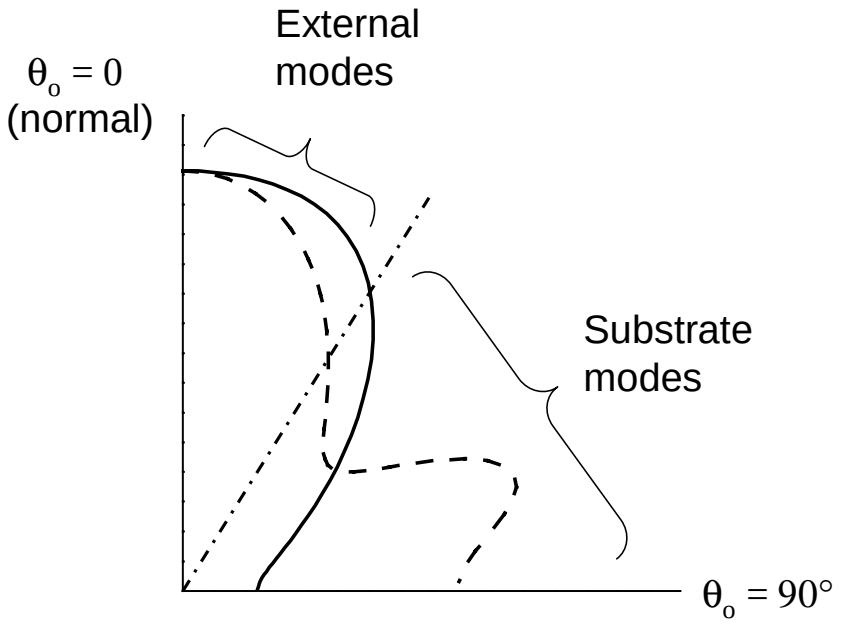

Figure 4.11: Radial plots of mode intensity *vs.* mode angle in Alq_3: CCQMM model for an OLED with the structure: high-index glass/100 nm ITO/40 nm PVK/80nm Alq_3/cathode, solid line: TE emission, dashed line: TM emission. The wavelength is 524 nm.

In the present construct of the CCQMM model, the microcavity ends in the glass substrate (Figure 4.2), although in reality, the external modes exist predominantly in air. This is prescribed by the relatively short coherent length of the emitted light when compared with the size of the total system. The EL from the OLED is inhomogeneously broadened — the energy levels depends on the surroundings of the excited molecule; therefore, it is difficult to deduce the coherent length from the EL spectrum. However, we can use the exciton lifetime as an estimate of the

coherence time. A typical fluorescence lifetime is 10^{-9} s, the non-radiative decay and dipole-cathode energy transfer can easily reduce the total lifetime by a factor of four, resulting in a coherence length less than 1 mm. The distance between the photo-detector and the OLED is typically 10 cm, which is much longer than the coherent length; hence, our microcavity does not include the substrate as one of its intermediate layers, and classical ray optics is used to describe the transmission of light from the substrate to air. The calculated decay rates are dependent upon the indices of the substrate material (Sec. 4.2.3). The CCQMM model calculates only relative intensities. The numerical results for devices on the same substrate can be compared with each other without reservation, but care must be taken in comparing the numerical results for devices on substrates of different indices. As shown in Chapter 5, when comparing the numerical results for OLEDs on both soda lime and high-index glass substrates, the measured external emission, W_{ext}, is used to normalize decay rates into other modes.

References

[1] G. G. Malliaras and J. C. Scott, *J. Appl. Phys.* **83**, 5399 (1998).

[2] P. S. Davids, I. H. Campbell, and D. L. Smith, "Device model for single carrier organic diodes", *J. Appl. Phys.* **82**, 6319 (1997).

[3] D. V. Khramtchenkov, V. I. Arkhipov, and H. Bässler, *J. Appl. Phys.* **81**, 6954 (1997).

[4] V. Bulović, V. B. Khalfin, G. Gu, P. E. Burrows, D. Z. Garbuzov, and S. R. Forrest, *Phys. Rev. B* **58**, 3730 (1998).

[5] N. C. Greenham, R. H. Friend, and D. D. C. Bradley, *Adv. Mater.* **6**, 491 (1994).

[6] C. F. Madigan, M.-H. Lu, and J. C. Sturm, *Appl. Phys. Lett.* **76**, 1650 (2000).

[7] G. Gu, D. Z. Garbuzov, P. E. Burrows, S. Venkatesh, and S. R. Forrest, *Opt. Lett.* **22**, 396 (1997).

[8] T. Yamasaki, K. Sumioka, and T. Tsutsui, *Appl. Phys. Lett.* **76**, 1243 (2000).

[9] M. A. Baldo, D. F. O'Brien, M. E. Thompson, and S. R. Forrest, *Phys. Rev. B* **60**, 14422 (1999).

[10] T. Tsutsui, Mater. Res. Bull. **22**, 39 (1997).

[11] J. Kido and Y. Iizumi, *Appl. Phys. Lett.* **73**, 2721 (1998).

[12] T. Tsutsui, M.-J. Yang, M. Yahiro, K. Nakamura, T. Wantanabe, T. Tsuji, Y. Fukuda. T. Wakimoto, and S. Miyaguchi, *Jph. J. Appl. Phys.* **38** L1502 (1999).

[13] M.-H. Lu, C. F. Madigan, and J. C. Sturm, *Mat. Res. Soc. Symp. Proc.* **621**, Q3.7 (2000).

[14] S. Saito, T. Tsutsui, M. Era, N. Takada, C. Adachi, Y. Hamada, and T. Wakimoto, *SPIE Proc.* **1910**, 212 (1993).

[15] J. Grüner, F. Cacialli, and R. H. Friend, *J. Appl. Phys.* **80**, 207 (1996).

[16] H. F. Wittmann, J. Grüner, R. H. Friend, G. W. C. Spencer, S. C. Moratti, and A. B. Holmes, *Adv. Mater.* **7**, 541 (1995).

[17] D. G. Lidzey, M. A. Pate, D. M. Whittaker, D. D. C. Bradley, M. S. Weaver, T. A. Fisher, and M. S. Skolnick, *Chem. Phys. Lett.* **263**, 655 (1996).

[18] V. Cimrová and D. Neher, *J. Appl. Phys.* **79**, 3299 (1996).

[19] H. Becker, S. E. Burns, and R. H. Friend, *Phys. Rev. B* **56**, 1893 (1997).

[20] J.-S. Kim, P. K. H. Ho, N. C. Greenham, and R. H. Friend, *J. Appl. Phys.* **88**, 1073 (2000).

[21] R. R. Chance, A. Prock, and R. Silbey, *Adv. Chem. Phys.* **37**, 1 (1978).

[22] R. R. Chance, A. Prock, and R. Silbey, *J. Chem. Phys.* **62**, 2245 (1975).

[23] R. R. Chance, A. H. Miller, A. Prock, and R. Silbey, *J. Chem. Phys.* **63**, 1589 (1975).

[24] K. B. Kahen, *Mat. Res. Soc. Symp.* **660**, JJ4.2 (2001).

[25] A. L. Buring and M. A. Ratner, *J. Phys. Chem.* **104**, 4704 (2000).

[26] K. Ujihara, *Phys. Rev. A* **12**, 148 (1975).

[27] G. Björk, S. Machida, Y. Yamamoto, and K. Igeta, *Phys. Rev. A* **44**, 669 (1991).

[28] G. Björk, *IEEE J. Quan. Elec.* **30**, 2314 (1994).

[29] D. G. Deppe and C. Lei, *J. Appl. Phys.* **70**, 3443 (1991).

[30] M.-H. Lu, C. F. Madigan, and J. C. Sturm, *Tech. Dig. Int. Elec. Dev. Meet.*, 607 (2000).

[31] M. Pope and C. E. Swenberg, *Electronic Processes in Organic Crystals and Polymers*, (Oxford University Press, New York, 1999).

[32] D. Z. Garbuzov, V. Bulović, P. E. Burrows, and S. R. Forrest, *Chem. Phys. Lett.* **249**, 433 (1996).

[33] Y. Cao, I. D. Parker, G. Yu, C. Zhang, and A. J. Heeger, *Nature* **397**, 414 (1999).

[34] M. Wohlgenannt, K. Tandon, S. Mazumdar, S. Ramasesha, and Z. V. Vardeny, *Nature* **409**, 494 (2001).

[35] A. A. Shoustikov, Y. You, and M. E. Thompson, *IEEE J. Sel. Quan. Elec* **4**, 3 (1998).

[36] E. Hecht, *Optics*, 3rd ed. (Addison-Wesley, Reading Mass.1998).

[37] C. W. Tang, S. A. VanSlyke, and C. H. Chen, *J. Appl. Phys.* **65**, 3610 (1989).

[38] C.-T. Tai, (Intext Educational Publishers, Scranton, PA, 1971).

[39] A. Sommerfeld, *Electrodynamics*, (Academic Press, New York, 1952).

[40] J. J. Macklin, J. K. Trautman, T. D. Harris, and L. E. Brus, *Science* **272**, 255 (1996).

[41] Y. Shi, J. Liu, and Y. Yang, *J. Appl. Phys.* **87**, 4254 (2000).

[42] J. Liu, Y. Shi, L. Ma, and Y. Yang, *J. Appl. Phys.* **88**, 605 (2000).

Chapter 5

External Coupling of Light in OLEDs: Application of Modeling and Experiments

---

5.1 Introduction

The experimental work presented in this chapter serves two purposes. First of all, it provides a confirmation of the CCQMM model. Once the support is established, the model is used to calculate the amount of light trapped in the substrate and ITO/organic waveguiding modes *vs.* that which is emitted. OLED structures with varying Alq_3 and ITO thickness, as well as the index of refraction of the substrate are examined. In certain cases, as much as $\sim$50% of the internally emitted light goes into the external modes, more than twice the figure predicted by classical ray optics. Just as important, the work on shaped substrates demonstrates a practical means to increase external emission by the conversion of substrate modes

into external modes. Through the use of shaped high-index substrates, the total integrated external efficiency is increased by a factor of 2.3. This is the highest enhancement reported to date.

This chapter contains the measured far-field and edge-emission data from various OLEDs on planar and shaped substrates. It can be seen from eq. 4.14 that the field in the OLED and therefore, the emission characteristics, are sensitively dependent on the location of the emission center. As a result, devices discussed in this chapter are all bilayer OLEDs based on PVK/Alq_3, where the exciton location is defined by the location of the heterojuction. After a review of the experimental procedure in Sec. 5.2, the experimental data is correlated with model predictions in Sec. 5.3 and 5.4. The implications of these results to device optimization is discussed in Sec. 5.5.

5.2 Device fabrication and measurement procedures

5.2.1 Bilayer OLEDs on planar and shaped substrates

Bi-layer OLEDs were fabricated on either 0.7 mm-thick soda lime glass substrates coated with ITO ($t_{ITO} = 180$ nm, $n_{ITO} = 1.8$) purchased from Applied Films Corp., or on bare 0.5 mm-thick soda lime or high-index glass (Schott SFL57 glass, $n_{glass2} = 1.85$) substrates. 100 or 200 nm thick ITO layers ($n_{ITO} = 2.0$) were deposited onto

the bare glass substrates by radio frequency (rf) magnetron sputtering in an Ar plasma with no intentional heating. The sheet resistance of the 100-nm-thick ITO was approximately 100 Ω/sq, and the transmission was ∼80% in the visible. The room-temperature ITO deposition process was discussed in detail in Chapter 3. The hole transport layer in all devices was a 40 nm layer of PVK, deposited by spin-coating from a PVK/Chlorobenzene solution after the ITO surface was treated by an O_2 plasma [1]. The electron transport and emitting layer in all devices was Alq_3 (from TCI America, one of the higher quality vendors), deposited by vacuum sublimation at base pressures $< 10^{-6}$ Torr. The deposition rate was 0.1-0.3 nm/s. The cathodes were 30-50 nm of Mg:Ag (10:1) followed by an Ag cap evaporated through a shadow mask with 0.5 mm-diameter holes. The excitons are created in the Alq_3 near the PVK interface and assumed to move with a diffusion length of 20 nm, so varying the Alq_3 thickness changes the cathode-emission zone spacing as explained in Sec. 3.3.

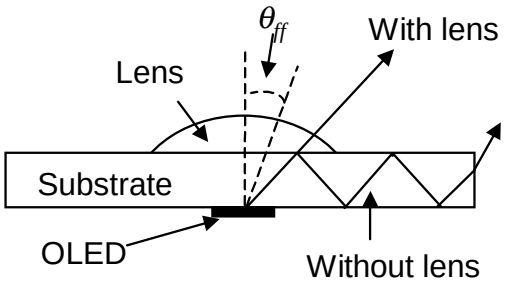

Figure 5.1: Attaching a lens to the backside of OLED converts some light from substrate modes to external modes.

All lenses used for effective substrate-shaping have a radius of curvature of 2.0 mm and a height of 1.5 mm, placing the OLED center exactly at the center of the curvature unless otherwise noted. If the OLED can be approximated as a point source, all rays would enter air at normal incidence, free of any refraction or total internal reflection (Figure 5.1). The substrate-waveguided light can be made to emit externally. The lenses were made from the same material as the substrates, and were attached to the backside of the substrate with index-matching oil. All devices were driven at a current density of 10 mA/cm^2. Far-field light emission was detected by a Si photodiode on a stage with azimuthal rotation. A linear polarizer was placed in front of the detector for measuring the TE and TM polarizations. For the edge emission experiments, the substrate were diced: the edges were vertical but not polished, so that they acted as a diffusive scatterer. The edge emission was measured by another Si photodiode placed immediately adjacent to the substrate (Figure 5.2). This photodiode was covered with black tape except for a thin slit to prevent stray surface emission from interfering with the measurement.

5.2.2 ITO thickness variations

ITO-coated soda lime glass substrates ($n_{ITO} = 1.8$, $t_{ITO} \simeq 165$ nm, Applied Films Corp.) were etched in $HNO_3 : HCl : H_20 = 1 : 9 : 10$ solution at room temperature where the etch rate is less than 10 nm/min. Four substrates were etched for various length of time. The resultant film thickness is measured by a Sloan Dektak III pro-

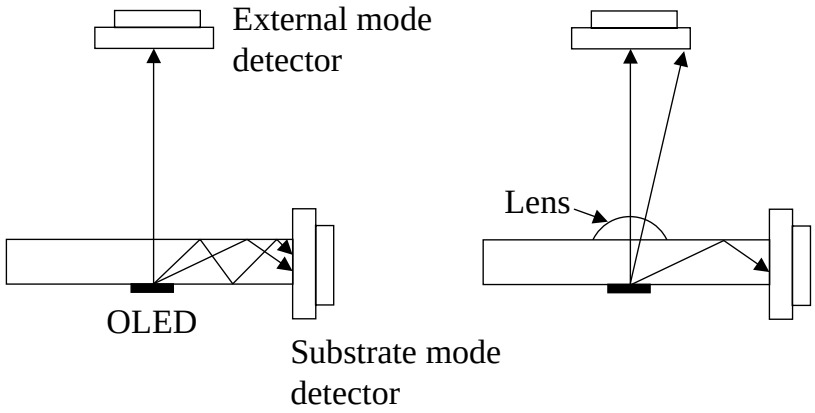

Figure 5.2: Setup for the simultaneous measurement of the external and edge emission with and without a lens attached to the back side of the OLED.

filometer to be 165 nm, 135 nm, 95 nm and 80 nm, respectively. The colors of the specular reflection ($\sim$40° from normal) from these substrates under a fluorescent light source as perceived by the unaided eye are purple, yellow, light yellow, and very pale purple, respectively. Bi-layer OLEDs with 40 nm PVK, 80 nm Alq_3, and Mg:Ag/Ag cathodes are fabricated as described above. The luminance-current density-voltage characteristics of these OLEDs were measured by an HP4145B semiconductor parameter analyzer and an calibrated Si photodiode.

5.2.3 OLEDs on polycarbonate substrates

Some early work involved OLEDs on 175-μm-thick polycarbonate (PC) substrates purchased from Goodfellows Corp. PC is soluble in solvents such as acetone and isopropanol, so the cleaning procedure was limited to scrubbing in Tergitol with cotton swabs. PC was chosen mainly for its surface flatness (as far as this particular

vendor was concerned) and its moderately high index of refraction ($n_{PC} = 1.595$). Single-layer PVK/PBD/C6 devices were fabricated (Sec. 2.5) on the PC substrates coated with room-temperature sputtered ITO (Sec. 3.4). The OLEDs generally exhibited high turn-on voltage and low efficiency due to the lower-quality ITO.

5.3 OLEDs on planar substrates

5.3.1 Introduction

The experimental data in this section are organized as follows: 1) OLEDs where the location of the emission zone is varied with varying Alq_3 layer thickness; 2) OLEDs where the thickness of the ITO layer is varied; and 3) OLEDs on high-index ($n_{glass2} = 1.85$) substrates.

5.3.2 Alq_3 thickness variations

The far-field intensity profiles from devices with Alq_3 layers varying from 20 - 80 nm are measured. The intensity profile of devices with thicker Alq_3 (40-80 nm) are qualitatively similar to the Lambertian profile, as has been observed in OLEDs elsewhere [2]-[4]. The exception was the device with a thin Alq_3 layer, where a significant peak in the intensity is observed in the TM polarized light (Figure 5.3). In the thin Alq_3 layer, all excitons are close to the metal surface where in-plane TM radiation dominates, as discussed following eq. 4.14. Coupled with the

transmission at the glass/air interface which falls off at large angles, this produced the peak in the TM intensity profile. The model results are in excellent agreement with the data.

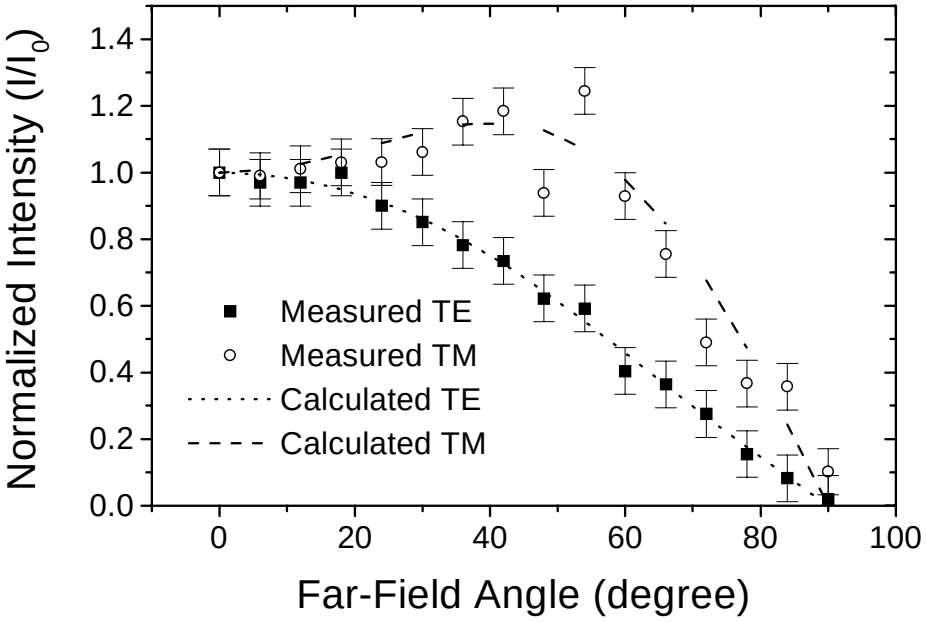

Figure 5.3: Modeling and experimental data of far-field intensity pattern of a planar OLED (soda lime glass/180 nm ITO/40 nm PVK/20 nm Alq_3/Mg:Ag). Solid square and upper triangle: measured TE and TM intensity. Solid and dashed lines: theory. The model results is normalized to the experimental data in the normal direction.

By integrating or summing $I(\theta_o)$ (cf. eq. 4.36) over the appropriate ranges: 0 to θ_{c1} ($= \sin^{-1} n_{air}/n_{Alq}$) for external modes, etc., the proportion of the internally generated emission that goes into each mode can be computed. First, the emission as a function of the thickness of the Alq_3 layer for OLEDs on standard soda lime glass substrates is examined (Figure 5.4). The overall height of the columns represent the rate of radiative decay, W_R. The sharp decrease in radiative output

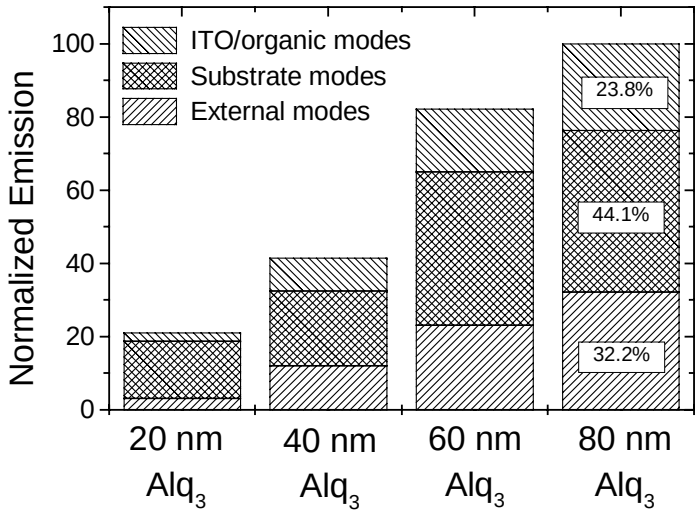

Figure 5.4: CCQMM model: calculated distribution of energy into external, substrate and ITO/organic modes as a function of Alq_3 thickness for OLEDs with the structure: soda lime glass/180 nm ITO/40 nm PVK/Alq_3/cathode.

with Alq_3 layer thickness can be attributed primarily to the cathode quenching effect as in Figure 4.5. In the device with 80 nm Alq_3, most of the excitons are close to the antinode of the electric field in the microcavity (Figure 4.8) where according to eq. 4.14, both the TE and antinodal TM contributions are maximized, leading to a large external and total emission. In contrast, in the device with 20 nm Alq_3, the excitons are close to the metal surface where the nodal TM contribution at large angles dominates. The large-angle radiation suffers from TIR resulting in far less external emission as a percentage of the total radiation.

It should be pointed out that in the 80-nm-Alq_3 device roughly one third of the emission is into the external modes, much greater than the 18.9% figure

according to classical ray optics. The external emission in the forward half plane of a series of OLEDs on standard substrates with Alq_3 layer ranging from 20 nm to 80 nm was computed by integrating the measured intensity profiles according to eq. 4.5. The normalized external quantum efficiency (photon/electron) as a function of the thickness of the Alq_3 layer is plotted in Figure 5.5 along with the calculated values by both the CCQMM model and the half-space dipole model [4].

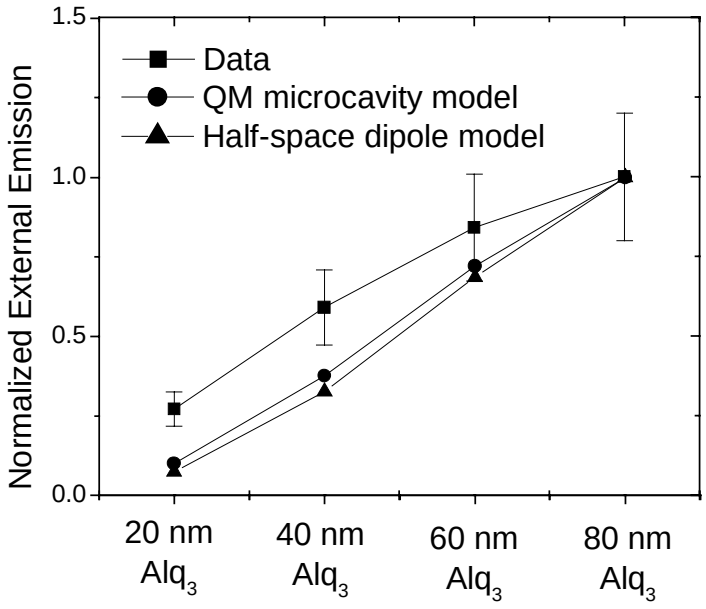

Figure 5.5: Normalized external emission vs. thickness of the Alq_3layer. Squares: data, circles: QM microcavity theory, up triangles: half-space dipole model. The devices are of the structure soda lime glass/180 nm ITO/40 nm PVK/Alq_3/Mg:Ag.

The external quantum efficiencies decrease with decreasing Alq_3 thickness due to cathode quenching as expected; however, both models under-predict the efficiencies in devices with thinner Alq_3 layers, while the CCQMM model is slightly more accurate. This discrepancy can be attributed to the fact that a thinner Alq_3

layer increases proportionally the amount of electron current relative to that of holes, thus improving the carrier balance, making the device more efficient [5]. An alternative explanation is that the actual exciton recombination profile shrinks with decreasing Alq_3 thickness due to dissociation of excitons at the cathode, which pins the exciton density to zero. This narrower exciton recombination profile makes the average exciton recombination site farther away from the cathode in devices with thinner Alq_3 than the model assumptions. By the same cathode quenching argument, the external emission will then be larger than the model predictions.

5.3.3 ITO thickness variations

The thickness of the ITO layer affects the modal distribution in two ways. It alters the ITO/organic modes by changing the combined thickness of the ITO/organic layer, and it alters the external and substrate modes through interference effects. It is possible to have an ITO layer so thin that no ITO/organic mode exists for most of the visible spectrum. In the same vein as in Figure 5.4, the distribution of light emission is calculated for OLEDs with 100 nm and 200 nm-thick ITO layers (Figure 5.6). The emission into the ITO/organic modes in the OLED with the thinner ITO layer is drastically suppressed, since the cut-off wavelength is only slightly above the low end of the visible spectrum. On the other hand, the cut-off is above the peak emission wavelength of Alq_3 in the OLED with the 200 nm ITO layer, resulting in much stronger ITO/organic modes. The absolute value of

the emission into the external and substrate modes is moderately affected by the interference effects, but not enough to prevent the proportion of external emission from increasing with decreasing ITO layer thickness. According to our model, as much as ∼52% of the light is emitted externally in the planar device with 100 nm ITO and 80 nm Alq_3. This is much greater than the ∼20% figure arrived at by ray optics. On the other hand, the half-space dipole model predicts an external coupling efficiency of ∼45% irrespective of the ITO or organic layer thickness. The overall external quantum efficiency is not as drastically affected, since the suppression of the ITO/organic modes rather than an increase in the external modes is responsible for this high external coupling efficiency. Design of optimal ITO thickness for various radiative *vs.* non-radiative decay rates is discussed in Sec. 5.6.

5.3.4 High-index substrates

The use of high-index (Schott SFL57 glass, $n_{glass2} = 1.85$) substrates eliminates TIR at the ITO/glass interface, which therefore converts the ITO/organic modes into substrate modes [16]. From classical ray optics, the external emission is expected to be independent of the index of the substrate. This is confirmed by the measured external quantum efficiency of identically fabricated OLEDs on both standard soda lime glass and high-index glass substrates (Table 5.2), as well as the observed far-field intensity profile (Figure 5.9). The distribution of light emission

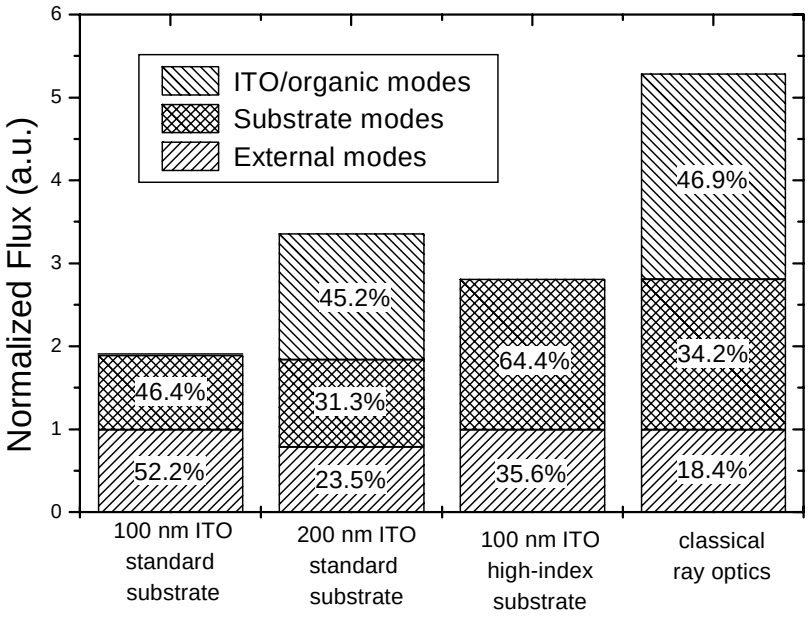

Figure 5.6: Calculated distribution of emission into external, substrate and ITO/organic modes for various OLED structures (glass substrate/ITO/40 nm PVK/80 nm Alq_3/cathode). The fluxes into the external modes of the sample with 80 nm Alq_3 on standard substrates and the classical model are normalized to 1.

for an OLED on high-index substrates is shown in Figure 5.6 with the external emission normalized to that of an identical device on soda lime glass substrates. By converting the ITO/organic modes and avoiding their suppression due cut-off, the device on high-index substrate has more emission into the substrate modes and a higher total radiative output compared with an identical device on standard soda lime glass substrates. While the amount of externally emitted light is similar in OLEDs on planar high-index and standard substrates (e.g. Figure 5.6), if the substrate modes in the high-index case can be harvested, the external emission could be increased by nearly 3X. This is demonstrated in the next section.

5.4 OLEDs on shaped substrates

5.4.1 Early work with OLEDs on shaped soda lime glass substrates

Since a large fraction of light is trapped by waveguiding modes in the substrate and ITO/organic layers, substrate patterning has been used to destroy the waveguides and redirect the light externally. The external coupling efficiency has been improved by a factor of 1.9 ± 0.2 by etching grooves in the glass around the OLED to redirect light trapped in the substrate and organic/ITO layers [11]. Nevertheless, this method does not lend itself well to the fabrication of device arrays, since metal lines and/or circuitry for passive or active matrix displays would have to cross the deep grooves. Backside patterning (viewing side) can destroy the substrate waveguide and redirect the light externally without disturbing the devices on the front side. Micro-silica spheres sintered to the backside of the glass substrate have been used to increase the external emission up to 70% [12]. Substrate modification by means of attaching a lens to the backside is the method adopted in this work (Figure 5.1) [13].

Earlier work based on single layer PVK/PBD/C6 polymer OLEDs used a number of lens geometries (Table 5.1) [13]. The far-field intensity profiles were measured (Figure 5.8) and are summarized in Table 5.1. The distance from the center of the lens to the OLED can be chosen to enhance the normal direction

intensity by a factor of 9.5 (trial 3) or to increase the integrated external emission by a factor of 2.0 (trial 2).

Table 5.1: Substrate and lens parameters (as defined in Figure 5.7) for different external coupling experiments. I_{normal}/I_0 and F/F_0 represent the ratio of normal emission intensity and total surface emitted light respectively to the results obtained for identical devices fabricated on planar substrates of the same substrate material.

Trial	Substrate Material	Lens Material	R_{lens} (mm)	ρ_{lens} (mm)	$t_{subs,eff}$ (mm)	$\theta_{subs,max}$	d (mm)	I_{normal}/I_0 ± 0.1	F/F_0 ± 0.1
1	Glass *(n=1.51)*	N/A	N/A	N/A	0.7	N/A	N/A	1.0	1.0
2	Glass *(n=1.51)*	Glass *(n=1.51)*	3.4	3.4	0.7	78º	+1.0	3.6	2.0
3	Glass *(n=1.51)*	Glass *(n=1.51)*	3.4	3.4	2.0	60º	+2.3	9.5	1.6
4	Glass *(n=1.51)*	Silicone *(n=1.41)*	2.7	2.4	1.9	51º	+0.6	2.1	1.6

The above experiments can at best hope to capture light wave-guided in the substrate, but not the light waveguided in the ITO/organic layers. That will be addressed with in the next section.

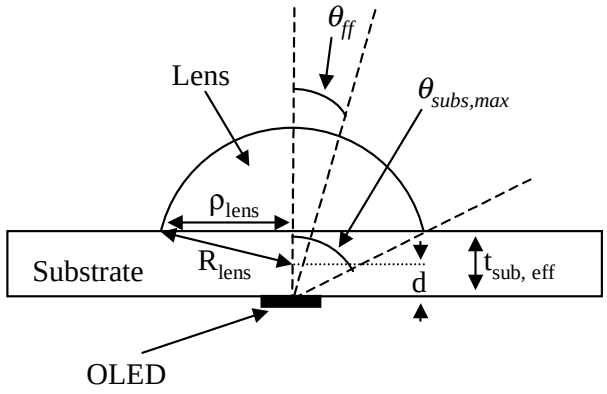

Figure 5.7: The relevant parameters shown are given for each experimental trial in Table 5.1. Note that the ray used to define the far-field angle, θ_{ff}, is drawn for the d=0 case, while in the diagram d, the offset between the center of curvature of the lens and the OLED, is drawn as non-zero so that it can be clearly identified.

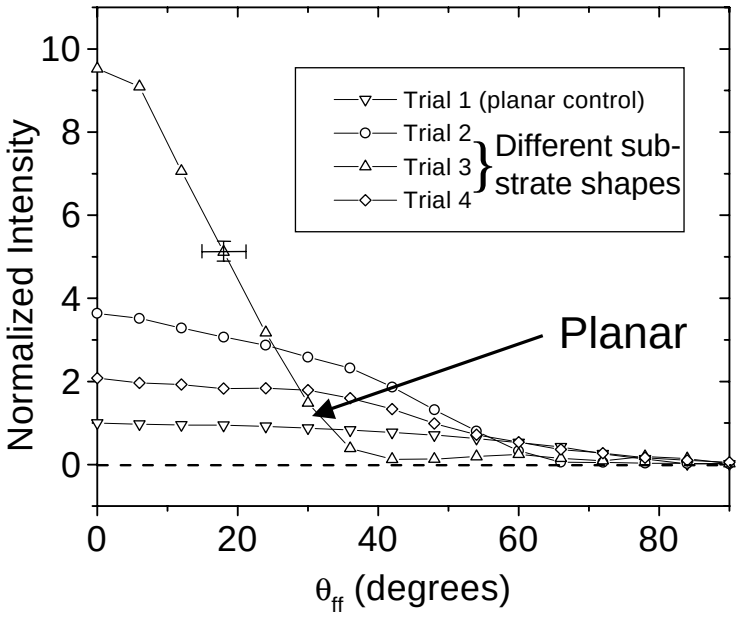

Figure 5.8: Measured far-field emission pattern for devices on soda lime glass substrates with (trial 2-4) and without lenses (trial 1). The lens shapes used in trials 2-4 are described in Table 5.1. (OLED structure: 180 nm ITO/100 nm (PVK/PBD/C6)/Mg:Ag/Ag). (From Ref. [13])

5.4.2 OLEDs on shaped high-index substrates

Figure 5.9 shows the far-field intensity pattern of a bilayer OLED with an 80 nm Alq_3 layer on both standard and high-index substrates, with and without a lens attached. As expected, in devices fabricated on planar substrates, the far-field intensity patterns are the same, irrespective of the index of the substrates (discussed in Sec. 5.3.4). Once a lens of the same index as the substrate is attached, the devices on the high-index substrates showed an average increase by a factor of 3.2 in the intensity in the normal direction versus an average increase by a factor of 2.2 for the devices on the standard substrates. These results are very close to the ideal scenario where the OLED is a point source at the center of curvature of the lens where the expected increase is given by n^2_{glass}, i.e., by factors of 3.4 and 2.3 for high-index and standard glass substrates respectively.

High-index substrates not only convert the ITO/organic modes, but also have a focusing effect on the distribution of emitted light rays. With a large substrate index ($n_{glass2} = 1.85$), diffraction from the emitting layer ($n_{Alq} = 1.71$) bends light rays forward in the substrate. In the ideal scenario where the OLED is a point source at the center of the curvature of the lens, the far-field intensity pattern in air is identical to the ray distribution in the substrate, so the emission in air is also more concentrated in the normal direction. Thus if we were to look at the light emission in the forward 120° cone, where most of the viewing takes place, the amount of increase in external quantum efficiency is even more remarkable. The

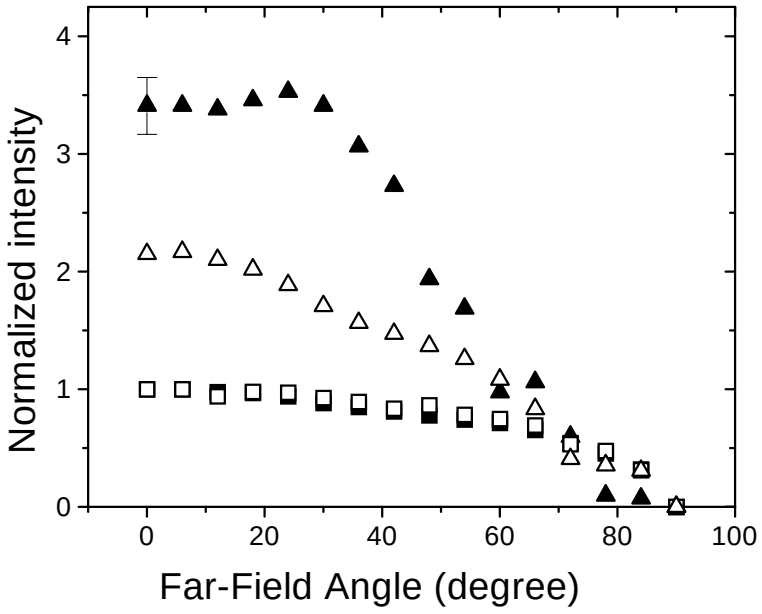

Figure 5.9: Far-field intensity profile of OLEDs (glass substrate/100 nm ITO/40 nm PVK/80 nm Alq_3/Mg:Ag/Ag) on both high-index and standard glass substrates. Open and closed squares: planar soda lime and high-index glass substrates, open triangles: shaped soda lime glass substrate, closed triangles: shaped high-index substrate.

observed increase was by a factor of 2.9 for the device on high-index substrate, and only a factor of 1.7 for the corresponding device on standard substrate.

The expected increase in the external luminous flux by attaching a lens with the same index as the substrate was also calculated assuming the same lens and OLED dimensions using the CCQMM model for substrate indices ranging from 1.3 to 2.0 (Figure 5.10). The energy distribution into different modes for the structure ITO (100 nm)/PVK (40nm)/Alq_3 (80 nm) was already shown in Figure 5.6. It is already qualitatively clear from this figure that for high substrate index of refraction more light is available for harvesting by attaching the lens. The

Table 5.2: Summary of increases in luminous flux for OLEDs on standard and high-index substrates after attaching a lens to the backside of the substrate (Figure 5.9). The measured external quantum efficiency (external photon/electron) is the same for both types of devices as measured from a group of large-area planar OLEDs.

	Standard glass		High-index glass	
	Theo.	Expt.	Theo.	Expt.
Q.E. for planar device	N/A	0.35%	N/A	0.36%
Flux increase in forward half-space	1.82X	1.5X	2.62X	2.3X
Flux increase in forward 120° cone	1.82X	1.7X	3.20X	2.9X

predicted enhancement factor increases monotonically with the index of refraction of the substrate. As the index of the substrate increases beyond that of the emitting layer ($n_{Alq} = 1.71$), emission becomes more concentrated in the forward direction due to refraction. Hence for higher substrate indices, the luminous flux in the forward 120° cone shows a larger increase compared with that in the entire forward half space for higher substrate indices. The model predictions of the increase in the forward half plane and 120° cone for both types of substrates agree well with the data. The discrepancy between theoretical and experimental values can be attributed to the finite size of the OLEDs and the imperfections at the edge of the lenses (Table 5.2).

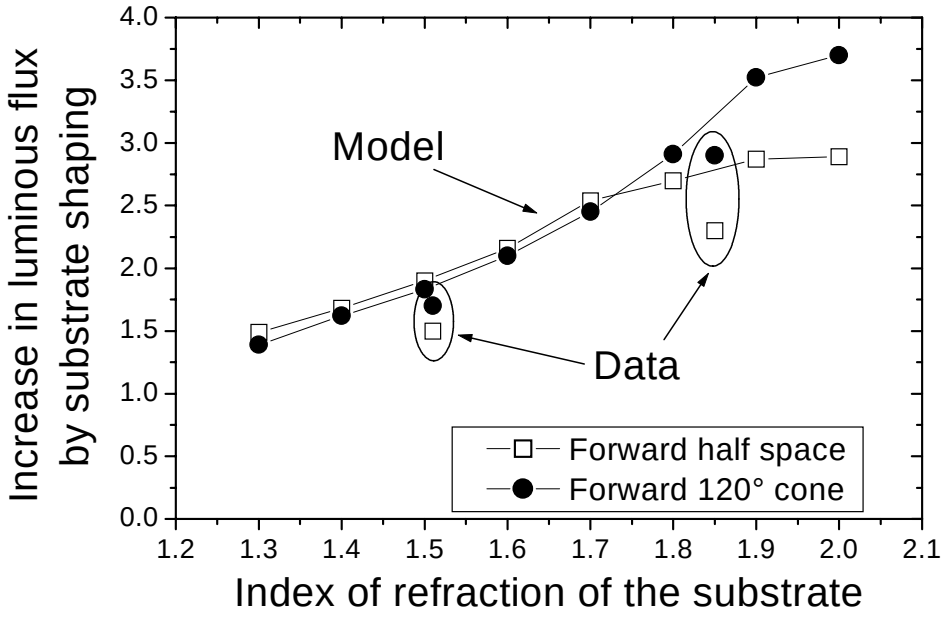

Figure 5.10: Predicted increases in luminous flux emitted in the forward half plane and the forward 120° cone as a function of the index of refraction of the substrate, assuming complete conversion of substrate modes into external modes. OLEDs have the structure: substrate/100 nm ITO/40 nm PVK/80 nm Alq_3/cathode.

5.5 Experimental measurement of external *vs.* substrate emission

Direct measurement of the substrate and ITO/organic waveguided light is difficult; therefore, we devised a method that measures indirectly the ratio of light emission into the external modes over that into the substrate modes, i.e., $\eta_{cp}^{ext}/\eta_{cp}^{sub}$. A portion of substrate waveguided light is made to emit externally by attaching a lens to the backside of the substrate. Due to the thickness of the substrate, it was assumed that attaching the lens negligibly affected the behavior of the OLED. Since the ITO/organic modes were heavily attenuated by the metal cathode and the absorption in the ITO layer, we assumed that the edge emission was exclusively from the substrate modes [6]. Assuming the absence of scattering that mixes the modes, it follows that

$$\begin{aligned} F_{ext} + F_{sub} &= F'_{ext} + F'_{sub} = r_1 F_{ext} + r_2 F_{sub} \\ \frac{\eta_{cp}^{ext}}{\eta_{cp}^{sub}} &= \frac{F_{ext}}{F_{sub}} = \frac{1 - r_2}{r_1 - 1} \end{aligned} \tag{5.1}$$

where F_{ext} and F_{sub} are the emissions in the external and substrate modes in a planar sample, and the primed symbols are the emissions after lens attachment. r_1 and r_2 are defined as F'_{ext}/F_{ext} and F'_{sub}/F_{sub}, respectively.

The measured ratios of for various devices are summarized in Table 5.3. In the OLED with the structure: soda lime glass/100 nm ITO/ 40 nm PVK/ 80 nm Alq_3/ Mg:Ag/Ag, our measurements indicated a ratio of 1.30 $\pm$ 0.20. In

other words, there is more emission into the external modes than the substrate modes. This is confirmed by our model, which predicted a ratio of 1.12. This structure is the same as the one modeled in Figure 5.6; therefore, the ratio of 1.12 is obtained by dividing 52.2% by 46.4%. When the thickness of the ITO is increased to 200 nm, a $\eta_{cp}^{ext}/\eta_{cp}^{sub}$ ratio of 0.51 ± 0.08 was obtained, indicating that emission into the substrate modes was almost twice as into the external modes. In the OLED on high-index substrates, the ITO/organic modes are redirected into the substrate modes; therefore, we can expect substantially less emission into the external modes than into the substrate modes. As expected, we obtained a ratio of only 0.41 ± 0.06. The model predicted $\eta_{cp}^{ext}/\eta_{cp}^{sub}$ ratios of 0.75 and 0.56 for the device with thicker ITO and on high-index substrate, respectively. Although discrepancies between the data and the modeling results exist, there was a recognizable pattern that confirmed the reduction of emission into the external modes relative to the substrate modes as the ITO thickness was increased, and when high-index substrates were used. The agreement was reasonable despite the simplicity of our assumptions, chief among which is probably the lack of mode mixing due to scattering.

Table 5.3: Measured values of $\eta_{cp}^{ext}/\eta_{cp}^{sub}$ compared with the calculations based on the CCQMM model for different device structures. The thicknesses of the PVK and Alq_3 layers are 40 nm and 80 nm respectively.

Sample	Measured	Model
Soda lime glass/100 nm ITO/PVK/Alq_3/Mg:Ag/Ag	1.30 ± 0.20	1.12
Soda lime glass/200 nm ITO/PVK/Alq_3/Mg:Ag/Ag	0.51 ± 0.08	0.75
High-index glass/100 nm ITO/PVK/Alq_3/Mg:Ag/Ag	0.41 ± 0.06	0.56

5.6 Structural optimization of external EL efficiency

5.6.1 Introduction

It is clear from Figure 5.5 that microcavity effects are at least as important as the transport of carriers in device optimization through layer thickness adjustments. In this section, we examine various structures and parameters using model and experiment to see what structure gives the most external light emission. Varying organic, ITO thicknesses and shaped substrates are considered, as well as organic materials with different intrinsic PL efficiencies are examined. The discussion is based on a bilayer OLED, but is applicable to both single-layer OLEDs and more complicated structures.

5.6.2 Organic and ITO thickness variations

Radiative emission is maximized for an exciton at an antinode of the electrical field in the cavity. For a perfect metallic cathode, the first antinode is a quarter wavelength away, or approximately 77 nm at the peak emission wavelength (λ = 524 nm). Because the excitons diffuse away from the PVK/Alq_3 interface, the optimal Alq_3 thickness should slightly exceed $\lambda/4$ (Figure 4.8). On the other hand, thick Alq_3increases the operating voltage, so in practice the best power efficiency is obtained with Alq_3 thicknesses around 50 nm [6]. Further device improvement is possible if the output coupling can be decoupled from the charge transport.

There is a similar rule of thumb for the distance between the exciton and the dominant reflective interface (ITO/glass) on the anode side for optimizing external emission. That distance should be a multiple of half wavelength for maximum constructive interference of electrical fields at the point of the exciton [14]. (Reflection at the ITO/glass interface contributes no phase change.) Again using the case of λ = 524 nm as an example the optimal ITO thickness is given by $t_{PVK}\, n_{PVK} + t_{ITO}\, n_{ITO} = \lambda/2$ [14]. The optimal ITO thickness according to this rule is found to be approximately 100 nm, assuming t_{PVK} = 40 nm, n_{PVK} = 1.67, and n_{ITO} = 2.0. Figure 5.11 shows $\eta_{exciton}$, η_{cp}^{ext}, $\eta_R = W_R/W_{TOT}$, and $\eta_{ET} = W_{ET}/W_{TOT}$ computed by the CCQMM model as a function of ITO thickness for OLEDs on soda lime glass. The efficiencies are calculated for three material systems with η_{PL} = 0.32, 0.10 and 0.90. The external coupling efficiency, η_{cp}^{ext} is

independent of the non-radiative processes, thus is also independent of η_{PL}, and a peak value of 52.6 % is observed at an ITO thickness of 100 nm, as predicted by the simple rule of thumb noted above. But calculation of the distribution into the three radiative modes reveals that the suppression of ITO/organic modes due to the thinness of the ITO layer (Figure 5.6) also plays a role. As the ITO thickness increases above 100 nm, the ITO/organic waveguide starts to accommodate more modes and η_{cp}^{ext} decreases rapidly.

However, the more relevant parameter to device optimization is the number of photons emitted externally per singlet exciton, $\eta_{exciton}$, which is as product of η_{cp}^{ext} and η_R. The total decay rate, W_{TOT}, does not change appreciably with the change in the thickness of the ITO layer; however, the relative strength of the radiative decay and the dipole-cathode energy transfer is seen to depend sensitively on the ITO thickness (Figure 5.11). With a thicker ITO, the increase in the rate of radiative decay, W_R, together with the decrease in dipole-cathode energy transfer, W_{ET}, increases η_R faster than the decrease in η_{cp}^{ext}, resulting in a notable increase in $\eta_{exciton}$. 125 nm of ITO gives the most efficient device on planar substrates where 12.6% of the singlet excitons emit a photon externally, whereas the device on 50 nm ITO is over 30% less efficient at $\eta_{exciton} = 8.7\%$. It remains a possibility that in some highly efficient devices ($\eta_{PL} \simeq 1,\ W_{ET} \simeq 0$), a high $\eta_{exciton}$ can be achieved with thin ITO layers that eliminates the ITO/organic modes.

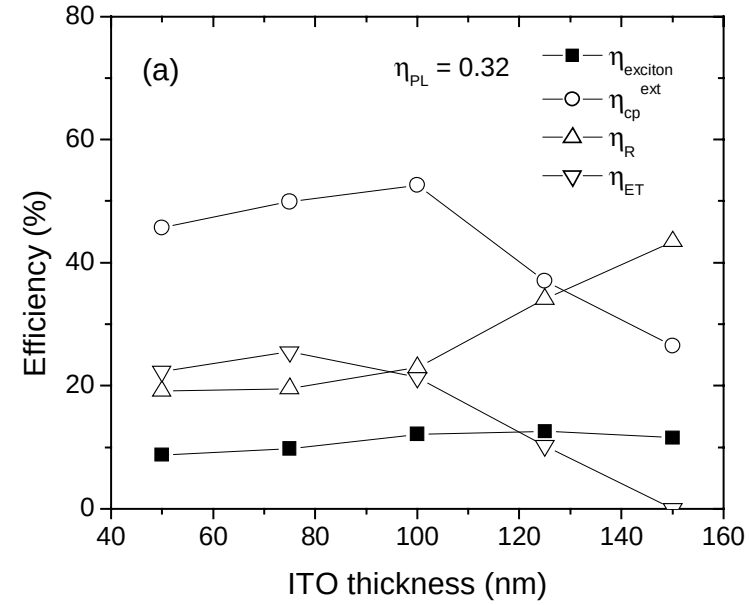
(a)
η_{PL} = 0.32
$\eta_{exciton}$
η_{cp}^{ext}
η_R
η_{ET}
Efficiency (%)
ITO thickness (nm)
0
20
40
60
80
40
60
80
100
120
140
160

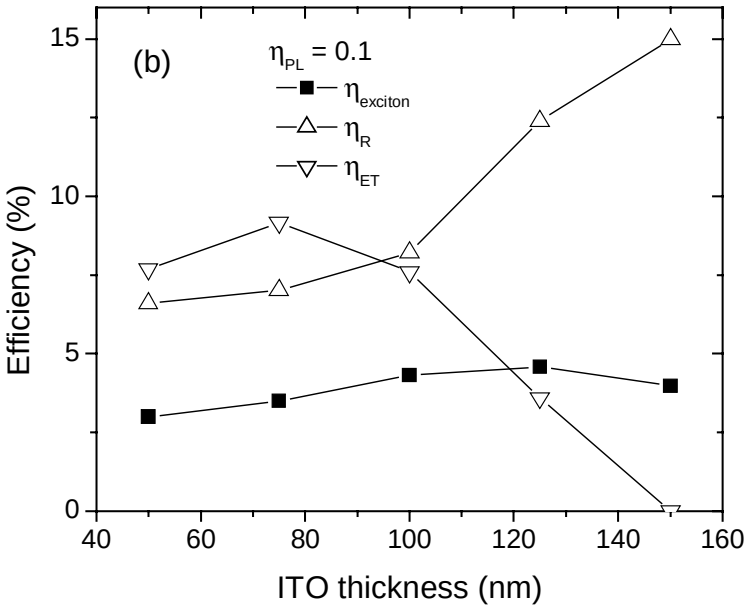
(b)
η_{PL} = 0.1
$\eta_{exciton}$
η_R
η_{ET}
Efficiency (%)
ITO thickness (nm)
0
5
10
15
40
60
80
100
120
140
160

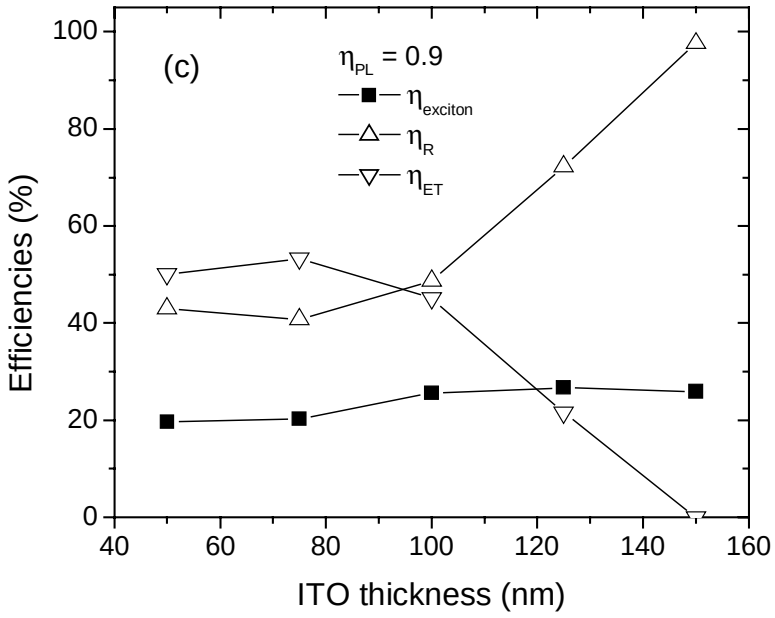

Figure 5.11: Various efficiencies *vs.* ITO thickness calculated for OLEDs with the structure: soda lime glass/ITO/40 nm PVK/80 nm Alq_3/Ag. Closed squares: $\eta_{exciton} = W_{ext}/W_{TOT}$, open circles: $\eta_{cp}^{ext} = W_{ext}/W_R$, open up triangles: $\eta_R = W_R/W_{TOT}$, and open down triangles: $\eta_{ET} = W_{ET}/W_{TOT}$. (a) $\eta_{PL} = 0.32$, (b) $\eta_{PL} = 0.1$, (c) $\eta_{PL} = 0.9$.

Figure 5.12 shows calculated $\eta_{exciton}$ as a function of ITO thickness for OLEDs on both planar and shaped soda lime glass substrates along with the experimentally measured external quantum efficiencies for devices on planar substrates. Shaped substrates ($\beta = 1$) increase $\eta_{exciton}$ by a factor of more than 2 compared with planar substrates as shown previously. Among the devices on planar substrates, the most efficient devices was one on 125 nm of ITO, whereas among the devices on shaped substrates, the most efficient device is on 150 nm of ITO ($\eta_{exciton}$ = 26.8%). The different ITO thickness alters the intensity distribution sufficiently that the optimization is dependent on whether shaped substrate is used.

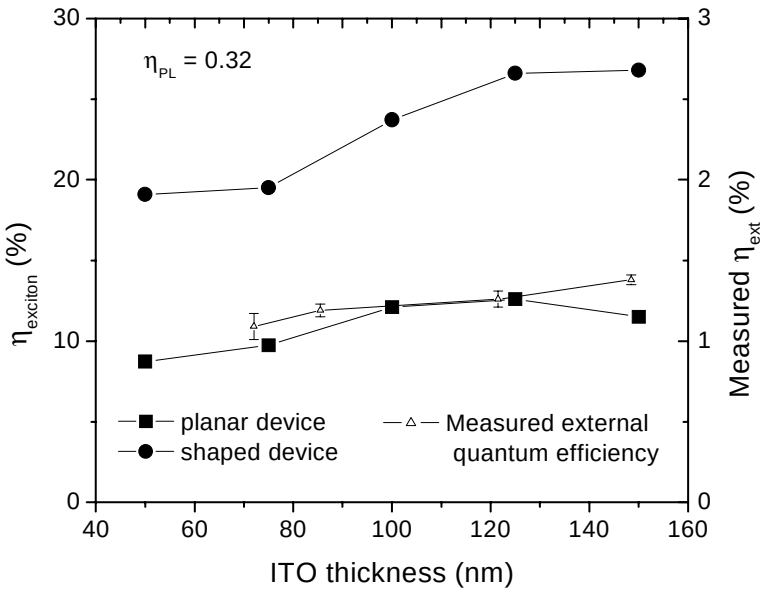

Figure 5.12: Calculated $\eta_{exciton}$ and measured external quantum efficiencies for OLEDs of the structure soda lime glass/ITO ($n_{ITO} = 2.0$)/40 nm PVK/80 nm Alq_3/Ag where the intrinsic PL efficiency is 0.32. Squares: planar substrate, circles: shaped substrate ($\beta = 1$), triangles: measured external quantum efficiency of the planar OLEDs. The lines are guides to the eye only.

The measured external quantum efficiency, η_{EL}^{ext} increases slightly with increasing ITO thickness as predicted (Figure 5.12). Because the total radiative emission is higher in the device with 150 nm ITO as indicated by η_R in Figure 5.11, it is believed that the scattering of light from the substrate and ITO/organic modes may have caused the device with 150 nm ITO to have a higher η_{EL}^{ext} than the one with 125 nm ITO. Comparing η_{EL}^{ext} with $\eta_{exciton}$ in Figure 5.12, it can be deduced that roughly 10% of the injected electrons result in a singlet exciton in these Alq_3/PVK based devices. This is exactly the same figure arrived at by Bulović et al. for Alq_3/NPD based devices. It is appropriate to revisit eq. 4.10:

$$\eta_{EL}^{ext} \quad = \quad \eta_{cp}^{ext}\, \eta_{EL}^{int} = \gamma\, r_{st}\, \eta_{exciton}$$

where γ is the number of exciton forming events per electron flowing through the OLED and r_{st} is the fraction of singlet excitons. r_{st} equals 0.22±0.03 as shown by Baldo et al. [10], so it follows that γ is 0.4. That is, 40% of the electrons injected form excitons (singlet and triplet).

5.6.3 Shaped substrates

The highest $\eta_{exciton}$ is obtained by using shaped high-index substrates. It converts ITO/organic modes (irrespective of the thickness of the ITO layer) into substrate modes which can be harvested by substrate patterning techniques. It also offers two advantages over the thin ITO/standard glass substrate combination. Firstly, from an engineering point of view, high-index substrates allow a high conversion

efficiency, β, for substrate features of the same size due to the favorable refraction of light rays that enter the substrate. Secondly, the total radiative emission is higher in an OLED on a high-index substrate than on a thin ITO/standard glass substrate (Figure 5.6), which translates into higher external emission in the presence of competing non-radiative processes. Note however, if the non-radiative processes are not significant, a standard, planar substrate with a thin ITO layer that suppresses the ITO/organic modes will actually support an OLED with a higher external emission than on a planar, high-index substrate (cf. Figure 5.6). The choice of substrates as a function of the relative radiative and non-radiative decay rates for planar and shaped substrates is summarized in the table below.

Table 5.4: Choice of substrates depending on the relative radiative and non-radiative decay rates for devices on planar and shaped substrates.

	Planar substrate $\beta = 0$	Shaped substrate $\beta \approx 1$
Phosphorescent or other high internal quantum efficiency systems: $W_R >> W_{NR}$	Standard substrates better	High-index substrates better
Low internal quantum efficiency systems: $W_{NR} > W_R$	Standard substrates slightly better	High-index substrates much better

5.7 Conclusions

A combined classical and QM microcavity model is used to describe the recombination of excitons in an OLED. The calculated emission rates into the external,

substrate, and ITO/organic modes differ substantially for the classical ray optics result and are strong functions of the indices and thicknesses of the layers. One of the chief shortcomings of the classical model is the failure to consider the cut-off effects of the ITO/organic waveguide. External coupling efficiencies in excess of 50% are predicted by the CCQMM model to be possible in certain planar structures without substrate patterning. The model accurately predicts the far-field intensity pattern, and the external/substrate mode ratio as determined by edge emission experiments. Shaped substrates, especially in conjunction with high-index substrates increase the integrated external emission significantly. The measured increase agrees well with the calculated value. Finally, it is discovered that the external coupling efficiency, η_{cp}^{ext}, and the efficiency of external emission for a singlet exciton, $\eta_{exciton}$, are not necessarily correlated. Device optimization should aim to maximize $\eta_{exciton}$, the accurate determination of which requires the combined classical and QM model. The layer thickness optimization also depends on whether a planar or shaped substrate is used, and whether the decay rate of excitons are dominated by radiative or non-radiative processes.

References

[1] C. C. Wu, C. I. Wu, J. C. Sturm and A. Kahn, *Appl. Phys. Lett.* **70**, 1348 (1997).

[2] N. C. Greenham, R. H. Friend, and D. D. C. Bradley, *Adv. Mater.* **6**, 491 (1994).

[3] C. F. Madigan, M.-H. Lu, and J. C. Sturm, *Appl. Phys. Lett.* **76**, 1650 (2000).

[4] J.-S. Kim, P. K. H. Ho, N. C. Greenham, and R. H. Friend, *J. Appl. Phys.* **88**, 1073 (2000).

[5] H. Aziz. Z. D. Popovic, N.-X. Hu, A.-M. Hor, and G. Xu, *Science* **283**, 1900 (1999).

[6] V. Bulović, V. B. Khalfin, G. Gu, P. E. Burrows, D. Z. Garbuzov, and S. R. Forrest, *Phys. Rev. B* **58**, 3730 (1998).

[7] Y. Cao, I. D. Parker, G. Yu, c. Zhang, and A. J. Heeger, *Nature* **397**, 414 (1999).

[8] Z. Shuai, D. Beljonne, R. J. Silbey, and J. L. Brédas, *Phys. Rev. Lett.* **84**, 131 (2000).

[9] M. Wohlgenannt, K. Tandon, S. Mazumdar, S. Ramasesha, and Z. V. Vardeny, *Nature* **409**, 494 (2001).

[10] M. A. Baldo, D. F. O'Brien, M. E. Thompson, and S. R. Forrest, *Phys. Rev. B* **60**, 14422 (1999).

[11] G. Gu, D. Z. Garbuzov, P. E. Burrows, S. Venkatesh, and S. R. Forrest, *Opt. Lett.* **22**, 396 (1997).

[12] T. Yamasaki, K. Sumioka, and T. Tsutsui, *Appl. Phys. Lett.* **76**, 1243 (2000).

[13] C. F. Madigan, M.-H. Lu, and J. C. Sturm, *Appl. Phys. Lett.* **76**, 1650 (2000).

[14] T. Watanabe, K. Nakamura, S. Kawami, Y. Fukuda, T. Tsuji, T. Wakimoto, S. Miyaguchi, M. Yahiro, M.-J. Yang, and T. Tsutsui, *Syn. Met.* **122**, 203 (2001).

[15] M.-H. Lu, C. F. Madigan, and J. C. Sturm, *Mat. Res. Soc. Symp. Proc.* **621**, Q3.7 (2000).

[16] M.-H. Lu, C. F. Madigan, and J. C. Sturm, *Tech. Dig. Int. Elec. Dev. Meet.*, 607 (2000).

[17] M.-H. Lu and J. C. Sturm, *Appl. Phys. Lett.* **78**, 1927 (2001).

[18] M.-H. Lu and J. C. Sturm, *J. Appl. Phys.*, accepted.

Chapter 6

An Active-Matrix OLED Display Pixel Based on Amorphous Silicon Thin Film Transistors

---

6.1 Introduction

OLEDs based on small molecules or polymers [1, 2] have attracted enormous attention because of their potential flat panel display applications. Large-area, high-resolution displays require active-matrix addressing. Passive-matrix OLED displays consist of an organic layer sandwiched in between perpendicular row (cathode) and column (anode) electrodes, where each intersection of row and column electrodes defines a pixel. On the other hand, active-matrix OLED displays have thin-film-transistors within each pixel, and have the advantage that the OLEDs may be operated in DC rather than in low duty cycle, high-intensity, pulsed operation, so that the peak current and thus the OLED driving voltage may be much

lower. This effect and the lower I^2R loss in the row and column lines significantly improve the system power efficiency. The lifetime *vs.* initial luminance reported by some groups are such that a low intensity, long duty cycle drive scheme should be favored [3, 4]. In addition, a pixel short can cause an entire line defect in a passive-matrix display, but only a single pixel defect in an active-matrix display.

Several developmental efforts on AMOLED displays are based on poly-crystalline silicon (p-Si) thin film transistor (TFT) technology [5, 6]; however, due to the large installed manufacturing base for amorphous silicon (α-Si) TFTs (for active-matrix liquid crystal displays, AMLCDs) and their cost advantage, an OLED display based on (α-Si) TFT back planes is of great commercial interest.

6.2 Pixel layout

Since the luminance of an OLED is proportional to its current and is only an indirect function of voltage, the pixel should supply a controlled current to the OLED. This is accomplished by using the simplest circuit possible, which has two TFTs (Figure 6.1).

The data voltage is written to the gate of the driving transistor (T_2) which in turn determines the current through the OLED. The programming current and storage requirements are similar to those of AMLCDs [7]. The ON current of the switching transistor (T_1) must be sufficient to write the data voltage within a row time, and the OFF current must be low enough to keep the voltage decay over a

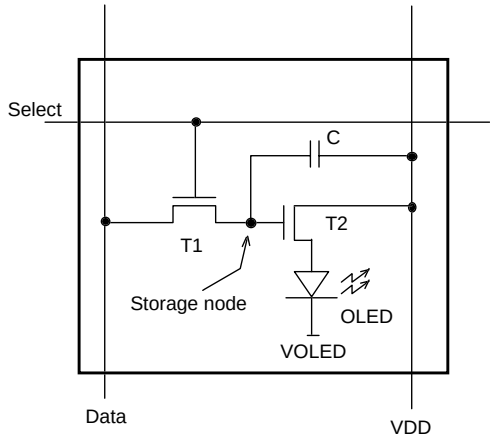

Figure 6.1: The two-transistor pixel: T_1 is the storage transistor; T_2 is the driving transistor; C is the storage capacitor.

frame time under a certain ΔV_{ON}:

$$\begin{aligned} I_{ON,T1} &> k_1\, C_{pixel}\, V_{ON}\, N/T_f \\ I_{OFF,T1} &< k_2\, \Delta V_{ON}\, C_{pixel}/T_f \end{aligned} \tag{6.1}$$

where V_{ON} is the ON voltage of the select signal; N is the number of rows; T_f is the frame time; T_f/N is the select time or row time; $C_{pixel} \simeq C_{storage}$ is the capacitance between the gate of T_2 and the V_{DD} line; the allowed voltage decay, ΔV_{ON}, is defined as the swing of V_{ON} divided by the number of gray scale levels. The constants k_1 and k_2 are taken to be 5 and 0.2, respectively. For a typical VGA display with a screen refresh rate of 60 Hz and 256 levels of gray scale, $N = 480$, $T_f = 16$ ms, $V_{ON}/\Delta V_{ON} = 256$, one arrives at the key condition $I_{ON,T1}/I_{OFF,T1} > 3 \times 10^6$, which is routinely met by α-Si TFTs for AMLCD displays. In addition, in AMOLED displays the driving transistor (T_2) must provide enough current to

drive the OLED to sufficient luminance:

$$I_{T2} = \frac{1}{2}\mu_n C_g \frac{W}{L}(V_{GS} - V_T)^2 = LA_{pixel}/\eta \tag{6.2}$$

where L in cd/m^2 is the desired areal luminance of the display, A_{pixel} is the area of the pixel, and η in cd/A is the luminous efficiency of the OLED.

The single-layer doped polymer OLED used in our experiment has a luminous efficiency of 3 cd/A in the green [8]; therefore, to achieve the benchmark of 100 cd/m^2 in areal luminance in a 250 μm $\times$ 250 μm pixel, $I_{T2} \geq 2$ μA is required.

The layout of the pixel is shown in Figure 6.2. The cell dimension is 250 μm $\times$ 250 μm; the switching transistor (T_1) which is located at the top left corner of the cell, has a W/L of 20 μm/20 μm; the driving transistor (T_2) , which is located at the top left corner of the cell, has a W/L of 80 μm/10 μm; and the area of $C_{storage}$ which is to the right of T_2 is 1500 μm^2. The OLED itself occupies 40% of the pixel area.

6.3 Experiments

The fabrication process starts with soda lime glass coated with 15 Ω /sq indium tin oxide (ITO) purchased from Applied Films Corp. After patterning the ITO, a 100 nm SiN_x:H passivation layer is deposited by plasma enhanced chemical vapor deposition (PECVD). Then α-Si TFTs are made by a back-channel-etch process (Figure 6.3) [9, 10]. First, the Ti/Pt TFT gate electrode (40/60 nm) is deposited

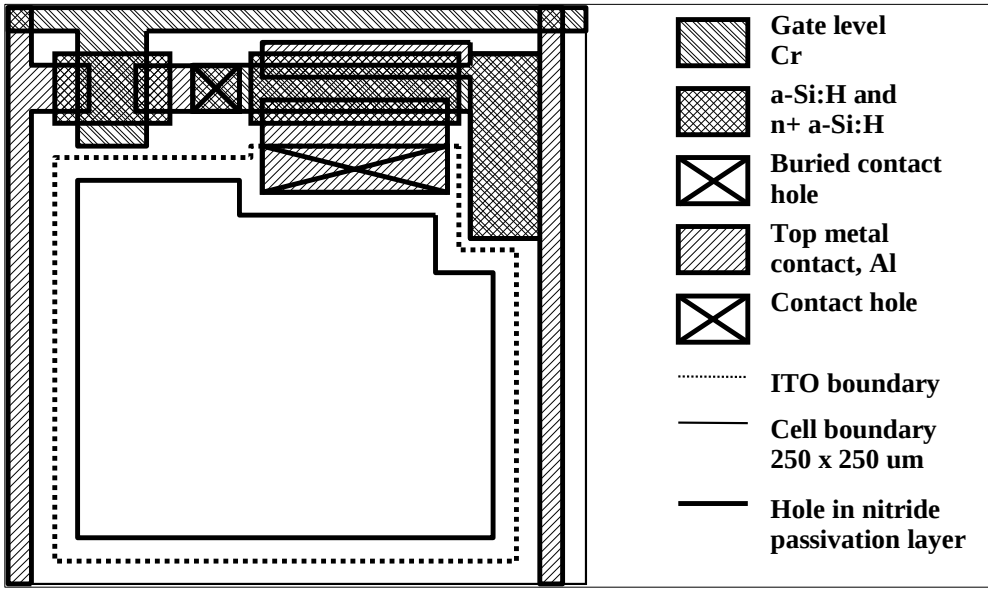

Figure 6.2: Cell layout of the two-transistor pixel.

by e-beam evaporation in a lift-off process, followed by the growth of layers of SiN_x:H (250 nm), intrinsic α-Si:H (150 nm) and n^+ α-Si:H (500 nm) in a three-chamber PECVD system in Prof. Wagner's lab at temperatures of 350°C, 250°C and 250°C respectively. The recipes for the growth of these layers is given in Table 6.1.

After defining the active α-Si:H regions and opening contact holes to the gate of T_1 and the ITO (Figure 6.1), the Al source/drain layer is evaporated and patterned. After a back-channel-etch and annealing, the TFTs are passivated by a blanket SiN_x:H film, and an OLED contact hole is opened to the ITO. The OLED used to demonstrate the operations of this pixel is a single-layer blend polymer device [8]. After treating the ITO anode with an O_2 plasma [11], a solution of

Table 6.1: Recipe for SiN_x:H, intrinsic α-Si:H, and n+ α-Si:H deposition. The units of time, pressure, rf power, temperature, and gas flow are seconds, mTorr, W, °C, and sccm, respectively.

Description	Time	Pressure	Power	Temp 1	Temp 2	Temp 3	SiH_4	NH_3	H_2
SiH_4 flush	120	500		350	350	320	13		
NH_3 flush	120	500		350	350	320	13	130	
SiNx Dep.	2250	500	3.5	350	350	320	13	130	
NH_3 flush	120	500		350	350	320	13	130	
Pause	10	5		350	350	320			
H_2 flush	5	100		350	350	320			20
H_2 flush	120	500		350	350	320			50

Description	Time	Pressure	Power	Temp 1	Temp 2	Temp 3	SiH_4	H_2
SiH_4 flush	120	500		250	250	230	50	
i-Si dep.	1080	500		250	250	230	50	
SiH_4 flush	120	500	4.5	250	250	230	50	
H_2 flush	5	500		250	250	230		10
H_2 flush	120	500		250	250	230		50

Description	Time	Pressure	Power	Temp 1	Temp 2	Temp 3	AR	SiH_4	PH_3
SiH_4 flush	60	500		260	270	200		50	
n+ flush	60	500		260	270	200		44	6
n+ Si Dep.	400	500	3.5	260	270	200		44	6
SiH_4 flush	120	500		260	270	200		50	
Ar flush	120	500		260	270	200	50		

poly(N-vinyl carbazole) / 2-(4-biphenyl)-5-(4-tert-butylphenyl)-1,3,4-oxadiazole / Coumarin 6 (PVK/PBD/C6) is spin-coated over the entire sample. Finally, a blanket Mg:Ag (10:1)/Ag cathode is thermally evaporated.

A cross-sectional diagram of T_2 and the OLED is shown in Figure 6.3. Beginning the process with ITO pre-coated substrates eliminates the need to deposit ITO (standard process temperature $\geq 350°C$) after TFT fabrication, which

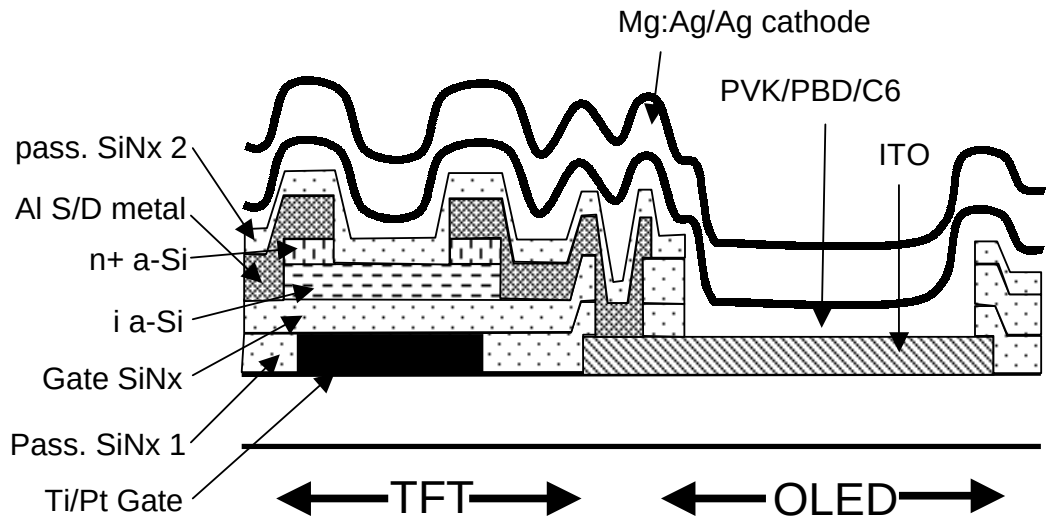

Figure 6.3: Pixel cross-section showing T_2 and the OLED.

may de-hydrogenate the TFT's. The use of Ti/Pt as TFT gates provides good contact between the Al source of of T_1 and the gate of T_2 (Figure 6.1). Initial experiments with Cr gates resulted in poor contacts to the source/drain metal because of an insulating surface metal oxide on the exposed Cr gate in the contact hole, resulting from intermediate process steps. Such a contact is not needed in AMLCD pixels.

The polymer layer deposition and loading of the sample into the evaporator were done in a dry nitrogen glove box. A solution of 100 mg PVK/40 mg PBD/0.3 mg C6 in 7.5 ml chloroform normally yields a 100-nm film on ITO-coated glass after spin-casting at 4000 rpm. However, when this solution was used to spin-cast a polymer layer over the TFT backplane, shorts between the OLED cathode and

the ITO were observed, presumably due to the topography of the backplane. To ensure yield, a solution with the same solute in only 5.5 ml chloroform was spun-cast at 4000 rpm. This solution normally yields 180 nm thick films on unpatterned substrates [12]. From the pixel EL (Figure 6.4), the emitting portion is in the central region of the actual OLED aperture (Figure 6.2). The polymer layer is expected to be much thicker near the edge due to surface tension . The side walls are up to 500 nm thick and not tapered. The drive voltage at J = 5 mA/cm^2 is 27 V *vs.* 9 V for an OLED with a 100 nm polymer layer. Assuming linear scaling of voltage with film thickness, the nominal thickness of the polymer layer in the emitting region is 300 nm.

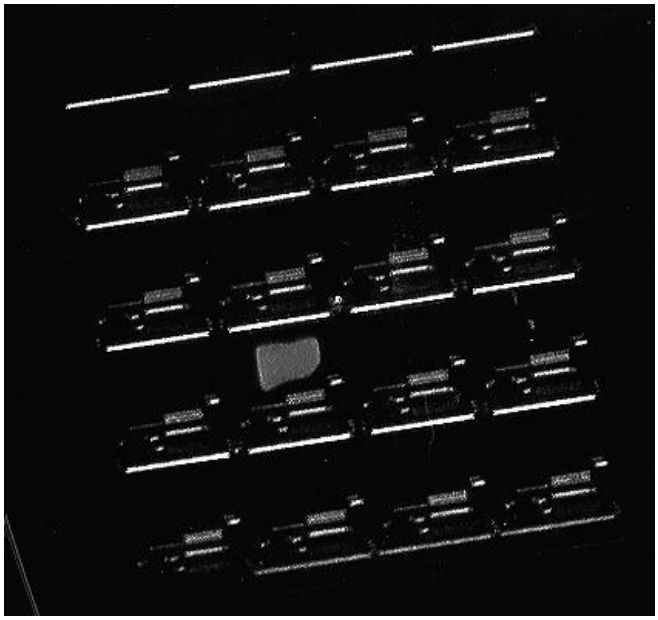

Figure 6.4: Optical micrograph of a 4x4 AMOLED array with one lit pixel.

6.4 Data and discussion

An optical micrograph of the pixel after passivation and before OLED integration is show in Figure 6.5. The TFT transfer characteristics is measured at this juncture (Figure 6.6).

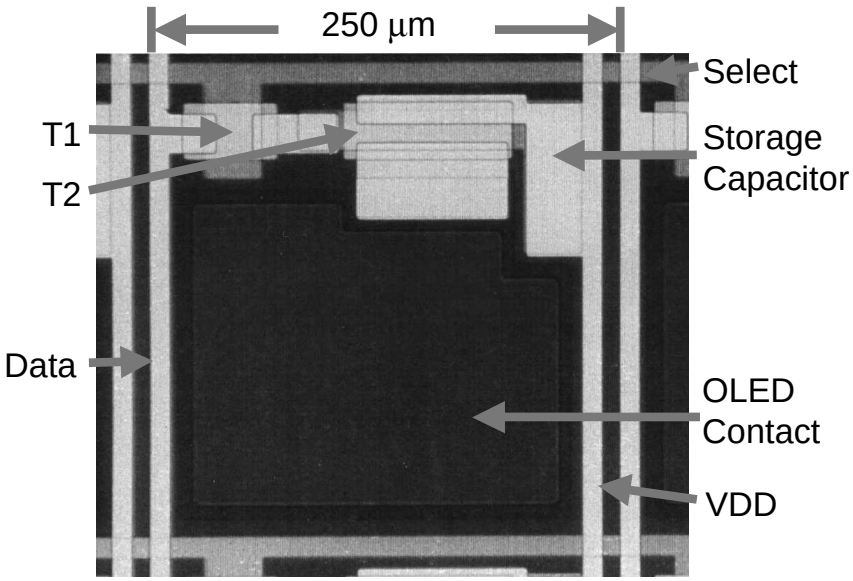

Figure 6.5: Optical micrograph of the pixel after passivation, before OLED integration. The cathode of the OLED will serve as the ground.

The average saturation region mobility (μ_n) is 0.5 cm^2/Vs; the threshold voltage (V_T) is 2.5 - 3 V. The I_{ON}/I_{OFF} ratio is around 5×10^6, so the aforementioned on/off current ratio for T_1 is satisfied. To reach a current of 2 μA in T_2, the over-drive voltage, $V_{OD} = V_{GS} - V_T$, needs to be 8 V, which is within the operation range for TFTs in AMLCD displays.

After evaporation of the OLED cathode, a ring of high vacuum grease (Var-

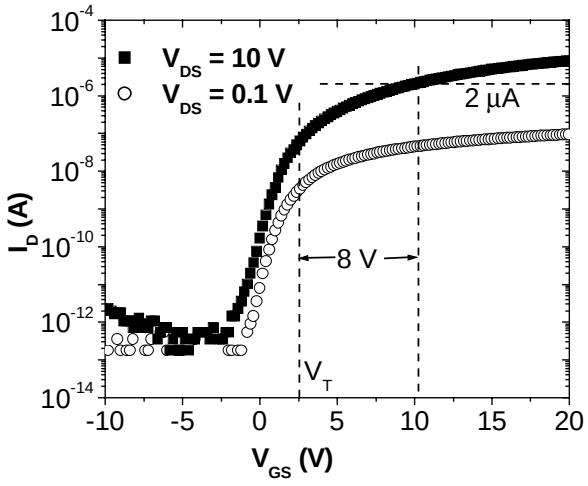

Figure 6.6: TFT transfer characteristics: W/L = 80 μm/10 μm, measured after passivation, before OLED integration.

ian) was drawn around the devices and a cover slide is place on top inside the dry nitrogen glove box to provide temporary encapsulation. Electrical measurements were performed at a probe station in air. The pixel is driven with data (V_{data}) and select signal wave forms consistent with VGA timing, along with $V_{DD} = 25$ V and $V_{OLED} = -10$ V. The frame time (T_f) is 16 ms, and the row time (T_r) is 33 μs, compatible with the video rate for a display with 480 rows. Both data and select signals vary from 0 to 30 V, which will bring the TFT into saturation for gate voltages up to $V_{DD} - V_T$, or about 27 V.

The resultant pixel luminance *vs.* data is plotted in Figure 6.7. Some leakage current at low data voltages indicates that the TFT in the measured pixel did not have as good off-state characteristics as shown in Figure 6.6. Video brightness (100

cd/m^2 areal luminance) is achieved at a data voltage of 30 V.

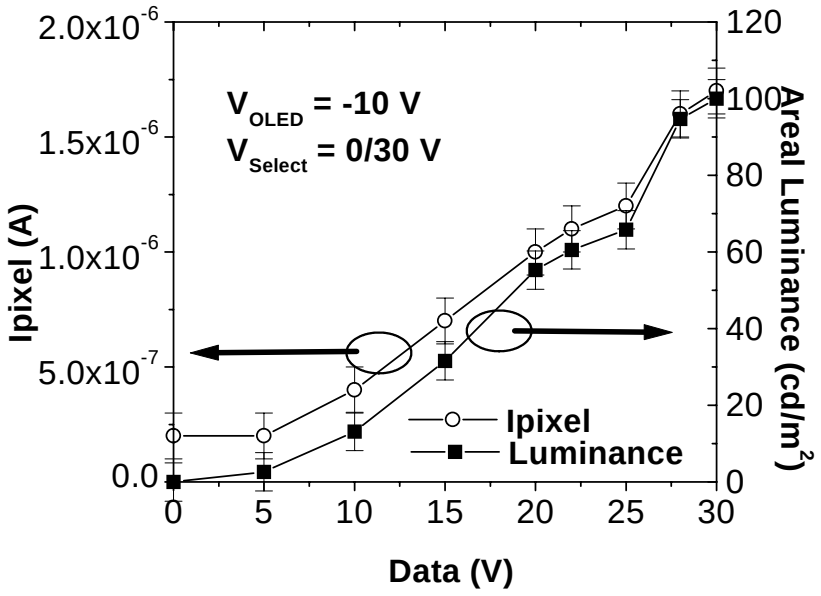

Figure 6.7: Pixel luminance as a function of data voltage, $V_{DD} = 25$ V, $V_{OLED} = -10$ V, Select = 30 V with VGA signal timing.

The data voltage swing of ~ 30 V required to reach ~ 2 μA of pixel current is substantially greater than the 11 V swing one would expect from $V_{OD} = 8$ V (shown in Figure 6.6) plus $V_T \sim 3$ V. This is because the fabrication process connects the OLED anode (ITO) to the TFT (Figure 6.8a); therefore, V_{data} is the sum of OLED voltage and the gate-to-source voltage of T_2, resulting in the high swing for V_{data} [13]. We would prefer a p-channel device, so that the swing on the gate of T_2 would only be its gate-to-source voltage, since in this case the source will be the more positive terminal of T_2 [6]. However, p-channel devices are not available in α-Si technology, due to exceedingly low hole mobilities.

A more desirable configuration would be to connect the OLED cathode

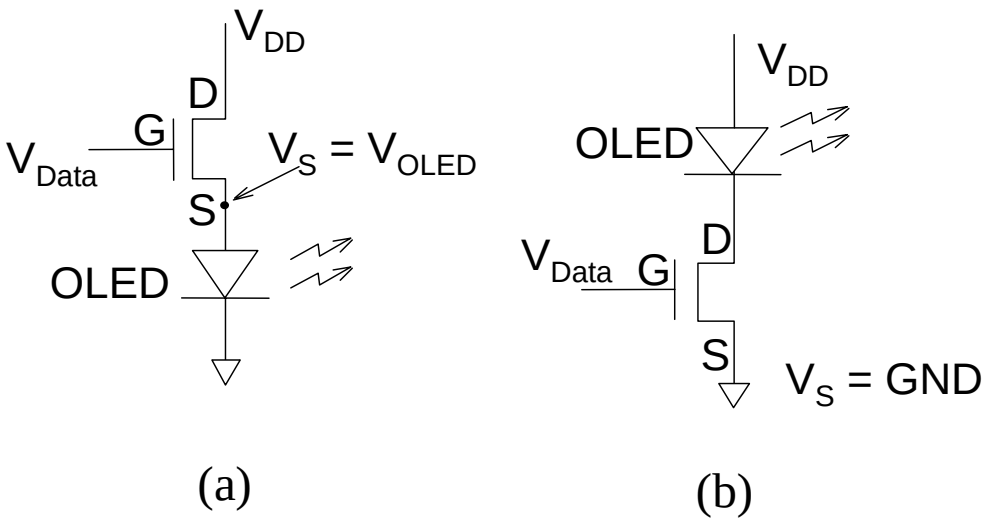

Figure 6.8: (a) The source of the TFT is connected to the anode of the OLED. V_{gs} depends on V_{OLED}. (b) The drain of the TFT is connected to the cathode of the OLED. V_{gs} is independent of the OLED characteristics.

to T_2, so that the source of T_2 is connected to ground (Figure 6.8b). One can predict how the required gate swing for T_2 will vary with TFT geometry and OLED efficiency in this situation. To keep the TFT in saturation, so that the current is independent of small variations in OLED characteristics, V_{DS} should be held greater than the largest $V_{GS} - V_T$. The corresponding V_{data} swing is shown in Figure 6.9, and in a realistic system with a W/L of 20 and an OLED luminous efficiency of 12 cd/A [14], the V_{data} swing can be less than 3 V. In addition to being power efficient, a low V_{data} swing helps to reduce TFT threshold voltage drift [16]. Such threshold voltage variations can be corrected by more complicated pixel designs [6]. Realizing such an optimal configuration will require either an inverted OLED with anode on top [15, 17], or a patterned top contact. Several

groups have demonstrated such cathode patterning although it has not yet been integrated with transistors [18, 19].

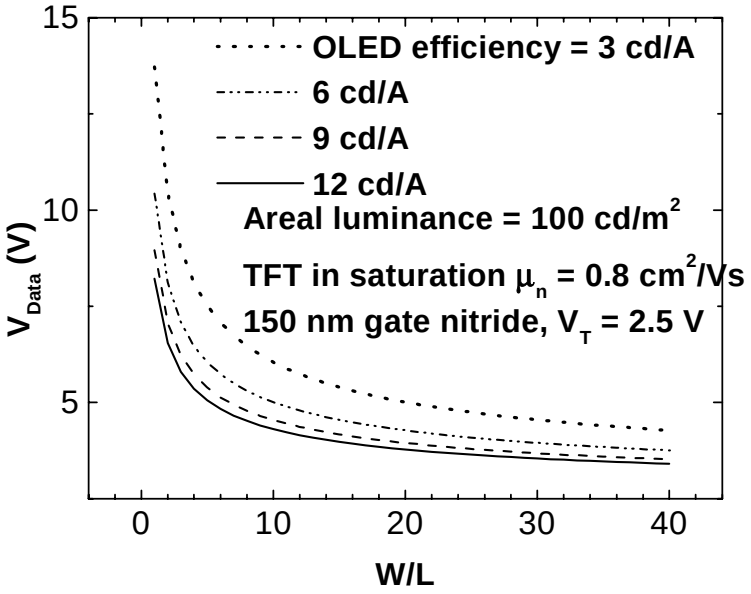

Figure 6.9: V_{data} swing ($= V_{GS} - V_T$) as a function of transistor W/L ratio for four OLED luminous efficiencies. Assumptions are: areal luminance = 100 cd/m^2, TFT in saturation, $\mu_n = 0.8$ cm^2/Vs, 150 nm gate nitride.

6.5 Conclusions

In summary, an AMOLED pixel based on α-Si TFTs that achieves 100 cd/m^2 in areal luminance was fabricated. To realize lower data voltage swings, it will be necessary to use more complicated circuits or inverted OLEDs so that cathode contacts to the TFT can be realized, or a p-channel TFT must be employed to drive the OLED. A data voltage swing under 3 V, which minimizes the power dissipation required to keep the driving TFT in saturation, should be feasible.

This work was done in 1998, and other groups have investigated amorphous silicon TFT based AMOLEDs since then. A circuit simulation demonstrated the feasibility of amorphous silicon TFT based backplane for highly efficient phosphorescent OLEDs [20]. Recently, a current-programmable amorphous silicon TFT based AMOLED pixel was reported [21]. It utilizes four transistors to correct for the drift of the TFT threshold voltage.

References

[1] C. W. Tang and S. A. VanSlyke, *Appl. Phys. Lett.* **51**, 913 (1987).

[2] J. H. Burroughes, D. D. C. Bradley, A. R. Brown, R. N. Marks, K, Mackay, R. H. Friend, P. L. Burns, and A. B. Holmes, *Nature* **347**, 539 (1990).

[3] Y. Sato and H. Kanai, *Mol. Cryst. Liq. Cryst.* **253**, 143 (1994).

[4] M. T. Bernius, M. Inbasekaran, J. O'Brien, and W. Wu, *Adv. Matt.* **12**, 1737 (2000).

[5] T. Shimoda, M. Kimura, S. Miyashita, R. H. Friend, J. H. Burroughes, and C. R. Towns, *SID Dig.*, 372 (1999).

[6] R. M. A. Dawson, Z. Shen, D.A. Furst, S. Connor, J. Hsu, M.G. Kane. R. G. Stewart, A. Ipri, C. N. King, P. J. Geen, R. T. Flegal, S. Pearson, W. A. Barrow, E. Dickey, K. Ping, S. Robinson, C. W. Tang, S. Van Slyke, F. Chen, J. Shi, M. H. Lu, M. Moskewicz, and J. C. Sturm, *SID Dig.*, 438 (1999).

[7] J. Kanicki, *Flat Panel Display Materials*, MRS Spring Meeting Tutorial, Material Research Society, San Francisco, CA, (1996).

[8] C. C. Wu, J. C. Sturm, R. A Register, J. Tian, E. P. Dana, and M. E. Thompson, *IEEE Trans. Elec. Dev.* **44**, 1269 (1997).

[9] E. Y. Ma, (Ph.D. thesis, Dept. of Elec. Eng., Princeton University, 1998).

[10] C. van Berkel, "Amorphous-Silicon Thin-Film Transistors: Physics and Properties", in Ed. J. Kanicki, *Amorphous and Microcrystalline Semiconductor Devices*, vol. II (Artech House, Boston, 1992).

[11] C. C. Wu, C. I. Wu, J. C. Sturm and A. Kahn, *Appl. Phys. Lett.* **70** 1348 (1997).

[12] C.-C. Wu, *Light-Emitting Devices Based on Doped Polymer Thin Films*, (Ph.D Thesis, Elec. Eng., Princeton Univ., 1997).

[13] C. C. Wu, S. D. Theiss, G. Gu, M. H. Lu, J. C. Sturm, S. Wagner and S. R. Forest, *IEEE Elec. Dev. Lett.* **18**, 609 (1997).

[14] J. Kido and Y. Iizumi, *Appl. Phys. Lett.* **73**, 2721 (1998).

[15] D. R. Baigent, R. N. Marks, N. C. Greenham, R. H. Friend, S. C. Moratti and A. B. Holmes, *Appl. Phys. Lett.* **65**, 2636 (1994).

[16] M. J. Powell, C. van Berkel and J. R. Hughes, *Appl. Phys. Lett.* **54**, 1323 (1989).

[17] V. Bulović, P. Tian, P. E. Burrows, M. R. Gokhale, S. R. Forrest and M. E. Thomson, *Appl. Phys. Lett.* **70** 2954 (1997).

[18] C. C. Wu, J. C. Sturm, R. A. Register and M. E. Thompson, *Appl. Phys. Lett.*, **69**, 3117 (1996).

[19] P. F. Tian, P. E. Burrows and S. R. Forrest, *Appl. Phys. Lett.* **71**, 3197 (1997).

[20] M. Hack, J. J. Brown, J. K. Mahon, R. Kwong, R. Hewitt, *Proc. 1st Int. Disp. Man. Conf.*, Seoul, Korea, Sept. 5-7, 2000.

[21] Y. He, R. Hattori, and J. Kanicki, *Jpn. J. Appl. Phys.* **40**, Pt.1, 1199 (2001).

Chapter 7

OLEDs with Lithographically Patterned Aluminum Cathodes, and OLED Process Tolerances

---

7.1 Introduction

The organic materials used in OLEDs are extremely susceptible to water, oxygen and organic solvents [1]-[5]. For this reason, direct patterning of OLEDs has generally been avoided. Instead, two approaches, each with its own advantages and disadvantages, are widely employed. For small molecule devices, shadow-masked deposition, either with a movable, metal shadow mask or an integrated shadow mask made of photoresist has been adopted [6, 7]. For polymer OLEDs, ink-jet deposition has been demonstrated as a viable approach [8]. Prototypes 2–3 inches in diagonal from both technologies have been demonstrated [9, 10]. However, an integrated shadow mask cannot produce full-color displays, and there are techno-

logical hurdles to overcome before a movable shadow mask can be used to produce large displays. As for the ink-jet approach, the control of droplet size and morphology of the deposited film requires surface patterning and plasma treatment which increases production complexity and cost [10]. For these reasons, it is worthwhile to explore lithographic patterning of OLEDs.

Direct photolithography has been attempted on thermally-converted PPV films [11]. (The PPV used in earlier work is insoluble in most solvents, and a precursor is spun-cast before being thermally converted into PPV [12].) Thermally-converted PPV is extremely rugged, so the results cannot be applied to the more commonly used small molecule and polymer compounds. Tian et al. also patterned OLEDs by angled deposition into patterned wells which were lithographically patterned before the organic deposition [13]. F. Pschenitzka et al. first demonstrated Al cathodes patterned by conventional photolithography performed directly on the OLEDs [14], which is improved upon in this work. Furthermore, the tolerance of OLEDs for traditional semiconductor processing, such as reactive-ion-etching is also explored.

7.2 Lithographically patterned and dry etched cathodes

The OLEDs used to demonstrate cathode patterning are single-layer PVK/PBD/C6 devices with Al cathodes [17, 18]. PVK/PBD/C6 films are spin-cast onto oxygen-plasma-treated ITO-coated glass substrates [19]. The cathode is evaporated through shadow masks for control devices, or in a blanket layer to be patterned and etched. Three types of devices are fabricated: 1) ITO/120 nm PVK/PBD/C6 /80 nm Mg:Ag/120 nm Ag/210 nm Al, 2) ITO/120 nm PVK/PBD/C6 /200 nm Al, and 3) ITO/120 nm PVK/PBD/C6/300 nm Al. Only the pure Al cathodes are lithographically patterned and dry etched.

No special treatment is performed on OLEDs with blanket Al cathodes; however, the selection of a proper photoresist and developer is the key to preventing Al delamination from the underlying cathode layer (blistering). The process sequence is as follows:

- 25 min, 90°C oven pre-bake
- Spin on AZ5214IR at 7000 RPM
- 50 s, 95°C hot plate bake
- 15 s exposure with mask
- 65 s, 115°C second bake

- 60 s flood exposure
- Develop in AZ312MIF:DI (1:1), 20 s

A thin image reversal photoresist, AZ5214IR, was chosen for its low process temperature requirements. The pre-bake is necessary to promote adhesion between the photoresist and the Al cathode. The developer AZ312MIF is formulated for metal-oxide-semiconductor transistor processes and attacks Al much more slowly than potassium or sodium hydroxide based developers. Blistering is caused by the developer attacking and forming pinholes in Al during the development process, and it was avoided previously by evaporating Al twice [15].

The Al cathode is etched by a boron trichloride/chlorine (BCl_3/Cl_2) plasma in a Plasma Technology reactive-ion etcher [20]-[23]. The plasma conditions used in these experiments are:

O_2 plasma: 25 sccm O_2, 100 mTorr, 100 W

Cl_2 plasma: 20 sccm Cl_2, 100 sccm Ar, 150 mTorr, 50 W

Al etch: 10 sccm Cl_2, 20 sccm BCl_3, 30 mTorr, 175 W, 95 s

PR strip: O_2 plasma: 25 sccm O_2, 100 mTorr, 140 W, 4 min followed by Ar plasma 25 sccm Ar, 30 mTorr, 140 W, 1 min

The O_2 and Cl_2 plasmas are used only to explore the process tolerances of OLEDs, not to etch Al cathodes. Cl radicals etch pure Al very rapidly [22],

$$Al + Cl \rightarrow AlCl(\uparrow) \tag{7.1}$$

However, Cl_2 does not etch the native oxide on Al. The removal of the native aluminum oxide (Al_2O_3), which is usually referred to as initiation, is accomplished by adding BCl_3 or CCl_4 to the gas mixture [20].

20 μm lines with 20 μm spacings are used as testing patterns for optimizing plasma conditions. Because Cl radicals etch Al isotropically and rapidly but only BCl_3 derived radicals etch Al_2O_3, the ratio of BCl_3 and Cl_2 flow rates is critical for line shape control (Figure 7.1a-d). Jagged edges are clearly visible when BCl_3:Cl_2 = 1:1 (Figure 7.1a, b). The situation is much improved when the ratio is increased to 2:1 (Figure 7.1c), and seems starting to worsen again when the ratio is increased to 4:1 (Figure 7.1d). Based on these results the BCl_3:Cl_2 ratio is set to 2:1.

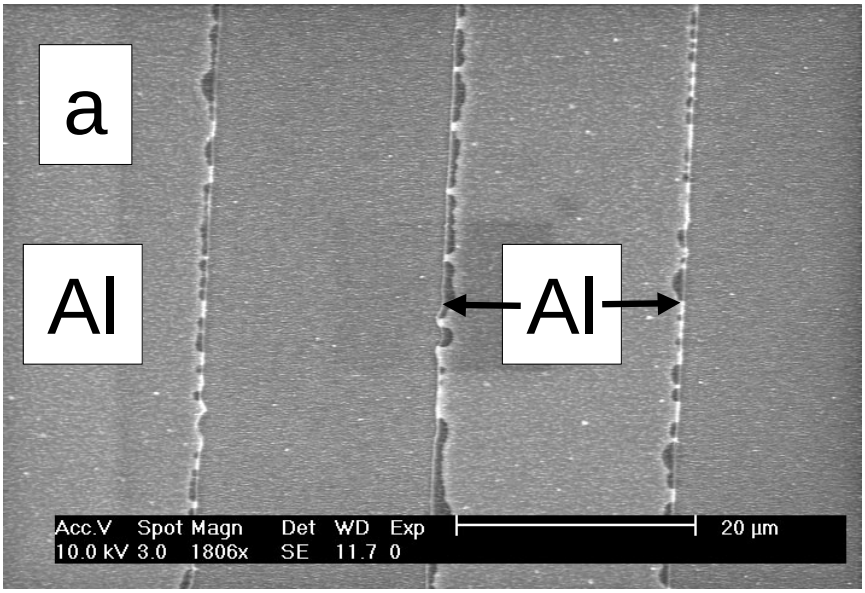
a
Al
Al
Acc.V Spot Magn Det WD Exp
10.0 kV 3.0 1806x SE 11.7 0
20 µm

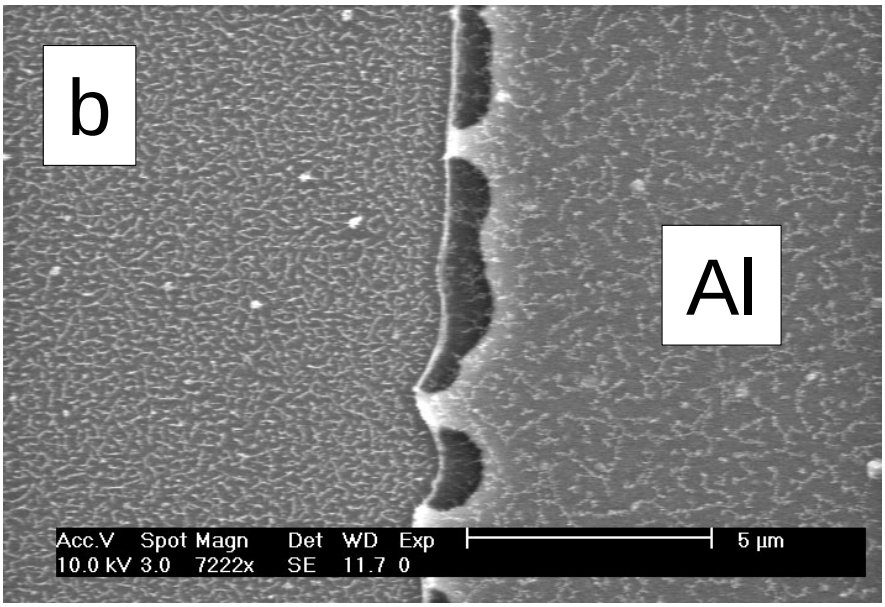
b
Al
Acc.V Spot Magn Det WD Exp
10.0 kV 3.0 7222x SE 11.7 0
5 µm

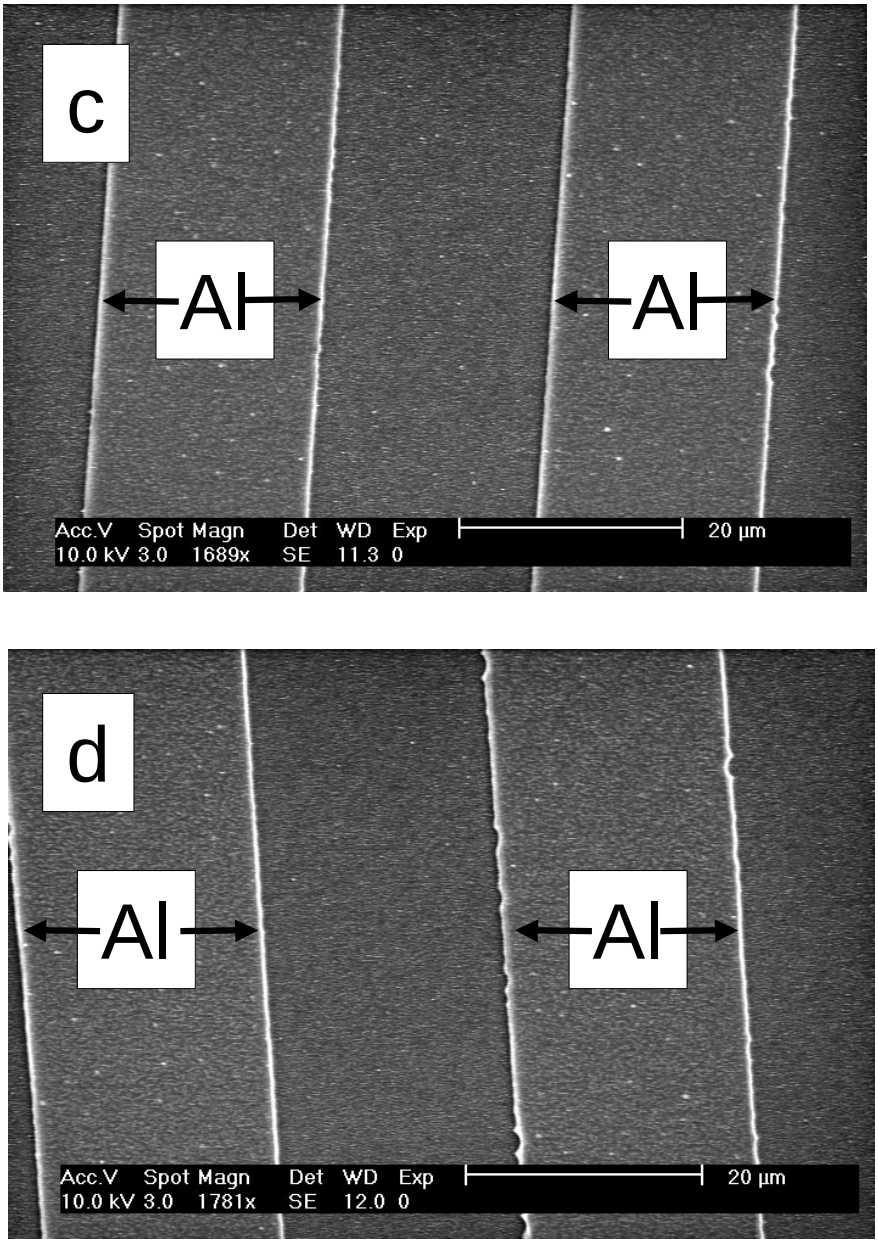

Figure 7.1: Line shape dependence on BCl_3:Cl_2 ratio: (a) BCl_3:Cl_2 = 1:1, (b) same as (a), high magnification, (c) BCl_3:Cl_2 = 2:1, (d) BCl_3:Cl_2 = 4:1. The white, gnarly structure on both the etched and unetched part is a residue of the etching process.

The photoresist that defines the line features is stripped with a two-step process of O_2 plasma ashing and Ar plasma sputtering. However, residue is left in both etched and unetched areas (Figure 7.1). The residues are not known, but are most likely a redeposited polymer consisting of chlorinated photoresist [16] . Because of the residues, the cathode cannot be contacted with a thin gold wire [17], but a more rigid wire (e.g. a stripped 26 gauge wire) had to be used. Figure 7.2 compares the characteristics of a control device where the Al cathode is evaporated through a shadow mask with a 1-mm diameter opening with an etched device where the same shadow mask is used in an image reversal photolithography process. The structure for both devices is ITO/120 nm PVK/PBD/C6/300 nm Al. Due to the contact difficulties, the etched device is measured outside of the glovebox and its luminance values are not available. But the EL is of the same intensity as from the control device at given drive currents as judged by eye. The drive voltage (as indicated by the solid line in Figure 7.2) is approximately 1.8 V higher than that of the control device (as indicated by the solid squares). It is unclear whether this increase is due to the etching process or from baking during the photolithography.

7.3 OLED process tolerances

The knowledge of the tolerance of OLEDs to standard semiconductor processes is of great value not only for dry-etch patterning of OLEDs, but also to OLED

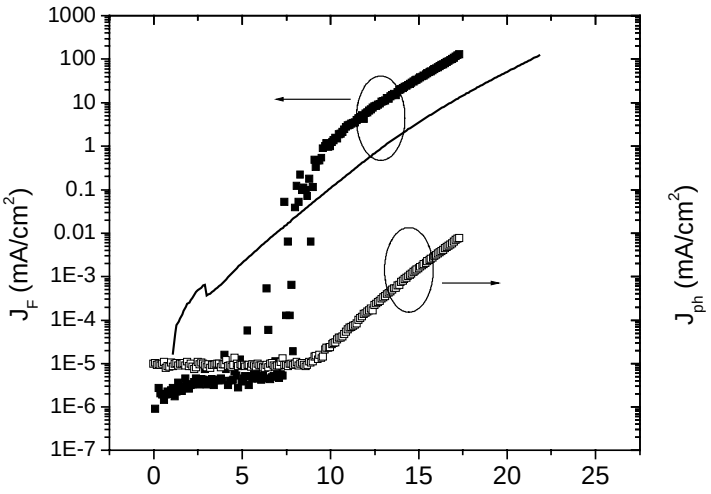

Figure 7.2: L–J–V of an control device and J–V of an etched OLED. Solid and open squares: forward and luminescence photo current density of the control device (patterned by cathode evaporation through a shadow mask); solid line: forward current density of the etched device, cathode size = 1 mm diameter, OLED structure: ITO/120 nm PVK/PBD/C6/300 nm Al.

reliability and degradation in general. As the OLEDs degrade in room air, a non-emissive region is formed around the edge of the device which we call the "edge dark zone", or the middle of the device which is commonly referred to as the "dark spots" [1]-[5]. Water or oxygen-induced cathode delamination is thought to be the main culprit, the other being moisture-induced crystallization [3]. Indeed, exposure to reactive agents, be they water, oxygen or other radicals, is the main cause of concern for applying traditional semiconductor processing to OLEDs. Therefore, the growth of these non-emissive zones is a good measure of OLEDs'

tolerance of various processing techniques. With the dry-etching of OLED cathodes in mind, the growth of edge dark zones for OLEDs exposed to various plasmas is investigated. The edge emission zones are preferred over the dark spots due to ease of measurement.

Type 1–3 OLEDs (see section 7.2) with cathodes evaporated through a shadow mask and type 3 OLEDs with etched cathodes are fabricated. All cathodes are circular and 1 mm in diameter. All devices are exposed to room air after the cathodes are deposited. Those devices which have shadow-mask-defined cathodes and are not exposed to any plasmas are referred to as control devices. Other devices with shadow-mask defined cathodes are exposed to O_2 or Cl_2 plasma for various amounts of time. Periodically, devices are driven at a current density of 10 mA/cm^2, and optical micrographs of the EL are taken, from which the width of the edge dark zone, ΔL, is measured. In between measurements, the devices are stored in room air.

A series of optical micrographs illustrating the growth of the edge dark zone with time from a type 1 control device is shown in Figure 7.3.

Figure 7.4 shows the growth of the edge dark zone in an control and an etched type 3 device. The relative humidity of the ambient during this measurement is approximately 50%. Within the measurement error, the growth of the edge dark zone is the same in both samples , indicating that the dry etching does not appreciably hasten degradation of devices stored in room air. It is unknown

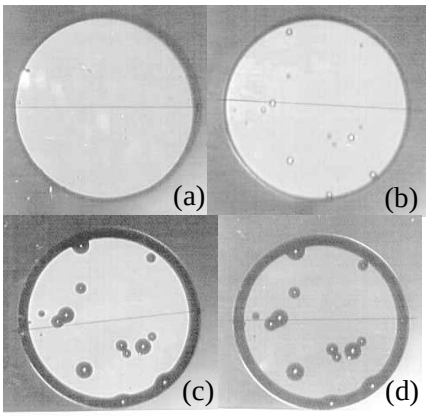

Figure 7.3: Electroluminescence micrographs of devices with Mg:Ag/Ag/Al cathodes (type 1) exposed to oxygen plasma for 4 min. The width of the non-emissive zone was a) 20 μm after 11 min exposure to air, b) 23 μm after one hour, c) 55 μm after 12 hours, and d) 60 μm after 15 hours.

whether the same holds true for packaged devices.

Figure 7.5 shows the growth of the dark zone for type 1 and 2 devices that are exposed to different plasmas for various durations. These plasma treatments do not etch the cathode. In between measurements, the samples are stored in room air that has a relative humidity of approximately 25%. From the plot, it is clear that with devices of the same cathode material, exposure to either O_2 or Cl_2 plasma does not change the growth of the edge dark zone. However, the edge dark zone grows much slowly in the devices with the Mg:Ag/Al cathodes. The growth of the edge dark zone is drastically reduced if the devices are stored in dry nitrogen. Comparing the edge dark zone growth rate for devices with Al cathodes in Figures 7.4 and 7.5, it can be seen that high ambient humidity induced a faster rate of dark zone growth, leading one to conclude that water, rather than oxygen,

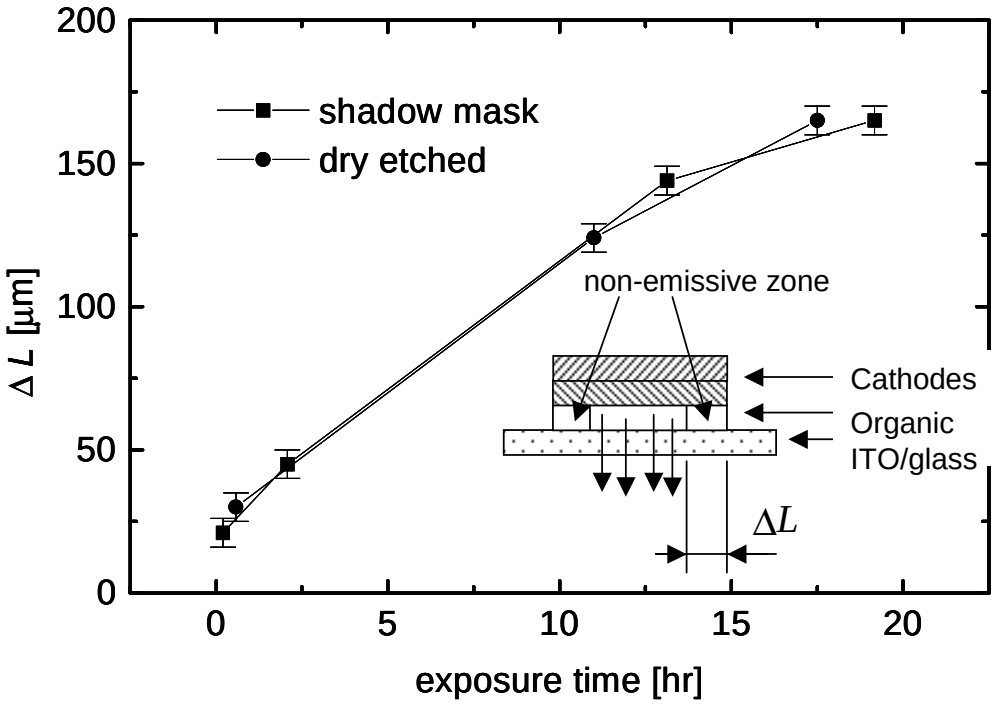

Figure 7.4: Growth of the edge dark zone with time in air (~50% relative humidity) after (a) aluminum cathode (300 nm) patterning with plasma etching (circles), and (b) patterned cathode formation by aluminum evaporation through a shadow mask (squares). ΔL is the width of the non-emissive zone (inset). (From Ref. ??)

is responsible for creating the non-emissive regions.

Similar ΔL *vs.* t curves are reported by McElvain et al. who measured the size of the dark sports *vs.* time [2]. The ΔL *vs.* t curves for the control samples in Figure 7.5 can be fitted to a square root of t equation of the form $\Delta L = \Delta L_0 + \sqrt{Dt}$:

$$\begin{aligned} \text{Mg:Ag/Ag/Al cathodes} \quad \Delta L(\mu\text{m}) &= 12.69 + 12.47\sqrt{t(\text{hr})} \\ \text{Al cathodes} \quad \Delta L(\mu\text{m}) &= 1.62 + 21.02\sqrt{t(\text{hr})} \end{aligned} \tag{7.2}$$

The large ΔL_0 value of the devices with Mg:Ag/Ag/Al cathodes is presumably due to the fact that Mg and Ag are co-evaporated, and the difference in the boat-

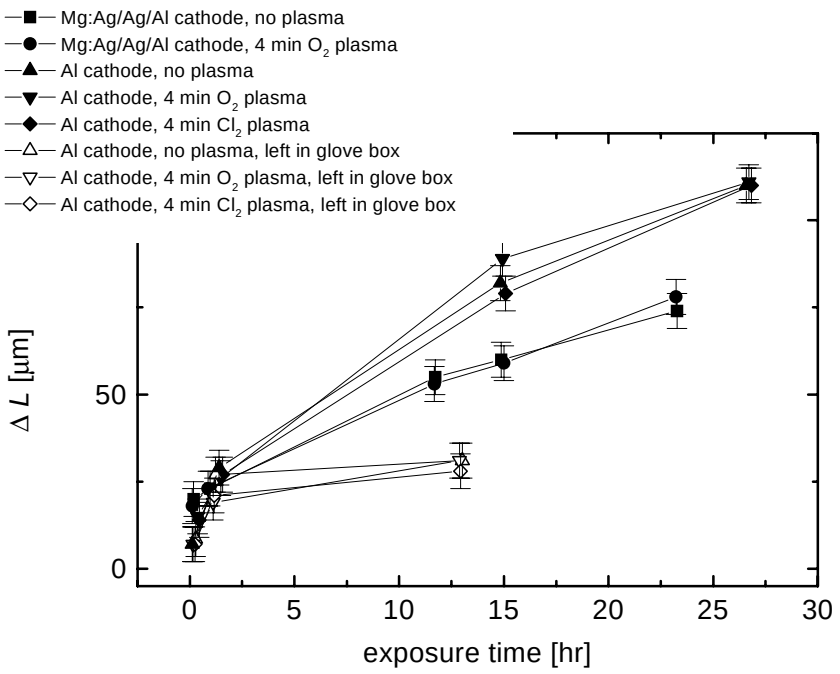

Figure 7.5: Growth of the non-emissive zone vs. exposure time to air for cathodes of different material and processing steps after cathode deposition. All cathodes were deposited using a shadow mask. (From Ref. **??**)

to-target angles resulted in some initial non-uniformity near device edge. The standard deviations (1.83 μm and 2.26 μm, respectively) are fairly small, so the growth of the dark zone is well described by the square root of t dependence characteristic of diffusion limited reactions. A simple test for adhesion among multiple layers of thin films is the Scotch tape test, where a Scotch tape is applied to the surface of the top layer and peeled off — the interface with the weakest adhesion is between the layers that are peeled off by the tape and those that remain. Such tests have revealed that the cathodes are delaminated from the organic material in the non-emissive regions [2, 4]. This data supports the theory

that water reacts with the cathode metal at the cathode/organic interface and causes the cathode to delaminate. The reaction is limited by the diffusion of water along that interface and is unaffected by exposing the OLEDs to O_2 or Cl_2 plasmas.

7.4 Conclusions

The photolithographic process performed directly on large OLEDs with blanket Al cathodes is improved by selecting the AZ5214IR photoresist and the AZ312MIF developer. The BCl_3/Cl_2 ratio for optimal line shape control in Al dry etching is determined to be 2:1. Working OLEDs with lithographically patterned and dry etched cathodes are obtained. OLED degradation is shown not to be affected by exposure to O_2 and Cl_2 plasmas by measuring the growth of the edge dark zones.

References

[1] P. E. Burrows, V. Bulovic, S. R. Forrest, L. S. Sapochak, D. M. McCarty, and M. E. Thompson, *Appl. Phys. Lett.* **65**, 2922 (1994).

[2] J. McElvain, H. Antoniadis, M. R. Hueschen, J. N. Miller, D. M. Roitman, J. R. Sheats, and R. L. Moon, *J. Appl. Phys.* **80**, 6002 (1996).

[3] H. Aziz, Z. Popovic, S. Xie, A.-M. Hor, N.-X. Hu, C. Tripp, and G. Xu, *Appl. Phys. Lett.* **72**, 756 (1998).

[4] H. Aziz, Z. Popovic, C. P. Tripp, N.-X. Hu, A.-M. Hor, and G. Xu, *Appl. Phys. Lett.* **72**, 2642 (1998).

[5] A. Berntsen, P. van de Weijer, Y. Croonen, C. Liedenbaum, and J. Vleggar, *Soc. Info. Disp. Symp. Proc.*, F-28 (1997).

[6] T. Tohma, *Soc. Info. Disp. Symp. Dig.*, F-1 (1997).

[7] K. Utsugi, M. Tamegai, and E. Hasegawa, *SID Dig.*, 640 (2000).

[8] T. R. Hebner, C. C. Wu, D. Marcy, M. H. Lu, and J. C. Sturm, *Appl. Phys. Lett.* **72**, 519 (1998).

[9] G. Rajeswaran, M. Itoh, M. Boroson, S. Barry, T. K. Hatwar, K. B. Kahen, K. Yoneda, R. Yokoyama, T. Yamada, N. Komiya, H, Kanno, and H. Takahashi, *Soc. Info. Disp. Symp. Dig.*, 974 (2000).

[10] T. Shimoda, S. Kanbe, H. Kobayashi, S. Seki, H. Kiguchi, I. Yudasaka, M. Kimura., S. Miyashita, R. H. Friend, J. H. Burroughes, C. R. Towns, *SID Dig.*, 376 (1999).

[11] D. G. Lidzey, M. A. Pate, M. S. Weaver et al., *Synth. Met.* **82**, 141 (1996).

[12] J. H. Burroughes, D. D. C. Bradley, A. R. Brown, R. N. Marks, K, Mackay, R. H. Friend, P. L. Burns, and A. B. Holmes, *Nature* **347**, 539 (1990).

[13] P. F. Tian, P. E. Burrows and S. R. Forrest, *Appl. Phys. Lett.* **71**, 3197 (1997).

[14] F. Pschenitzka, Spring Meeting, Mat. Res. Soc., San Francisco, CA (1998).

[15] F. Pschenitzka, M.-H. Lu, and J. C. Sturm, *SID Dig.*, 731 (2001).

[16] W.-Y. Lee, J. M. Eldridge, and G. C. Schwartz, *J. Appl. Phys.* **52**, 2994 (1981).

[17] C.-C. Wu, *Light-Emitting Devices Based on Doped Polymer Thin Films*, (Ph.D Thesis, Elec. Eng., Princeton Univ., 1997).

[18] C. C. Wu, J. C. Sturm, R. A Register, J. Tian, E. P. Dana, and M. E. Thompson, *IEEE Trans. Elec. Dev.* **44**, 1269 (1997).

[19] C. C. Wu, C. I. Wu, J. C. Sturm and A. Kahn, *Appl. Phys. Lett.* **70** 1348 (1997).

[20] G. C. Schwartz, in *Proc. of the 5th Plasma Processing*, eds. G. S. Mathad, G. C. Schwartz, and G. Smolinsky, *Electrochemical Soc. Proc.*, 85-1 (1985).

[21] T. Mizutani, H. Komatsu, and S. Harada, *Int. Elec. Dev. Meeting Tech. Dig.*, 582 (1981).

[22] K. Tokunaga, F. C. Redeker, D. A. Danner, and D. W. Hess, *J. Electrochem. Soc.* **128**, 851 (1981).

[23] T. Banjo, M. Tsuchihashi, M. Hanazaki, M. Tuda, and K. Ono, *Jpn. J. Appl. Phys.* **36**, 4824 (1997).

Chapter 8

Conclusions and Future Work

The majority of this thesis is devoted to the light emission in OLEDs after the appropriate excitons have been formed. A combined classical and quantum mechanical microcavity (CCQMM) theory was used to describe the recombination of said excitons. Light emission into various modes as a function of emission zone to cathode distance, thickness of the ITO anode, index of the substrate were calculated with the CCQMM model and verified by experiments. The computed far-field and edge emissions were found to be in good agreement with empirical data. Cathode effects in the OLED through dipole-cathode energy transfer was examined through the model. Another major portion of the experimental work deals with shape-substrates as a means to increase the external coupling efficiency. The increase in the total external emission by a factor of 2.3 for an OLED on shaped high-index-of-refraction substrate is the highest increase in external efficiency by substrate patterning reported to date. The CCQMM model accurately predicted

the amount of increase from the shaped substrates as well.

Recently, Hung et al. reported an OLED featuring the structure ITO/NPD (75 nm)/Alq_3 (35 nm) /LiF (0.3 nm)/Al (0.6 nm)/CuPc (40 nm) /Mg:Ag where the electron injection is from the optically transparent LiF/Al layer [1]. The CuPc layer which has higher electron mobility than the Alq_3 serves as a conductive spacer between the Mg:Ag layer and the thin LiF/Al layer. Consequently, the carrier transport is decoupled from the external coupling and microcavity effects; therefore, the device enjoys the low drive voltage indicative of an OLED with a thin Alq_3 layer and a high external efficiency indicative of an OLED whose emission zone is located optimally ($\sim$77 nm for Alq_3) from the opaque metal cathode. The use of a more transparent replacement for CuPc and further optimization for carrier balance in the OLED is sure to lead to a higher efficiency device with low drive voltage.

An active-matrix OLED display pixel based on amorphous silicon TFTs was fabricated and driven to video brightness (100 cd/m^2) at video rates. Recent efforts in the display industry revolves around low-temperature polysilicon (LTPS) TFT technology due to the instability in the threshold voltage of amorphous silicon TFTs [2, 3, 4]. However, LTPS TFTs are plagued by initial threshold and mobility non-uniformities due to variations in the silicon grain structures. High-efficiency OLEDs require less current which place less stress on the driving TFTs, thus slowing down the threshold voltage drift in amorphous silicon TFTs. This

combined with its inherent cost advantage puts amorphous silicon TFT technology in the running still.

OLEDs with lithographically-patterned and dry-etched aluminum cathodes were demonstrated. Exposure to both oxygen and chlorine plasmas were found not to affect the rate of growth of the edge dark ring in OLEDs. Complete removal of photoresist after aluminum etching remain a processing challenge, which if solved, may make patterning OLEDs by conventional lithography feasible. The current method of choice for patterning for full-color OLED displays seem to be shifted-shadow-mask deposition for small molecule OLEDs and ink jet printing for polymer OLEDs [4, 5, 6]. However, larger-area patterning by shifting shadow masks, droplet size and profile control and lifetime for ink-jet-printed devices are still out-standing questions.

Amorphous silicon *vs.* polysilicon, small molecule OLEDs *vs.* polymer OLEDs, these are all open questions — the only certainty seems to be that OLEDs will be in the next generation displays!

References

[1] L. S. Hung and M. G. Mason, *Appl. Phys. Lett.* **78**, 3732 (2001).

[2] M. Mizukami, K. Inukai, H. Yamagata, T. Konuma, T. Nishi, J. Koyama, S. Yamazaki, and T. Tsutsui, *SID Dig.*, 912 (2000).

[3] K. Inukai, H. Kimura, M. Mizukami, J. Maruyama, S. Murakami, J. Koyama, T. Konuma and S. Yamazaki, SID Dig., 924 (2000).

[4] G. Rajeswaran, M. Itoh, M. Boroson, S. Barry, T. K. Hatwar, K. B. Kahen, K. Yoneda, R. Yokoyama, T. Yamada, N. Komiya, H, Kanno, and H. Takahashi, *Soc. Info. Disp. Symp. Dig.*, 974 (2000).

[5] T. R. Hebner, C. C. Wu, D. Marcy, M. H. Lu, and J. C. Sturm, *Appl. Phys. Lett.* **72**, 519 (1998).

[6] T. Shimoda, S. Kanbe, H. Kobayashi, S. Seki, H. Kiguchi, I. Yudasaka, M. Kimura., S. Miyashita, R. H. Friend, J. H. Burroughes, C. R. Towns, *SID Dig.*, 376 (1999).

Appendix A

Mathematica Scripts for Numerical Computations

A.1 Overview

The scripts were written for use with Mathematica (Wolfram Research). They are run with the format: "<<filename" in a Mathematica notebook, where <filename> is the name of the script. For example <<intensity.txt would execute the commands in the ascii file intensity.txt sequentially.

All length are in nm's. All rates are normalized to the intrinsic radiative decay rate. The following architecture is assumed: cathode/Alq_3/PVK/ITO/glass/air. The microcavity is between the cathode and the glass substrate. Transmission from glass to air is treated classically.

The variable "x" denotes the modal angel in Alq_3, in radians.

A.2 Procedure

The procedure for calculating the decay rates of a singlet exciton in the OLED cavity is as follows:

1. Determine the material constants, i.e., the refractive indices, and the thickness of all the layers.

2. Calculate the dipole life time in the cavity using the Green's function method. The name of the script to be run is "Comp3.txt" (approximate run time: several hours):

    - Before running, the definition of material constants in the file must be updated.
    - The complex permittivity of Ag is used for the cathode. The results are already weighted by the Alq_3 spectrum.
    - The output is $W_\perp$ and $W_\parallel$: the decay rate for perpendicular and parallel dipoles, respectively, in the format of 10 values computed at 10 evenly spaced locations in the Alq_3layer, i.e., given a structure Ag/80 nm Alq_3/40 nm PVK/100 nm ITO/glass, $W_\perp$ and $W_\parallel$ are calculated assuming the dipole is 80, 72, 64, ..., 16, 8 nm away from the cathode.
    - Save Wper and Wpar in a file called "dipole??.txt".
    - Calculated the external and substrate modes using "inten33.txt" (approximate run time: minutes):

- Update both the material constants, and the "dipole??.txt" file that contains the output from the previous step.
- The limits of integration in the integral are determined by the critical angles for TIR.
- The script runs and numbers like extTE, extTM, subTE, subTM are calculated. They are the external and substrate modes in TE and TM polarizations. The number returned is WextTE/Wtot, i.e., if extTE = 0.1 then given a singlet exciton in the cavity, 10
- If nglass < nAlq, there are ITO/org modes which are calculated with "inten34.txt": Update both the material constants, and the "dipole??.txt" file that contains the output from step 2. Run the script and, the energy in TE and TM modes are in apiTE and apiTM, respectively.

A.3 Mathematica scripts

A.3.1 Comp3.txt

```
(* comp3.txt, Green's function compute total rates.  Dec. 2000,
modified from comp2.txt, compute only 10 points every case *)

nAg={}; kAg={};

For[spec=380, spec<=780, spec+=4,

    If[spec<=382, nAg = Append[nAg, 0.23]; kAg = Append[kAg, 1.86],

    If[spec<=413, nAg = Append[nAg, 0.23]; kAg = Append[kAg, 1.86
        + 0.41 (spec-382)/31],
```

```
    If[spec<=496, nAg = Append[nAg, 0.23 + 0.01 (spec-413)/83];
        kAg = Append[kAg, 2.27 + 0.82 (spec-413)/83],

    If[spec<=620, nAg = Append[nAg, 0.24 + 0.03 (spec-496)/124];
        kAg = Append[kAg, 3.09 + 1.09 (spec-496)/124],

    If[spec<=827, nAg = Append[nAg, 0.27]; kAg = Append[kAg,
        4.18 + 1.61 (spec-620)/207]

    ]   ]   ]   ]   ]

];

ncat[lamb_] = nAg[[Round[(lamb-380)/4+1]]] + I
kAg[[Round[(lamb-380)/4+1]]];

na = 1.85; ng = 2.0; ni = 1.67; no = 1.71;

do = 80; di = 40; dg = 150;

zo = do; zi = do + di; zg = dg + di + do;

kc[lamb_] = 2 Pi ncat[lamb]/lamb; ko[lamb_] = 2 Pi no/lamb;
kg[lamb_] = 2 Pi ng/lamb; ki[lamb_] = 2 Pi ni/lamb; ka[lamb_] = 2
Pi na/lamb;

hc[x_,lambda_] = Sqrt[(2 Pi ncat[lambda]/lambda)^2 - x^2];
ho[x_,lambda_] = Sqrt[(2 Pi no/lambda)^2 - x^2]; hg[x_,lambda_] =
Sqrt[(2 Pi ng/lambda)^2 - x^2]; hi[x_,lambda_] = Sqrt[(2 Pi
ni/lambda)^2 - x^2]; ha[x_,lambda_] = Sqrt[(2 Pi na/lambda)^2 -
x^2];

<<cop.txt <<alq2.dat alq=alq/Sum[alq[[j]],{j,1,101}];
specpoints=101;

Wper = Table[Sum[(1 + 1.5 NIntegrate[Re[x^3/(ho[x,380+4(j-1)]
ko[380+4(j-1)]^3) Exp[I 2 ho[x,380+4(j-1)] l/10 do]
fop[x,380+4(j-1),l/10 do]], {x,0,0.999999
ko[380+4(j-1)]},PrecisionGoal->3] + 1.5
NIntegrate[x^3/(Im[ho[x,380+4(j-1)]] ko[380+4(j-1)]^3) Exp[- 2
Im[ho[x,380+4(j-1)] l/10 do]] Im[fop[x,380+4(j-1),l/10
```

```
do]],{x,1.0001 ko[380+4(j-1)],1.01 ko[380+4(j-1)],4.2/(1+Log[l/10
do])}, PrecisionGoal->3,MaxRecursion->15]) alq[[j]],
{j,specpoints}], {l,1,10}];

Wpar = Table[Sum[(1 + 0.75 NIntegrate[Re[x/(ho[x,380+4(j-1)]
ko[380+4(j-1)]) Exp[I 2 ho[x,380+4(j-1)] l/10 do]
(cop[x,380+4(j-1),l/10 do] - ho[x,380+4(j-1)]^2/ko[380+4(j-1)]^2
fop[x,380+4(j-1),l/10 do])], {x,0,0.999999
ko[380+4(j-1)]},PrecisionGoal->3] + 0.75
NIntegrate[x/(Im[ho[x,380+4(j-1)]] ko[380+4(j-1)]) Exp[- 2
Im[ho[x,380+4(j-1)] l/10 do]] Im[cop[x,380+4(j-1),l/10 do] -
ho[x,380+4(j-1)]^2/ko[380+4(j-1)]^2 fop[x,380+4(j-1),l/10 do]],
{x,1.0001 ko[380+4(j-1)],1.01 ko[380+4(j-1)],1.75},
PrecisionGoal->3,MaxRecursion->15]) alq[[j]], {j,specpoints}],
{l,1,10}];

diTE={}; diTM={};

For[n=1, n<=10, n++,
    diTE=Append[diTE,1/(Wpar[[n]] + 2.125)];
    diTM=Append[diTM,1/(Wper[[n]] + 2.125)]
];
```

A.3.2 inten33.txt

```
(* inten33.txt *) (* 4-layer model,  perfect cathode, includes
Alq, exciton decay *) (* include also exciton efficiency as a
function of dist. to cathode, from Bulovic papaer *) (* over a 1
degree cone.  Both integrated and narrow angle results.

modified from inten31.txt, fixed the way diTE and diTM called*)

(* Mike Lu, dec. 2000 *) (* To be read in a Mathematica notebook
with "<< inten31.txt" *)

(* length scale: 1 unit = 1 nm *)

na = 1.51; ng = 2; ni = 1.67; no = 1.71; nepo=1.81;

do = 80; di = 40; dg = 100;
```

```
<<dipole39.txt

Wnr = 2.125; delta = 20; norm = NSum[Exp[-(do
i/10/delta)],{i,0,9}];

koz[x_,lambda_] = 2 Pi/lambda no Cos[x]; kiz[x_,lambda_] = 2
Pi/lambda ni Sqrt[1 - no^2/ni^2 Sin[x]^2]; kgz[x_,lambda_] = 2
Pi/lambda ng Sqrt[1 - no^2/ng^2 Sin[x]^2];

thetmax = 75.7*Pi/180;

rl = 1.96; da = 0; beta[x_] = ArcSin[da/rl Sin[x]]; alpha[x_] =
ArcSin[na da/rl Sin[x]];

g2a[x_] = (1/na)^2 Cos[x]/Sqrt[1-(1/na Sin[x])^2];  (* x is angle
in air *)

(* x is angle in air *) g2aTE[x_] = (2 na Sqrt[1-(1/na Sin[x])^2]
/ (na Sqrt[1-(1/na Sin[x])^2] + Cos[x]))^2 (1/na)
Cos[x]/Sqrt[1-(1/na Sin[x])^2]; g2aTM[x_] = (2 na Sqrt[1-(1/na
Sin[x])^2] / (Sqrt[1-(1/na Sin[x])^2] + na Cos[x]))^2 (1/na)
Cos[x]/Sqrt[1-(1/na Sin[x])^2];

(* x is angle in glass *) g2aTE2[x_] = (2 na Cos[x] / (na Cos[x] +
Sqrt[1-(na Sin[x])^2]))^2 (1/na) Sqrt[1-(na Sin[x])^2]/Cos[x];
g2aTM2[x_] = (2 na Cos[x] / (Cos[x] + na Sqrt[1-(na Sin[x])^2]))^2
(1/na) Sqrt[1-(na Sin[x])^2]/Cos[x];

g2alens[x_] = (Cos[alpha[x]] + na da^2/rl^2 Sin[x]^2 + da/rl
Cos[x] Cos[alpha[x]] - na da/rl Cos[x] Cos[beta[x]]) / (1 + da/rl
Cos[x]/Cos[beta[x]] - ng da/rl Cos[x]/Cos[alpha[x]]);
g2alensTE[x_] = (2 na Cos[x] / (na Cos[x] + nepo Sqrt[1-(na/nepo
Sin[x])^2]))^2 (2 nepo Sqrt[1-(na/nepo Sin[x])^2] / (na Cos[x] +
nepo Sqrt[1-(na/nepo Sin[x])^2]))^2; g2alensTM[x_] = (2 na Cos[x]
/ (nepo Cos[x] + na Sqrt[1-(na/nepo Sin[x])^2]))^2 (2 nepo
Sqrt[1-(na/nepo Sin[x])^2] / (nepo Cos[x] + na Sqrt[1-(na/nepo
Sin[x])^2]))^2;

CTE[x_,lamb_]= koz[x,lamb]/kgz[x,lamb] Cos[koz[x,lamb] do]
Cos[kiz[x,lamb] di]          Cos[kgz[x,lamb] dg] -
kiz[x,lamb]/kgz[x,lamb] Sin[koz[x,lamb] do] Sin[kiz[x,lamb]   di]
Cos[kgz[x,lamb] dg] - koz[x,lamb]/kiz[x,lamb] Cos[koz[x,lamb] do]
```

```
Sin[kiz[x,lamb] di] Sin[kgz[x,lamb] dg] - Sin[koz[x,lamb] do]
Cos[kiz[x,lamb] di]   Sin[kgz[x,lamb] dg];

DTE[x_,lamb_]= koz[x,lamb]/kgz[x,lamb] Cos[koz[x,lamb] do]
Cos[kiz[x,lamb] di]          Sin[kgz[x,lamb] dg] -
kiz[x,lamb]/kgz[x,lamb] Sin[koz[x,lamb] do] Sin[kiz[x,lamb]   di]
Sin[kgz[x,lamb] dg] + koz[x,lamb]/kiz[x,lamb] Cos[koz[x,lamb] do]
Sin[kiz[x,lamb] di] Cos[kgz[x,lamb] dg] + Sin[koz[x,lamb] do]
Cos[kiz[x,lamb] di]   Cos[kgz[x,lamb] dg];

CTM[x_,lamb_]= -ng^2/no^2 koz[x,lamb]/kgz[x,lamb] Sin[koz[x,lamb]
do] Cos[kiz[x,lamb] di]   Cos[kgz[x,lamb] dg] - ng^2/ ni^2
kiz[x,lamb]/kgz[x,lamb] Cos[koz[x,lamb] do]        Sin[kiz[x,lamb]
di] Cos[kgz[x,lamb] dg] + ni^2/no^2 koz[x,lamb]/kiz[x,lamb]
Sin[koz[x,lamb] do] Sin[kiz[x,lamb] di] Sin[kgz[x,lamb] dg] -
Cos[koz[x,lamb] do]   Cos[kiz[x,lamb] di] Sin[kgz[x,lamb] dg];

DTM[x_,lamb_]= -ng^2/no^2 koz[x,lamb]/kgz[x,lamb] Sin[koz[x,lamb]
do] Cos[kiz[x,lamb] di]   Sin[kgz[x,lamb] dg] - ng^2/ ni^2
kiz[x,lamb]/kgz[x,lamb] Cos[koz[x,lamb] do]        Sin[kiz[x,lamb]
di] Sin[kgz[x,lamb] dg] - ni^2/no^2 koz[x,lamb]/kiz[x,lamb]
Sin[koz[x,lamb] do] Sin[kiz[x,lamb] di] Cos[kgz[x,lamb] dg] +
Cos[koz[x,lamb] do]   Cos[kiz[x,lamb] di] Cos[kgz[x,lamb] dg];

(* The following are the wavelength dependent emission normalized
to Wtot *)

I4TE[x_,lamb_,l_] = no^2/na^2 Sin[koz[x,lamb] l]^2 /(1/3
Wper[[Round[l 10/do]]] + 2/3 Wpar[[Round[l 10/do]]] +
Wnr)/(ng^2/na^2 (1 - no^2/ng^2 Sin[x]^2)/(1 - no^2/na^2 Sin[x]^2)
CTE[x,lamb]^2 + DTE[x,lamb]^2);

I4TM[x_,lamb_,l_] = (Cos[x]^2 Sin[koz[x,lamb] l]^2 + Sin[x]^2
Cos[koz[x,lamb] l]^2)/ (1/3 Wper[[Round[l 10/do]]] + 2/3
Wpar[[Round[l 10/do]]] + Wnr) / (na^2/ng^2 (1 - no^2/ng^2
Sin[x]^2)/(1 - no^2/na^2 Sin[x]^2) CTM[x,lamb]^2 + DTM[x,lamb]^2);


<<alq2.dat alq=alq/Sum[alq[[j]],{j,1,101}]; specpoints=101; (*
extTE = Sum[Sum[NIntegrate[I4TE[ArcSin[na/no Sin[x]], 380+4(j-1),
(10-i) do/10] Sin[x] , {x,0,ArcSin[1/na]},PrecisionGoal->3]
Exp[-(i do/10 /delta)], {i,0,9}]/norm alq[[j]], {j,specpoints}];
```

```
Print["extTE ",extTE]

extTM = Sum[Sum[NIntegrate[I4TM[ArcSin[na/no Sin[x]], 380+4(j-1),
(10-i) do/10] Sin[x] , {x,0,ArcSin[1/na]},PrecisionGoal->3]
Exp[-(i do/10 /delta)], {i,0,9}]/norm  alq[[j]], {j,specpoints}];
Print["extTM ",extTM]*)

subTE = Sum[Sum[NIntegrate[I4TE[ArcSin[na/no Sin[x]], 380+4(j-1),
(10-i) do/10] Sin[x],
{x,ArcSin[1/na],ArcSin[no/na]},PrecisionGoal->3] Exp[-(i do/10
/delta)], {i,0,9}]/norm alq[[j]], {j,specpoints}]; Print["subTE
",subTE]

subTM = Sum[Sum[NIntegrate[I4TM[ArcSin[na/no Sin[x]], 380+4(j-1),
(10-i) do/10] Sin[x],
{x,ArcSin[1/na],ArcSin[no/na]},PrecisionGoal->3] Exp[-(i do/10
/delta)], {i,0,9}]/norm alq[[j]], {j,specpoints}]; Print["subTM
",subTM] (* lensTE = Sum[Sum[NIntegrate[I4TE[ArcSin[na/no Sin[x]],
380+4(j-1), (10-i) do/10] Sin[x], {x,0,thetmax},PrecisionGoal->3]
Exp[-(i do/10 /delta)], {i,0,9}]/norm alq[[j]], {j,specpoints}];
Print["lensTE ",lensTE]

lensTM = Sum[Sum[NIntegrate[I4TM[ArcSin[na/no Sin[x]], 380+4(j-1),
(10-i) do/10] Sin[x], {x,0,thetmax},PrecisionGoal->3] Exp[-(i
do/10 /delta)], {i,0,9}]/norm alq[[j]], {j,specpoints}];
Print["lensTM ",lensTM]

lensTE100 = Sum[Sum[NIntegrate[I4TE[ArcSin[na/no Sin[x]],
380+4(j-1), (10-i) do/10] Sin[x], {x,0,50/180 Pi}] Exp[-(i do/10
/delta)], {i,0,9}]/norm alq[[j]], {j,specpoints}];
Print["lensTE100 ",lensTE100]

lensTM100 = Sum[Sum[NIntegrate[I4TM[ArcSin[na/no Sin[x]],
380+4(j-1), (10-i) do/10] Sin[x], {x,0,50/180 Pi}] Exp[-(i do/10
/delta)], {i,0,9}]/norm alq[[j]], {j,specpoints}];
Print["lensTM100 ",lensTM100]

lenssubTE = Sum[Sum[NIntegrate[I4TE[ArcSin[na/no Sin[x]],
380+4(j-1), (10-i) do/10] Sin[x], {x,thetmax,Pi/2}] Exp[-(i do/10
/delta)], {i,0,9}]/norm alq[[j]], {j,specpoints}];
Print["lenssubTE ",lenssubTE]
```

```
lenssubTM = Sum[Sum[NIntegrate[I4TM[ArcSin[na/no Sin[x]],
380+4(j-1), (10-i) do/10] Sin[x], {x,thetmax,Pi/2}] Exp[-(i do/10
/delta)], {i,0,9}]/norm alq[[j]], {j,specpoints}];
Print["lenssubTM ",lenssubTM] *)

(* compute far field intensity pattern at 6 degree intervals. *)
(* ffTE = Table[Sum[Sum[I4TE[ArcSin[1/no Sin[(n-1) 6 Pi/180]],
380+4(j-1), (10-i) do/10] Exp[-(i do/10 /delta)], {i,0,9}]/norm
g2a[6 (n-1) Pi/180] g2aTE[6 (n-1) Pi/180] alq[[j]],
{j,specpoints}], {n,16}];

ffTM = Table[Sum[Sum[I4TM[ArcSin[1/no Sin[(n-1) 6 Pi/180]],
380+4(j-1), (10-i) do/10] Exp[-(i do/10 /delta)], {i,0,9}]/norm
g2a[6 (n-1) Pi/180] g2aTM[6 (n-1) Pi/180] alq[[j]],
{j,specpoints}], {n,16}];

ideallensTE = Table[Sum[Sum[I4TE[ArcSin[na/no Sin[angle[[n]]]],
380+4(j-1), (10-i) do/10] Exp[-(i do/10 /delta)], {i,0,9}]/norm
alq[[j]] g2alens[angle[[n]]], {j,specpoints}], {n,1,16}];

ideallensTM = Table[Sum[Sum[I4TM[ArcSin[na/no Sin[angle[[n]]]],
380+4(j-1), (10-i) do/10] Exp[-(i do/10 /delta)], {i,0,9}]/norm
alq[[j]] g2alens[angle[[n]]], {j,specpoints}], {n,1,16}];

fflensTE = Table[Sum[Sum[I4TE[ArcSin[na/no Sin[angle[[n]]]],
380+4(j-1), (10-i) do/10] Exp[-(i do/10 /delta)], {i,0,9}]/norm
alq[[j]] g2alens[angle[[n]]] g2alensTE[angle[[n]]],
{j,specpoints}], {n,1,16}];

fflensTM = Table[Sum[Sum[I4TM[ArcSin[na/no Sin[angle[[n]]]],
380+4(j-1), (10-i) do/10] Exp[-(i do/10 /delta)], {i,0,9}]/norm
alq[[j]] g2alens[angle[[n]]] g2alensTM[angle[[n]]],
{j,specpoints}], {n,1,16}]; *) (*
Sum[ffTE[[i]]Sin[(i-1)Pi/30]Pi/30,{i,1,11}]
Sum[ffTM[[i]]Sin[(i-1)Pi/30]Pi/30,{i,1,11}]
Sum[ideallensTE[[i]]Sin[(i-1)Pi/30]Pi/30,{i,1,11}]
Sum[ideallensTM[[i]]Sin[(i-1)Pi/30]Pi/30,{i,1,11}] *)
```

A.3.3 inten34.txt

```
(* Michael Lu Dec. 1999, inten34.txt *) (* compute radiation in
ito/pvk/alq layer. First, find allowable k vectores. *) (* unit of
```

```
length scale nm *) (* variable x: angle in the alq layer modified
from inten32 by fixing Wtot*)

ng = 1.51; ni = 2.0; np = 1.67; na = 1.71;

da = 80; dp = 40; di = 150;

delta = 20; norm = Sum[Exp[-(da i/10/delta)],{i,0,9}];

critang1 = ArcSin[ng/na]; critang2 = ArcSin[np/na];

<<dipole36.txt; Wnr = 0;

<<alq2.dat; alq=alq/Sum[alq[[j]],{j,1,101}]; specpoints = 101;

(* Plot[Tan[kiz[x] di]/kiz[x] + (ATE[x] Sin[kpz[x] dp] + BTE[x]
Cos[kpz[x] dp]) / kpz[x]/ (ATE[x] Cos[kpz[x] dp] - BTE[x]
Sin[kpz[x] dp]), {x, critang1, Pi/2}]

Plot[Cot[kiz[x] di] ni^2/kiz[x] - (ATM[x] Sin[kpz[x] dp] + BTM[x]
Cos[kpz[x] dp]) np^2 / kpz[x] / (ATM[x] Cos[kpz[x] dp] - BTM[x]
Sin[kpz[x] dp]), {x,critang1,Pi/2}] *) (* OpenWrite["api5a.txt"];
WriteString["api5a.txt", "wavelength\t",
"TEX\t","F2TE\t","TMX\t","F2TM\n"]; *)

apiTE=0;apiTM=0;

TEX=1.2; TMX=1.3;

For[p=1, p < 102, p++,

    lamb = 380 + 4 (p-1);

    kaz[x_] = 2 Pi/lamb na Cos[x];
    kpz[x_] = 2 Pi/lamb np Sqrt[1 - na^2/np^2 Sin[x]^2];
    kiz[x_] = 2 Pi/lamb ni Sqrt[1 - na^2/ni^2 Sin[x]^2];

    ATE[x_] = kaz[x]/kpz[x] Cos[kaz[x] da];

    BTE[x_] = Sin[kaz[x] da];

    CTE[x_] = - (ATE[x] Sin[kpz[x] dp] + BTE[x] Cos[kpz[x] dp])
```

```
    /Sin[kiz[x] di];

ATM[x_] = - np^2/na^2 kaz[x]/kpz[x] Sin[kaz[x] da];

BTM[x_] = Cos[kaz[x] da];

CTM[x_] = (ATM[x] Sin[kpz[x] dp] + BTM[x] Cos[kpz[x] dp])
    /Cos[kiz[x] di];

f2TE[x_] = lamb/2 Sin[x] Sum[Sin[kaz[x] (10-i) da/10]^2 /
    (1/3 Wper[[10-i]] + 2/3 Wpar[[10-i]] + Wnr) Exp[-(i da/10
    /delta)], {i,0,9}]/norm /(na^2 (da - 0.5 Sin[2 kaz[x] da])
    + np^2 (dp - 0.5 Sin[2 kpz[x] dp]) ATE[x]^2 + np^2 (dp +
    0.5 Sin[2 kpz[x] dp]) BTE[x]^2 - 0.5 np^2 ATE[x] BTE[x]
    (Cos[2 kpz[x] dp] - 1) + ni^2 CTE[x]^2 (di - 0.5 Sin[2
    kiz[x] di]));

f2TM[x_] = lamb/2 /na^2 Sin[x] Sum[(Sin[x]^2 Cos[kaz[x] (10-i)
    da/10]^2 + Cos[x]^2 Sin[kaz[x] (10-i) da/10]^2) /(1/3
    Wper[[10-i]] + 2/3 Wpar[[10-i]] + Wnr) Exp[-(i da/10
    /delta)], {i,0,9}]/norm /(da + 0.5 Sin[2 kaz[x] da] +
    ATM[x]^2 (dp - 0.5 Sin[2 kpz[x] dp]) + BTM[x]^2 (dp + 0.5
    Sin[2 kpz[x] dp]) - 0.5 ATM[x] BTM[x] (Cos[2 kpz[x] dp]
    -1) + CTM[x]^2 (di + 0.5 Sin[2 kiz[x] di]));

TEX=x /. FindRoot[Tan[kiz[x] di]/kiz[x]+(ATE[x] Sin[kpz[x] dp]+
    BTE[x] Cos[kpz[x] dp])/kpz[x]/(ATE[x] Cos[kpz[x] dp]-BTE[x]
    Sin[kpz[x] dp])==0, {x,1.3}];

TMX=x /. FindRoot[Cot[kiz[x] di] ni^2/kiz[x]-(ATM[x] Sin[kpz[x]
    dp]+BTM[x] Cos[kpz[x] dp]) np^2/kpz[x]/(ATM[x] Cos[kpz[x]
    dp]-BTM[x] Sin[kpz[x] dp])==0,{x,1.3}];

If[TEX > critang1 && TEX < critang2, apiTE +=f2TE[TEX] alq[[p]]];
If[TMX > critang1 && TMX < critang2, apiTM +=f2TM[TMX] alq[[p]]];

(* WriteString["api5a.txt",ToString[lamb], "     ",ToString[TEX],
"   ", ToString[f2TE[TEX]], "   ",ToString[TMX], "   ",
ToString[f2TM[TMX]],"\n"]; *)

Print[lamb,", ",TEX,", ",f2TE[TEX],", ",TMX,", ",f2TM[TMX]];
]
```

```
(* Close["api5a.txt"]; *)
```

Appendix B

Publications and Presentations Resulting from This Work

Journal publications

1. M.-H. Lu and J. C. Sturm, "Light emission in organic light-emitting devices: modeling and experiment", *J. Appl. Phys.*, accepted.

2. M.-H. Lu and J. C. Sturm, "External coupling efficiency in planar organic light emitting devices", *Appl. Phys. Lett.* **78**, 1927 (2001).

3. C. F. Madigan, M.-H. Lu, and J. C. Sturm, "Improvement of output coupling efficiency of organic light emitting diodes by backside substrate modification", *Appl. Phys. Lett.* **76**, 1650 (2000).

4. T. R. Hebner, C. C. Wu, D. Marcy, M. H. Lu, and J. C. Sturm, "Ink-jet printing of doped polymers for organic light emitting devices", *Appl. Phys.*

Lett. **72**, 519 (1998).

5. C. C. Wu, S. D. Theiss, G. Gu, M. H. Lu, J. C. Sturm, S. Wagner and S. R. Forest, "Integration of organic LEDs and a-Si TFTs onto unbreakable and flexible metal foil substrate", *IEEE Elec. Dev. Lett.* **18**, 609 (1997).

Conference proceedings and presentations

1. (Invited) M.-H. Lu and J. C. Sturm, "External coupling and cathode effects in organic light-emitting devices: modeling and experiments", *SPIE Proceedings*, to be published.

2. K. Long, M.-H. Lu, F. Pschenitzka, and J. C. Sturm, "Novel three-color polymer light-emitting devices for passive-matrix flat panel displays", *59th Dev. Res. Conf. Dig.*, 179 (2001).

3. (Poster)F. Pschenitzka, M.-H. Lu, and J. C. Sturm, "Patterning of OLED cathodes by metal dry etching", *SID Dig.*, 731 (2001).

4. M.-H. Lu, C. F. Madigan, and J. C. Sturm,"Improved external coupling efficiency in organic light-emitting devices on high-index substrate", *IEDM Tech. Dig.*, 607 (2000).

5. M.-H. Lu, C. F. Madigan, and J. C. Sturm,"Experiment and modeling of conversion of substrate-Waveguided light to surface-emitted light", *Mat. Res.*

Soc. Symp. Proc. **621**, Q3.7 (2000).

6. R. M. A. Dawson, Z. Shen, D.A. Furst, S. Connor, J. Hsu, M.G. Kane. R. G. Stewart, A. Ipri, C. N. King, P. J. Geen, R. T. Flegal, S. Pearson, W. A. Barrow, E. Dickey, K. Ping, S. Robinson, C. W. Tang, S. Van Slyke, F. Chen, J. Shi, M. H. Lu, M. Moskewicz, and J. C. Sturm, "A polysilicon active matrix organic light emitting diode display with integrated drivers", *SID Dig.*, 438 (1999).

7. M. H. Lu, E. Ma, J. C. Sturm, and S. Wagner, "Amorphous silicon TFT active-matrix OLED pixel", *Lasers Electro-opt. Soc. Symp. Proc.*, 130 (1998).

8. R. M. A. Dawson, M. G. Kane, Z. Shen, D.A. Furst, S. Connor, J. Hsu, R. G. Stewart, A. Ipri, C. N. King, P. J. Geen, R. T. Flegal, S. Pearson, W. A. Barrow, E. Dickey, K. Ping, S. Robinson, C. W. Tang, S. Van Slyke, F. Chen, J. Shi, J. C. Sturm, and M. H. Lu, "Active Matrix Organic Light Emitting Diode Pixel Design using Polysilicon Thin Film Transistors", *Proc. LEOS'98*, 128 (1998).

9. (Invited) J. C. Sturm, F. Pschenitzka, T. R. Hebner, M. H. Lu, C. C. Wu, and W. Wilson, "Patterning approaches and system power efficiency considerations for organic LED displays", *SPIE Proc.* **3476** (1998).

10. R. M. A. Dawson, Z. Shen, D.A. Furst, S. Connor, J. Hsu, M.G. Kane. R.

G. Stewart, A. Ipri, C. N. King, P. J. Geen, R. T. Flegal, S. Pearson, W. A. Barrow, E. Dickey, K. Ping, S. Robinson, C. W. Tang, S. Van Slyke, F. Chen, J. Shi, M. H. Lu, and J. C. Sturm, "The impact of the transient response of organic light emitting diodes on the design of active matrix OLED displays", *IEDM Tech. Dig.*, 875 (1998).

11. R. M. A. Dawson, Z. Shen, D.A. Furst, S. Connor, J. Hsu, M.G. Kane. R. G. Stewart, A. Ipri, C. N. King, P. J. Geen, R. T. Flegal, S. Pearson, W. A. Barrow, E. Dickey, K. Ping, S. Robinson, C. W. Tang, S. Van Slyke, F. Chen, J. Shi, J. C. Sturm and M. H. Lu, "Design of an Improved Pixel for a Polysilicon Active-Matrix Organic LED Display", *SID Dig.*, 11 (1998).

12. K. A. Killeen, T. R. Hebner, F. Pschenitzka, M.-H. Lu, M. E. Thompson, and J. C. Sturm, "Single-layer polymer-blend organic light emitting diodes", *Abs. Pap. Am. Chem. Soc.* **216**, 583-POLY, Pt. 3 (1998).

13. E. Y. Ma, S. D. Theiss, M.H. Lu, J.C. Sturm and S. Wagner, "Thin film transistors for foldable displays", *IEDM Tech. Dig.*, 535 (1997).

14. (Poster) E.Y. Ma, S. D. Theiss, M. H. Lu, C. C. Wu, J. C. Sturm, and S. Wagner, "Organic Light Emitting Diode/Thin Film Transistor Integration for Foldable Displays", *17th Int. Disp. Res. Conf.* L78 (1997).

15. C. C. Wu, S. Theiss, M. H. Lu, J. C. Sturm, and S. Wagner, "Integration of organic LEDs and amorphous Si TFTs onto unbreakable metal foil sub-

strates", *IEDM Tech. Dig.*, 957 (1996).

Patent applications

1. PCT/00133598WO, Sturm, James, C.; Madigan, Conor, F.; and Lu, Min-Hao, M., "Organic light emitting diode having spherical shaped patterns".